
Few-cycle laser-driven electron accelerators

Daniel E. Cárdenas Armas



München 2018

Few-cycle laser-driven electron accelerators

Daniel E. Cárdenas Armas

Dissertation
an der Fakultät für Physik
der Ludwig-Maximilians-Universität
München

vorgelegt von
Daniel E. Cárdenas Armas
aus Caracas, Venezuela

München, den 9. Juni 2017

First Supervisor: Prof. Dr. Ferenc Krausz
Second Supervisor: Prof. Dr. Malte Kaluza
Examination date: July 27th 2017

Contents

Zusammenfassung	xiii
Abstract	xv
Introduction	xvii
Publications by the author	xxiii
1 The light source: Optical parametric synthesizer LWS-20	1
1.1 The Laser	1
1.1.1 The synthesis	1
1.1.2 Intensity contrast ratio	4
2 Laser-plasma I	7
2.1 Laser-driven ionization mechanisms	7
2.2 Single electron in a highly intense electromagnetic field	8
2.2.1 Ponderomotive force	12
2.3 Propagation of electromagnetic waves in plasmas	14
2.3.1 Underdense plasmas	15
2.3.2 Overdense plasmas	17
2.4 Particle-in-cell simulations (PIC)	20
3 Laser wakefield electron acceleration	23
3.1 Basics of LWFA	24
3.1.1 Wakefield generation and wavebreaking limit	24
3.1.2 Electron injection into the wakefield	25
3.1.3 Electron energy gain limitations	27
3.1.4 Externally injected electron beams: shock front	29
3.1.5 Beamloading	30
3.2 LWFA experimental setup	31
3.2.1 The LWFA chamber	32
3.2.2 Shock-front generation	34
3.3 LWFA experimental results	36
3.3.1 The dephasing effect	37

4	Relativistic attosecond nanoplasmonics	59
4.1	Nano-solids basics	60
4.1.1	Laser-plasma II: Light absorption and scattering in nano-solids . . .	60
4.1.2	Sub-cycle (non-ponderomotive) acceleration in plasmonic fields . . .	69
4.1.3	CEP effects in nanoplasmonics	70
4.2	RANP experiment setup	74
4.3	RANP experimental results	75
4.3.1	Electron emission from a nano-target	75
4.3.2	Intensity-dependent angular distribution	81
4.3.3	CEP effects observed	84
4.3.4	Discussion	88
5	Conclusions and outlook	99
5.1	The LWFA electron phase-space evolution	99
5.2	CEP-dependent emission of relativistic electrons from nanotargets	100
5.3	Looking towards the future	102
6	Data archiving	113
	Acknowledgments	119

List of Figures

1.1	Laser scenario in 2017	2
1.2	Layout of LWS-20	3
1.3	Two-color-pumped OPCPA sequential amplification	4
1.4	LWS-20 spectrum and temporal structure	5
1.5	Measured LWS-20 intensity contrast	6
2.1	Laser intensity vs. Tungsten ionization levels	9
2.2	Electron kinetic energy in the laser field in the laboratory frame	11
2.3	Sketch of ponderomotive force	12
2.4	Scattering angle vs electron initial velocity for $a_0 = 4.5$	13
2.5	Scattering angle vs a_0 for $\beta_0 = 0$	13
2.6	Group velocity dispersion in plasmas	15
2.7	Plasma-scale length in solids	19
2.8	Skin depth in solids	19
2.9	Relativistic pseudo-transparency	19
2.10	PIC simulations on RANP experiments	21
2.11	PIC simulations on LWFA at $a_0 = 7$	21
2.12	Electron spectrum from PIC simulations on LWFA at $a_0 = 7$	21
3.1	Boat-driven wake.	23
3.2	One-dimensional wakefield in the quasi-static approximation at $8 \times 10^{19} \text{ cm}^{-3}$ and $\tau_L = 5 \text{ fs}$	26
3.3	LWFA phase-space diagram driven at $8 \times 10^{19} \text{ cm}^{-3}$ and $\tau_L = 5 \text{ fs}$	27
3.4	Sketch of shock-front injection	31
3.5	Experimental setup for the LWFA experiments	32
3.6	Laser focal spot used for LWFA experiments	33
3.7	Dipole magnet dispersion used in the sub-5 fs LWS-20 experiments.	34
3.8	Visualization of the shock front on the sideview camera.	35
3.9	Measured density profile of a 300 μm nozzle using shock front	36
3.10	Illustration of the experimental setup used for the LWFA experiments	37
3.11	Typical spatial properties of the electron beam produced in the LWFA experiments	38
3.12	Analogy of the wakefield in the laboratory frame	39

3.13	Peak energy of the electron spectrum for sub-10-fs laser pulses vs. acceleration lengths for various electron densities	40
3.14	Measured and predicted dephasing lengths	42
3.15	Transmitted laser spectrum after the LWFA	43
3.16	Rayleigh length determination for the LWFA experiments	43
3.17	Measured longitudinal accelerating field for different densities	44
3.18	Insight into the dephasing process	46
3.19	Scheme of the phase-space evolution of the shock-front injected beam . . .	48
3.20	Details of shock-front injection through PIC simulations	50
3.21	Comparison between experiments and PIC simulations for the 8 fs LWS-20 results	51
3.22	Simulated electron spectra with an 8 fs laser pulse with $a_0 = 0.75$ at a density of $4 \times 10^{19} \text{ cm}^{-3}$	52
3.23	Simulated longitudinal field for 5 fs+20 fs ²	53
3.24	Simulated laser and wakefield evolution with 5 fs	54
3.25	Simulated laser and wakefield evolution with 5 fs+20 fs ²	55
3.26	Simulated snapshots of the wakefield	56
4.1	Schematic of charge separation in a nanoparticle with radius R_0	64
4.2	Radial electric field for particles of radius 50,200 and 500 nm	66
4.3	Simulated radial electric field of nanospheres as function of time	68
4.4	Electron current generated through tunnel ionization	70
4.5	Electron trajectories in localized fields in the sub-cycle regime.	71
4.6	CEP effects in few-cycle lasers	72
4.7	Asymmetry parameter A for the case of Fig.(4.6)	73
4.8	Laser focal spot used for RANP experiment and determination of the Rayleigh length	74
4.9	Gouy phase shift in RANP experiment	75
4.10	Experimental setup for RANP experiment	76
4.11	Alignment procedure of each target during the RANP campaign	77
4.12	Average electron angular distribution in RANP experiment	78
4.13	Typical electron angular distribution along the nanoneedle axis	78
4.14	Electron spectrum measured in the RANP experiment	79
4.15	Polarization sensitivity in the RANP	80
4.16	Forces acting on the electron during its ejection from the nanotarget into vacuum.	81
4.17	Measured emission angle as a function of the laser peak intensity	82
4.18	Measured emitted charge as a function of the laser peak intensity	82
4.19	Typical shots for different laser peak intensities	83
4.20	Measured and simulated asymmetry parameter A_N as a function of the CEP.	85
4.21	Electron angular distribution as a function of the CEP.	86
4.22	Measured electron emission angle as a function of the CEP.	87
4.23	Simulated electron emission angle as a function of the CEP.	87

4.24	First step of the electron acceleration mechanism	89
4.25	Nanotarget surface field dynamics	90
4.26	Electron energy evolution in real space during the first step	90
4.27	Electron energy evolution through both acceleration steps	92
4.28	Second step of the electron acceleration mechanism	92
4.29	End of the electron acceleration in the second step	93
4.30	Simulated electron energy as a function of a_0 in RANP	94
4.31	CEP sensitivity of the electron emission during the first step	95
4.32	Simulated 2D asymmetry for one CEP	96
4.33	Simulated 2D asymmetry as a function of the CEP	97
5.1	Conclusion 1: Study of the electron dephasing in LWFA	100
5.2	Conclusion 2: CEP-dependent emission of relativistic electrons from nano- targets	101

List of Tables

1	Costs of particle accelerators and other costly world-wide projects	xviii
2.1	Laser intensity vs. ionization levels	8

Zusammenfassung

Die kollektive Bewegung von Elektronen im Plasma, ein Plasmon, besitzt ein damit verbundenes elektrostatisches Feld, welches den derzeit letzten Stand der Radiofrequenz-Beschleuniger-Technologie (50 MV/m) um mehrere Größenordnungen ($> 10^3 - 10^4$) übertrifft und räumlich auf den Bereich einer Plasmawellenlänge (1-0.1)'s μm beschränkt ist. Diese Plasmonen können mittels ultrakurzer und hochintensiver Laserpulse durch verschiedene Kopplungsmechanismen erzeugt werden. In dieser Doktorarbeit werden zwei verschiedene Typen von Plasma-basierten Elektronenbeschleunigern vorgestellt, die von Laserpulsen mit wenigen Lichtzyklen getrieben werden: (i) die sogenannte Laser WakeField Acceleration (LWFA) durch Erzeugung von Volumenplasmonen in Plasma geringer Dichte (unterdicht); (ii) und die Generierung der sogenannten lokalisierten Oberflächenplasmonen (localized surface plasmons, LSP) an der Schnittstelle zwischen nanometrischem Plasma hoher Dichte (im s.g. überdichten Bereich) und Vakuum. Während beide Prozesse durch Lichtpulse getrieben werden und der Gesamtenergiegewinn bis in den MeV Bereich reicht, ist die zugrunde liegende Physik grundverschieden. Im Falle der LWFA werden die Elektronen gefangen und in einer Plasmawelle beschleunigt (≈ 100 GV/m), die dem hochintensiven Laserpuls ($2-6 \times 10^{18}$ Wcm $^{-2}$) folgt, während dieser durch ein ionisiertes Heliumgas propagiert. Hingegen verstärken LSPs das einfallende Laserfeld (\geq TV/m) und fungieren als ein effizienter Photoinjektor von sub-fs relativistischen Elektronenbunch in das Laserfeld für eine anschließende Beschleunigung mittels Vacuum Laser Acceleration (VLA).

Die erste Hälfte der Doktorarbeit behandelt die erste systematische Messung der Evolution des Elektronenstrahls im Phasenraum, die durch die Dephasierungslänge charakterisiert ist. Die Studie wurde mit verschiedenen Elektronendichten $7 - 21 \times 10^{19}$ cm $^{-3}$ für den $\tau_{\text{puls}} < 5$ fs Lichtquelle, sowie für geringere Dichten (4×10^{19} cm $^{-3}$) mit dem älteren $\tau_{\text{puls}} = 8$ fs Laserpulsen durchgeführt. Für diesen Zweck wurde ein robuster externer Elektroneninjektionsmechanismus namens Shock Front verwendet, um die Beschleunigungslänge durch die Überprüfung der Injektionsposition in das Wakefield zu scannen. Aufgrund der starken Skalierung des Effekts, τ_{puls}^3 , wurden die gemessenen Dephasierungslängen auf 60-300 μm begrenzt und finale Energiespitzen von 6-20 MeV beobachtet. Shock-front-Injektion lieferte stabile und quasi-monoenergetische $\Delta E \approx 3 - 5$ MeV Elektronenstrahlen und ermöglichte die Veränderung der Parameter des Strahls, wie Ladung, Energiespitze, Divergent und relative Energiespreizung, erstmals mit hoher Auslösung zu überwachen. Darüber hinaus wurden neue Phänomene wie die Entschleunigung und konsekutive Dephasierung identifiziert.

Die zweite Hälfte der Arbeit beschäftigt sich mit der bahnbrechenden Emission von relativistischen Elektronenbunches von Nanonadeln. Ultraschnelle Nanophotonik wird um sechs Größenordnungen der Intensität in das relativistische Regime katapultiert. Wolfram-Nadeln von wenigen 100 Nanometern räumlicher Ausdehnung werden mit sub-two-cycle duration Lichtpulsen bei ultrarelativistischer Intensität (6×10^{19} Wcm $^{-2}$) bestrahlt. Solch eine hohe Spitzen-Laserintensität treibt die Elektronenenergie in den MeV Bereich und die Gesamtladung auf bis zu einige hundert Picocoulomb. In diesem Regime wird der Ausbreitungswinkel der Elektronenbunchen hauptsächlich durch die eintreffenden Laserintensität bestimmt, anstatt durch die Größe des Targets, wie klassisch erwartet und bisher bei niedriger Laserintensität berichtet. Darüber hinaus war die Winkelverteilung der emittierten Elektronen stark abhängig von der genauen Form des elektrischen Feldes, charakterisiert durch die Träger-Einhüllenden-Phase (carrier-envelope phase, CEP). In der Tat oszillierten so-wohl 15% der gemessenen Ladung als auch der Propagationswinkel der Elektronenbunches periodisch mit der CEP des treibenden Pulses. Durch Analyse der Ausbreitung der MeV Elektronenstrahlen wurden zwei aufeinander folgende Schritte identifiziert bezüglich des Ausstoßes von dem Target durch das erhöhte plasmonische Feld und der folgenden Beschleunigung durch das Laserfeld im Vakuum. Das beschleunigende elektrische Feld übertrifft in beiden Schritten die TV/m Grenze, und ist damit deutlich höher als die Felder, die mit anderen bekannten Techniken erzeugt wurden. Dieser Meilenstein der Laser-Plasma-Physik bildet die Basis eines lang erwarteten, direkt durch Laser im Vakuum erzeugten Elektronenbeschleunigungsmechanismus. Des Weiteren ebnet die starke Abhängigkeit der Winkelverteilung des Elektronenstrahls von der CEP den Weg zu einer neuen Generation von isolierten relativistischen attosekunden Elektronenbunches.

Abstract

The collective motion of electrons in plasma, *plasmons*, has an associated electrostatic field which surpasses the current state-of-the-art radio-frequency accelerator technology (50 MV/m) by several orders of magnitude ($> 10^3 - 10^4$); and a spatial dimension, the plasma wavelength, of (1 – 0.1)’s μm . These plasmons can be excited by the force of an ultrashort high-intensity laser pulse by different coupling mechanisms. In this thesis, two different types of few-cycle laser-driven plasma-based electron accelerators are exposed: (i) the so-called Laser WakeField Acceleration (LWFA) by the excitation of volume plasmons in a low density (underdense) plasma; (ii) and the generation of so-called localized surface plasmons (LSPs) at the interface of a high density (overdense) plasma of nanometer size and vacuum. While both processes are driven by light pulses and the total energy gain scales up to the MeV range, the underlying physics are completely different. In LWFA, a few-fs electron bunch is trapped and accelerated in a plasma wave (≈ 100 GV/m) following the highly intense laser pulse, $2 - 6 \times 10^{18} \text{ Wcm}^{-2}$, as the latter propagates through an ionized Helium gas. On the other hand, LSPs enhance instantaneously the incident laser field (\geq TV/m) and act as an efficient photo-injector of sub-fs relativistic bunches into the laser field for subsequent acceleration in the Vacuum Laser Acceleration (VLA) scheme.

In the first half of this thesis, the first systematic measurement of the evolution of the electron beam in the phase-space, characterized by the dephasing length, is presented. The study was done for different electron densities $7 - 21 \times 10^{19} \text{ cm}^{-3}$ for the $\tau_{\text{pulse}} < 5$ fs light source as well as at lower densities, ($4 \times 10^{19} \text{ cm}^{-3}$) with the older $\tau_{\text{pulse}} = 8$ fs laser pulses. For this purpose, a robust external electron injection mechanism, named shock front, was utilized to scan the acceleration length by controlling the injection position into the wakefield. Due to the strong scaling, τ_{pulse}^3 , the measured dephasing lengths were limited to 60-300 μm and final peak energies of 6-20 MeV were observed. Shock-front injection provided stable and quasi-monoenergetic $\Delta E \approx 3 - 5$ MeV electron beams and allowed the evolution of the beam parameters such as charge, peak energy, divergence and relative energy spread to be monitored for the first time with high resolution. Moreover, new phenomena such as deceleration and consecutive dephasing were identified. The second half of the thesis deals with the “groundbreaking” emission of relativistic electron bunches from nanotargets. Ultrafast nanophotonics is boosted by 6 orders of magnitude in intensity for the first time into the relativistic realm. Tungsten needle targets of 100’s nm spatial extent were irradiated with sub-two-cycle duration light pulses at ultra relativistic intensity, $6 \times 10^{19} \text{ Wcm}^{-2}$. Such a high peak laser intensity automatically thrust the electron energy in the MeV range and the total charge to the 0.1’s nC scale. In this regime, the propagation angle of the electron bunches was determined mainly by the incident laser intensity, rather than the size of the target as classically expected and reported until now at much lower laser intensity. Moreover, the electron angular distribution of the emitted electrons was a sensitive function of the exact shape of the electric field, characterized by the carrier-envelope-phase (CEP). Indeed, about 15% of the measured electron yield oscillated periodically as a function of the CEP as well as the propagation angle of the electron bunches, which oscillated in a correlated manner. By analyzing the evolution of the MeV electron beams, two consecutive steps were identified regarding the ejection from the target by the enhanced plasmonic field and subsequent acceleration by the laser field in vacuum. The accelerating electric field in both steps exceeded the TV/m limit, significantly beyond any other technique to date. This milestone of laser-plasma physics forms the basis of a long-desired electron acceleration mechanism directly by lasers in vacuum. Furthermore, the strong sensitivity of the electron beam angular distribution properties to the CEP paves the way to the next generation of relativistic electron sources, providing isolated and attosecond electron pulses.

Introduction

The understanding of phenomena involving the transport of charge has over 2600 years of history. Since the observation of first electrostatic forces on amber (in Greek, $\eta\lambda\epsilon\kappa\tau\rho\theta\nu$, "electron") in 600 B.C. by Thales of Milet, the interaction of electromagnetic fields with charged particles has caught attention of scientists across centuries. From sheer curiosity, it has become one of the pillars of modern civilization.

Particle accelerators today: a 10^9 \$ infrastructure on km^2 size

Among many other technologies, the idea to accelerate electrons to generate secondary sources of radiation or discover new fundamental particles has been exaggeratedly appealing. It has applications over various branches sweeping from science, industry and medicine [143, 31, 98]. Moreover, in 1979 the idea of a Laser electron Plasma-based Accelerator[144] (LPA) was conceived. This partially overlapped in time with the evolution of ultra-high power femtosecond laser technology. Chirped-Pulsed Amplification (CPA)[139] revolutionized the laser technology and allowed the generation of 10's fs pulses with high peak power which soon reached the required intensities in the original LPA proposal, about $I_L \approx 10^{18} \text{ Wcm}^{-2}$. The laser intensity is determined by:

$$I_L = \frac{\epsilon_0 c E_L^2}{2} \quad (1)$$

where, ϵ_0 and c are the vacuum permeability and the velocity of light in vacuum, respectively. The alternative idea of a highly intense laser used for accelerating particles seems natural since intensities of 10^{18} Wcm^{-2} correspond to an electric field of $E_L \approx 3 \text{ TVm}^{-1}$. As it will be described in this work, acceleration of particles with the laser field itself is far from trivial. In order to circumvent this limitation, the original LPA idea takes advantage of the collective properties of gaseous plasmas and their capacities to sustain fields of the order $E_{plasma} \approx 100 \text{ GVm}^{-1}$. The most basic concept of an LPA was called LWFA. In this case, the laser pulse triggers huge charge separation regions, the acoustic electron plasma wave, where a strong longitudinal electrostatic field is generated. The LWFA boom came in 2004 when different groups [53, 44, 99] reported 50-100 MeV quasi-monoenergetic electrons. Nowadays, LWFA is routinely realized in many laboratories around the world and due to its competitive features, it is currently attracting scientists to work on and the states to invest in this promising technology.

Particle accelerator	Cost (USD)	Size (km)
CERN* (EUROPE)	7.5 G\$	10's
SLAC* (USA)	350 M\$	3
Sirius* (Brazil)	400 M\$	0.5
Sesame* (Middle East)	79 M\$	0.1
Extreme Light Infrastructure ⁺ (ELI)	750 M\$	≈ 0.01 (table-top)
Conventional Petawatt (PW) system ⁺	10 M\$	≈ 0.01 (table-top)

Other costly projects	Cost (USD)
U.S. defense budget	800 G\$
Project Apollo Space Program	25G\$
Eradicate world poverty	175 G\$

Country/Region	GDP (USD)
European Union GDP	16 T\$
U.S. GDP	18 T\$
Brazil GDP	2 T\$
Middle East GDP	1.5 T\$
Afghanistan GDP	20 G\$

Table 1: Cost of different projects regarding particle accelerators around the world, along with the Gross-Domestic-Product (GDP) of different regions. For the sake of completeness and comparison, other important costly projects are also included. Particle accelerators labeled with * represent conventional particle accelerators, while + are future laser-based ones.

In order to get a good impression on how much effort is being put into particle accelerators, laser-driven and conventional ones, take a look at Table 1. From this table, here are some key points:

1. How much particle energy is enough? MeV, GeV or even TeV energy level. Different applications require particular spectral ranges. From 100's MeV level protons[113] and heavy ions [83] for cancer therapy. Moreover, TeV electron-positron or TeV protons collisions allow new fundamental particles to be discovered, such as the Higgs Boson[1]. Current state-of-the-art accelerators are limited to maximum values about 50 MVm^{-1} before electrical breakdown. This automatically corresponds to acceleration lengths of $\text{TeV}/\text{MVm}^{-1} \rightarrow 10^2$ km. For this purpose, circular structures such as the Large Hadron Collider (LHC)[42] in CERN with a circumference of about 30 km are designed where the hadrons accelerates subsequently until it reaches the desired range.
2. The size of LPAs are mostly limited to the laser system size, the so-called table-top, since the acceleration itself takes place within an adult human's hand. State-of-the-art reports have demonstrated GeV electrons within few centimeters [89]. A key advantage of LPAs is their compactness given by the large accelerating fields ($\approx 100 \text{ GV m}^{-1}$), about 10^4 higher than conventional radio-frequency based technology, such as CERN or SLAC.
3. The amount of money invested in building such accelerators is intuitively proportional to their size. Although cutting-edge-laser technology projects are quite expensive at the moment, such as ELI, the budget is far below the one used for big facilities such as CERN. Moreover, conventional PW systems are becoming routinely available, even more in the near future, thus lowering their selling price.
4. Particle accelerators have applicability in science, industry and medicine. In particular for the latter, radiation-based cancer therapy is already being implemented in several hospitals around the globe [117]. Furthermore, electron acceleration leads to secondary sources, such as broad band ultra-brilliant X-rays. A charged particle propagating in a circular geometry, such as a synchrotron loses $\frac{E_{kin}^4}{m^4 R}$ per turn, where E_{kin} and m are particle kinetic energy and rest mass, and R the radius of the accelerator. In the case of LHC at CERN, this "lost" energy is on the order of a few keV per proton and about 1% of the energy gain per round-trip due to its large circumference of 27 km. Yet, in the case of electrons $m_e \ll m_p$, this photon emission is utilized for multiple X-ray scientific[82] and medical studies[141].
5. The particle accelerator community is huge and its economical weight surpasses many third-world economies. The budget to build one accelerator such as CERN is even comparable to the GDP of an entire country. This data is meant to transmit the reader the importance of this field and its huge technological future. Its worth is recognized by governments from different countries which are currently investing an incredible amount of money, about 0.1% of their GDP, in building them.

The LPA community has made significant progress in the last decade. Record values are few GeV and few percent energy spread (rms). Electron charge lies within few pC at GeV and

100's pC at 100's MeV energies, few millimeters to centimeters acceleration length and few femtosecond bunch duration. The generation of such ultrashort electron pulses is intrinsic to the LWFA mechanism, since the bunches occupy a fraction of the plasma wavelength which spans from few to many 10's μm . Nevertheless, the overall performance must fulfill extreme requirements demanded by big-impact applications such as an X-ray synchrotron or a free-electron laser (XFEL). Reducing the costs and size is not enough. LPA's electron parameters such as absolute energy spread, charge, stability, among others, must be significantly improved. In particular, seeding an XFEL[50] require monochromaticity $\ll 1\%$ energy spread, high charge ≈ 1 nC within 0.1% of the spectral bandwidth at 1 GeV[98], 10's fs pulse duration, small normalized emittance ($< 1\text{nm}$)[100], reproducibility, etcetera. The injection into the accelerating structure has become a fundamental step for meeting these demanding criteria. Among different external injection mechanisms[25, 47], shock-front injection[131] has gained relevance within the laser-accelerator community due to the stability, tunability and absolute energy spread, reaching few per cent [14].

In the family of laser accelerators, LWFA would be the experienced big brother. Still the fact that $E_L \approx 3\text{TVm}^{-1}$ at 10^{18}Wcm^{-2} (orders of magnitude higher than in LWFA), makes the idea of accelerating the electrons directly with lasers very appealing. Vacuum Laser Acceleration (VLA) has been largely studied since its original proposal in 1995 [40]. Surfing this field seemed rather complicated, for a relativistic ($>\text{MeV}$) electron bunch should be injected within a half laser cycle. Thus, LWFA is to femtosecond as VLA is to attosecond. Via exotic interactions with solids, VLA made it to the spotlight in 2015 [147] by generating a 20-MeV attosecond electron bunch train. Nevertheless, no mention of the expected fields of $O(\text{TVm}^{-1})$ was made nor insight into the injection mechanism was described. Solid further steps in this promising direction are taken in the second half of this work.

High field lasers today: still a $10^7\text{\$}$ infrastructure on 10 m^2 size

LPA technology could be competitive, among many things, for its compactness and lower costs. Nevertheless, only highly intense and expensive $\gg 10^6\text{\$}$ TW-PW laser systems with 10's m^2 size can drive the acceleration. Can we actually further reduce the required laser systems? Once again, the answer lays in collective motion of electrons.

The resonant oscillation of a slab of electrons under the influence of an optical electromagnetic wave leads to a localized sub-wavelength confinement of light at the surface of a nano-scale target. In this way, the incident light wave is locally enhanced. So far, the reported enhancement factors have been relatively weak, scarcely exceeding unity [142], by employing isolated nanotargets of about 100's nm size. Higher values of about multi-10 can be reached by shooting at even smaller samples and factors of even $\approx 10^2\text{'s}$ are reachable by shooting at a system of isolated nanoparticles [137, 68], as in bow-tie configuration. Further experiments regarding the excitation of propagating plasmons along metal-dielectric interfaces have shown enhancement factors of 10's. The latter are essentially light waves that are trapped on the surface because of their resonant interaction with the free electrons of the conductor. [6]. The capacity to "multiply" the laser intensity of smaller and more economic lasers is indeed very attractive as well as to

realize electron "nano accelerators". State-of-the-art novel nJ-laser-driven mini-accelerators have reached accelerating fields up to a few-GVm⁻¹ [65] and kinetic energies in the keV level [71, 37]. In this work, we examine to which extent can few-TW pulses be enhanced by a target of 100's nm size at unprecedented intensities and its final impact on the electron emission. This topic will be referred to as Relativistic Attosecond Nanoplasmonics (RANP).

The high degree of sensitivity of matter to the incident electric field gave birth to the attosecond science [84] and this strong dependence is one of the hallmarks of this research field. Tailored few-cycle light pulses might also revolutionize laser-plasma physics by controlling exactly the electronic motion in matter. However, such a field dependence has been until now scarcely unknown in the relativistic realm. The laser technology was just not available. For this reason, our high-intensity light source is a pioneering and unique system.

Structure of this work

Chapter 1: The light source

The first chapter describes the light source utilized in this thesis, the Light Wave Synthesizer 20 (LWS-20). The laser parameters are not only described in terms of energy and pulse duration, but the reader understands the uniqueness of LWS-20 and is able to identify its pioneering position in the context of relativistic laser plasma physics in the near single-cycle regime.

Chapter 2: Basics of laser-plasma interactions

The second chapter is a review of the most relevant laser-plasma interactions. Here, general concepts involving the two experiments explained in this work are introduced. These include ionization mechanisms and single electron motion in the laser field, as well as the optical properties regarding propagation of light in overdense and underdense plasmas. Finally, some basic notions of Particle-In-Cell simulations are presented, along with examples involving the experimental work exposed in this thesis. This chapter provides the knowledge to interpret and understand the experimental results discussed in chapter 3 and 4.

Chapter 3: LWFA experiment

Firstly, this chapter provides a short introduction of the laser wakefield accelerator concept, including the wakefield generation and some electron injection mechanisms as well as the main limitations of the maximum obtainable electron energy and their corresponding scaling in terms of the laser parameters, in particular the electron dephasing. The rest of the chapter corresponds to the first experiment this thesis deals with: a detailed analysis of the phase-space evolution of the electron beam during its acceleration in the laser wakefield. This evolution is characterized by the dephasing length, about 60-300 μm for the current sub-5 fs LWS-20 version and the old 8 fs one.

Chapter 4: RANP experiment

Firstly, this chapter provides a short and more detailed introduction about laser-plasma interactions in solids, including absorption mechanisms as a function of the laser intensity and the plasma scale length. Moreover, the scattering of light by targets whose dimensions are smaller than the optical wavelength, ≈ 100 's nm at low intensities is also presented. Furthermore, a historical background about the electron emission from these nanotargets as a function of the exact shape of the laser electric field using near-IR laser pulses is shown as well as the study of the sub-cycle emission regime at mid-IR driving conditions. This knowledge, combined with Chapter 2, should suffice to understand the experimental observations. The rest of the chapter corresponds to the second experimental campaign of this thesis: the attosecond emission of relativistic electrons from nanotargets in the near single-cycle regime.

Chapter 5: Conclusions and outlook

This chapter provides a summary and conclusions of both experiments and gives an outlook of laser plasma accelerators in the regimes investigated in this work as well as some near future applications.

Publications by the author

The experiments reported in this thesis were performed using the LWS-20 laser system at the Max Planck Institute for Quantum Optics. In these experiments, the author played an active role in terms of laser performance, work in laboratory and interpretation of the collected data. Moreover, the author also collaborated in other scientific works presented below.

- D.E. Cardenas, S. Chou, J. Xu, L. Hofmann, A. Buck, K. Schmid, C.M.S. Sears, D.E. Rivas, B. Shen, and L. Veisz. *Energy limitation of laser-plasma electron accelerators*. Submitted to **New Journal of Physics**. (2017)

- The author contributed to build the experimental setup and was largely responsible for the electron diagnostics. The experimental data was collected by the author in collaboration with S.C. and L.H. The author evaluated the data obtained with the sub-5 fs LWS-20 laser, re-evaluated the data obtained with the 8 fs LWS-20 and wrote the manuscript with the input from L.V. and S.C. plus other co-authors.

- D.E. Cardenas, T.M. Ostermayr, L. Di Lucchio, L. Hofmann, P. Gibbon, J. Schreiber and L. Veisz. *Sub-cycle relativistic nanophotonics*. Submitted to **Nature Photonics**. (2017)

- The author designed and built the experimental setup with collaboration from L.H. The data was collected by the author with T.M.O., who participated in the experimental campaign. The author performed the complete analysis of the experimental data, evaluated the results obtained from simulations and wrote the manuscript with suggestions from L.V. and other co-authors.

- D.E Rivas, A. Borot, D.E. Cardenas, G. Marcus, X. Gu, D. Herrmann, J. Xu, J. Tan, D. Kormin, G. Ma, W. Dallari, G. Tsakiris, I. Földes, S. Chou, M. Weidmann, B. Bergues, T. Wittmann, H. Schröder, P. Tzallas, D. Charalambidis, O. Raszkazovskaya, V. Pervak, F. Krausz, and L. Veisz. *Next Generation Driver for Attosecond and Laser-plasma Physics*. Accepted in **Scientific Reports** (2017).

- The author was largely responsible, together with D.E.R., in maintaining the good performance of the LWS-20 for his own experiments and others throughout his whole PhD. Moreover, the author designed and automatized the alignment for most of the amplification stages in a reproducible and user-friendly way.

- S. Chou, J. Xu, K. Khrennikov, D.E Cardenas, J. Wenz, M. Heigoldt, L. Veisz, and S. Karsch. *Collective deceleration of laser-driven electron bunches*. **Physical Review Letters**. **117**, 144801 (2016).

- The author performed simulations regarding the evolution of the electron beam using General Particle Tracer.

- M. Aladia, R. Bollaa, D.E. Cardenas, L. Veisz, and I. B. Földes. *Cluster size distributions in gas jets for different nozzle geometries*. Submitted to **Journal of Instrumentation** (2017)

- Scientific collaboration to characterize the gas jets used for electron acceleration.

Chapter 1

The light source: Optical parametric synthesizer LWS-20

Laser-matter interactions are divided in two major fields with two completely different perspectives: attosecond science and laser-plasma physics. Nowadays, high-peak power lasers provide relativistic intensities beyond 10^{18} Wcm^{-2} and can be utilized to accelerate particles such as electrons[98, 41]. Highly intense lasers started to develop interesting new physics when the generation of intense attosecond light pulses from solid targets was suggested [103, 106]. On the other hand, low-energy near single-cycle pulses have proved to control the electron currents in dielectrics[129] by the force of light in the attosecond range [59, 10]. Provided the high sensitivity of the electronic response to the exact shape of the incident field, sub-2 cycle lasers can trigger a final asymmetrical emission[110, 165] which exploits the applicability of these sources. Furthermore, highly interesting and exotic scenarios are expected when these short pulses are applied at relativistic intensities. Next generation of sub-fs particle sources such as isolated high-yield MeV electron[36, 91] or 100 eV photon[151, 94] bunches could be generated if such an asymmetry is exploited. State-of-the-art multi-10 mJ few-cycle broadband light sources [16, 78, 156], such as ours, based in chirped nonlinear amplification are filling this gap in the laser world scenario. In particular, our laser, the sub-5 fs Light-Wave Synthesizer (LWS-20) is an unique system which connects the attosecond science and the high-energy field as shown in Fig.(1.1). When focused to almost the diffraction limit $w_0 \approx \lambda_L = 740 \text{ nm}$ with an unprecedented temporal intensity contrast, extreme interactions occur where the electrons reach $99\%c$ in less than 2 optical cycles.

1.1 The Laser

1.1.1 The synthesis

In the laser community, the idea of a synthesizer is to tailor exactly the pulse waveform with a certain amplitude and phase. The “tailoring” gains importance when the laser pulse is not longer described exclusively by its envelope, but by the electric field, which consists of few cycles and their relative amplitude vary significantly under the envelope. Furthermore, following the classical relationship $\Delta\omega\tau_{\text{pulse}} = C$ (where C is a constant), only broadband light pulses support these

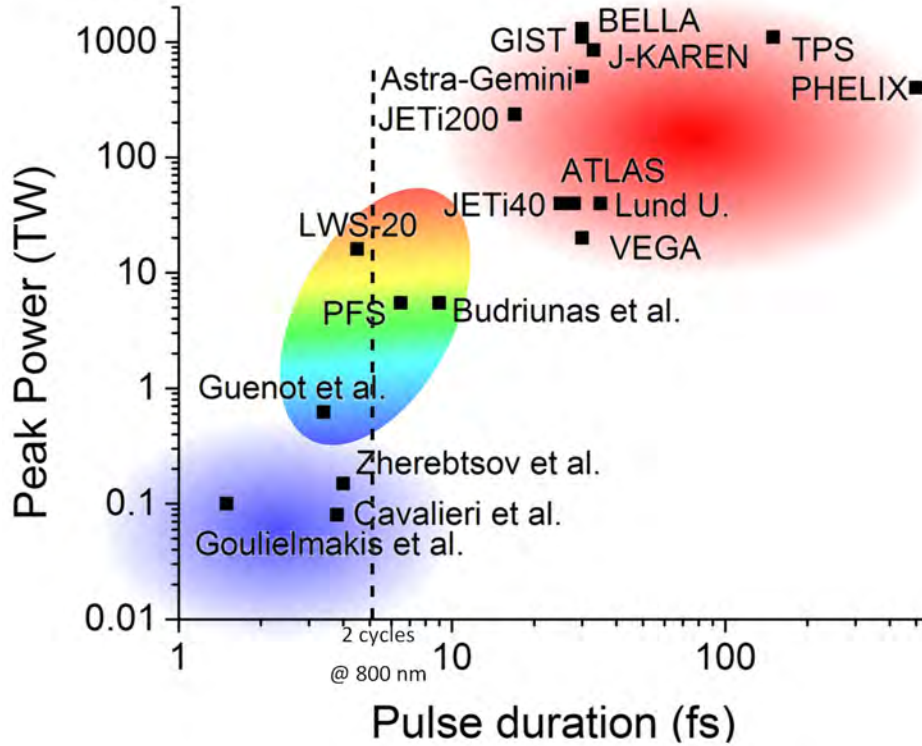


Figure 1.1: Laser scenario in 2017. Typical laser systems corresponding to relativistic plasma physics are highlighted in red: ATLAS [14], Lund Laser Center (LLC) [35], 20 TW VEGA system [126], JETi200 [75], Astra-Gemini [70], the Petawatt system at the Gwangju Institute of Science and Technology [80], the BELLA project [88], the J-KAREN system [3], the Texas Petawatt System (TPS) [52] and the PHELIX laser [4]. Find a complete review on Petawatt lasers in [32]. Some examples of few-cycle sub-mJ laser systems working in the attosecond field are marked in blue: Cavalieri et al.[20], Zherebtsov et al.[164] and down to single-cycle regime from Goulielmakis et al.[59]. Single-cycle pulses with higher energies (mJ-level) are becoming available as well, as reported by Guénot et al.[60]. Finally, few-cycle multi-10 mJ lasers such as: the Petawatt-Field Synthesizer (PFS) [78] and the work of Budriunas et al. [16], together with the sub-2 cycle LWS-20 [156] used in this thesis, fill the gap between these research areas. As observed in the figure above, the LWS-20 is the few-cycle most powerful laser in the world.

short pulse durations τ_{pulse} . Here is where the synthesis takes place[59] and gives name to our laser system. Different spectral components are coherently mixed, yet each one is independently controlled in terms of amplitude and phase. Furthermore, our amplification scheme is scalable to higher energies.

The LWS-20 is based in Optical Parametric Chirped-Pulse Amplification (OPCPA). This technology is a mixture between the traditional CPA technology and parametric light amplification in a nonlinear medium [39], resulting in a broadband energy gain of up to several orders of

magnitude[22, 155].

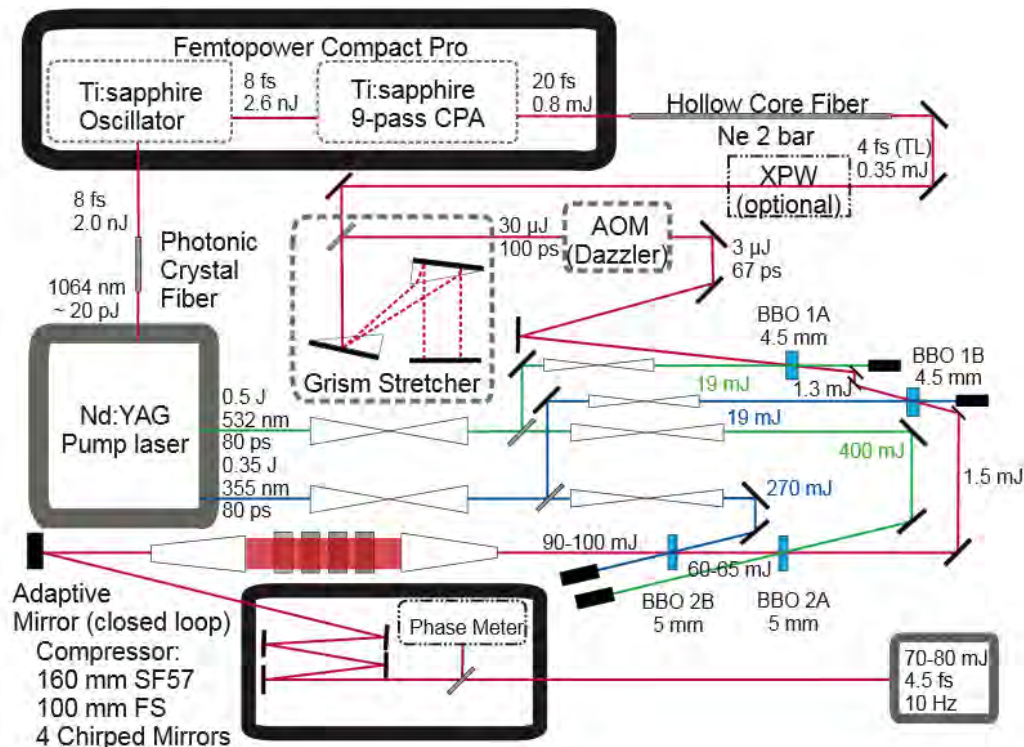


Figure 1.2: Layout of LWS-20

The LWS-20 layout is shown in Fig.(1.2). The system is born in a 80 MHz few-nJ few-cycle Ti:Sa oscillator which seeds simultaneously the front end (60%) as well as the pump laser (40%). The first part of the front end is a commercially available CPA-based Ti:Sa system delivering light pulses centered at 800 nm with 1 mJ and 22 fs pulse duration at 1 kHz repetition rate (Femtopower Compact Pro, Femtolasers GmbH). These pulses are sent into a Neon-filled hollow-core-fiber for spectral broadening via self-phase-modulation [23]. Immediate compression down to sub-5 fs using chirped mirrors is required when the Cross-Wave Polarizer (XPW) is used[76]. Using XPW or not, the pulses are then temporarily stretched in a GRISM (a combination of a prism and grating) "stretcher" [146] up to 100 ps and directed straightaway to a acoustic-optical programmable dispersive modulator (DAZZLER, Fastlite Ltd.). The final seed (few- μ J) pulse duration is about 60 ps before the amplification.

The optically-synchronized 80 MHz pump seed is focused into a photonic crystal fiber (PCF) from which the spectral components around the desired wavelength, 1064 nm, are generated to be further amplified to Joule-level and stretched to 80 ps in a Nd:YAG flashlamp-based pump laser (ESKPLA). LWS-20 is based on two color pumping OPCPA [64] and therefore, second (540 mJ at 532 nm) and third harmonic (400 mJ at 355 nm) are generated and distributed in four amplification stages, two per colour, as described in Fig.(1.2). The broadband seed overlaps with the shorter wavelength pump in a type I BBO crystal (Beta Barium Borate) and it is amplified in a non-collinear fashion where phase-matching is fulfilled for a broader spectral

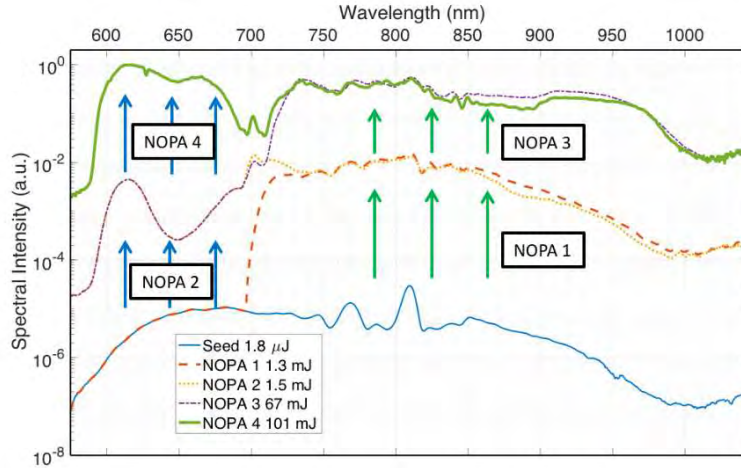


Figure 1.3: Two-color-pumped sequential amplification, spanning a spectrum from 580 to 1020 nm with an energy of about 100 mJ. Figure obtained from [156].

region. Visible spectral region (580-700 nm) and near-IR (700-1020 nm) are amplified separately and consecutively by the 355 nm and the 532 nm pump, respectively. After the last stage, a final energy of about 100 mJ is reached, as shown in Fig.(1.3). In order to avoid strong nonlinearities in the silica crystals, the still chirped pulses are expanded to a size of approximately 5 cm's and then compressed in 160 mm-long SF57 and 100 mm fused silica down to 100 fs. A deformable mirror and a wavefront sensor in a closed loop configuration were installed before the compressor chamber to optimize the small wavefront aberrations ≈ 50 nm in order avoid major energy losses on the focal plane. Four chirped mirrors are in charge of the final compression in vacuum down to sub-5 fs, see Fig.(1.4), and the pulse is finally sent to the experiments with an energy 70 mJ. For complete temporal characterization, the carrier envelope phase (CEP), φ_{CEP} , which is the offset between the optical phase and the maximum of the wave envelope of an optical pulse, must be measured. For this purpose, a small portion of the laser beam is taken from the main driver through a 5 mm diameter silver mirror coated on a 2 μm thick pellicle (National Photocolor) and sent to single-shot stereo phasemeter[161]. In this way, although the waveform shape is not controllable, it is measurable shot-to-shot.

1.1.2 Intensity contrast ratio

There are four origins of prepulses, post-pulses and pedestals in a CPA system. 1) incomplete compression of the laser pulse; 2) leakage from pulse pickers during the amplification; 3) amplified spontaneous emission (ASE) and 4) undesired reflections from optical components. The equivalent of ASE for optical OPCPA is the amplified optical parametric fluorescence (AOPF). As it will be explained later in sub-sec.2.3.2 and in chapter 4, the high-dynamic laser intensity temporal contrast is of extreme relevance in the laser-solid community. The intensity contrast of a pulse is defined as the peak intensity ratio at a determined time instant. So, an ASE pedestal is expected to come to the amplification stages since the LWS-20's front end is actually a conventional Ti:Sa

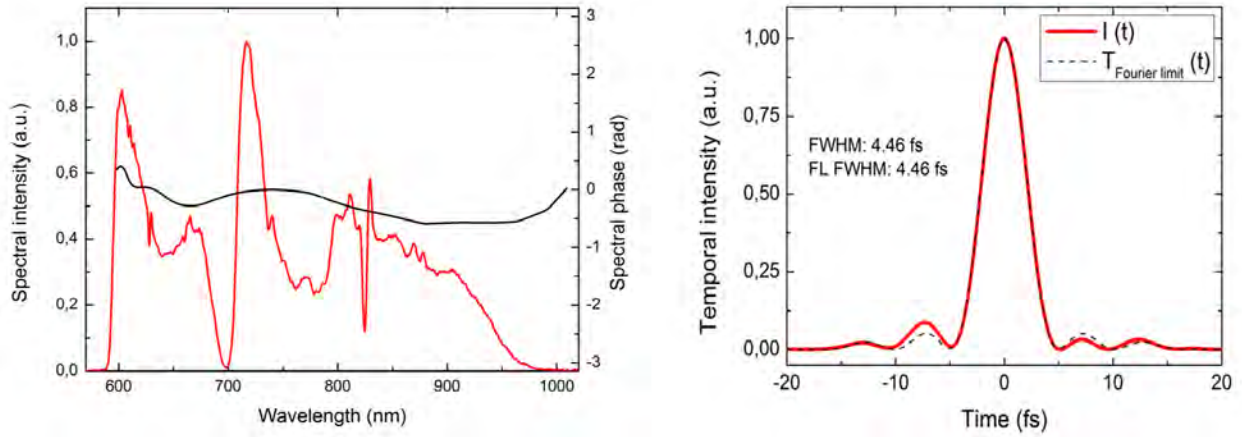


Figure 1.4: **Left:** The sub-5 fs LWS-20 spectral power density and phase. **Right:** Temporal structure of the Fourier-limited and compressed LWS-20 pulse.

system. However, picosecond-gated pumping to a final maximum gain of 10^5 compensates this limitation. The small gain in OPCPA is a nonlinear function of the laser intensity, $G \propto e^{\sqrt{I_{pump}}}$. Thus, strongly-pumped high-gain OPCPA, $G \approx 10^5$ in only one channel would lead to strong AOPF[81], since $I_{AOPF} \propto G$. For this purpose, LWS-20 possesses two sequential channels with gains of 10^3 in and 10^2 , respectively, for each color pump as seen in Fig.(1.3). In this way, control over the gain and I_{AOPF} is of extreme relevance when designing each OPA stage.

Laser-induced ionization mechanisms and plasma formation set on at very low intensities, at 10^{12} Wcm^{-2} as reviewed in sec.2.1. Hence, good contrasts of $10^7 - 10^8$ at few picoseconds, are needed for solid-target experiments. Picosecond pumping automatically temporarily compresses the energy density down to the ps range[78, 101]. Furthermore, two extra technologies can be implemented to improve the contrast, XPW and the so-called plasma mirror[38] (PM). For the experiments described in this work, only XPW was implemented. Although a good contrast is always desired as a starting point, each application or experiment is optimized for a certain plasma-scale length[163], i.e. intensity contrast. The measurement shown in Fig.(1.1.2) is based on a third-order nonlinearity and about $\Delta\lambda \approx 100 \text{ nm}$ from the whole spectrum is measurable.

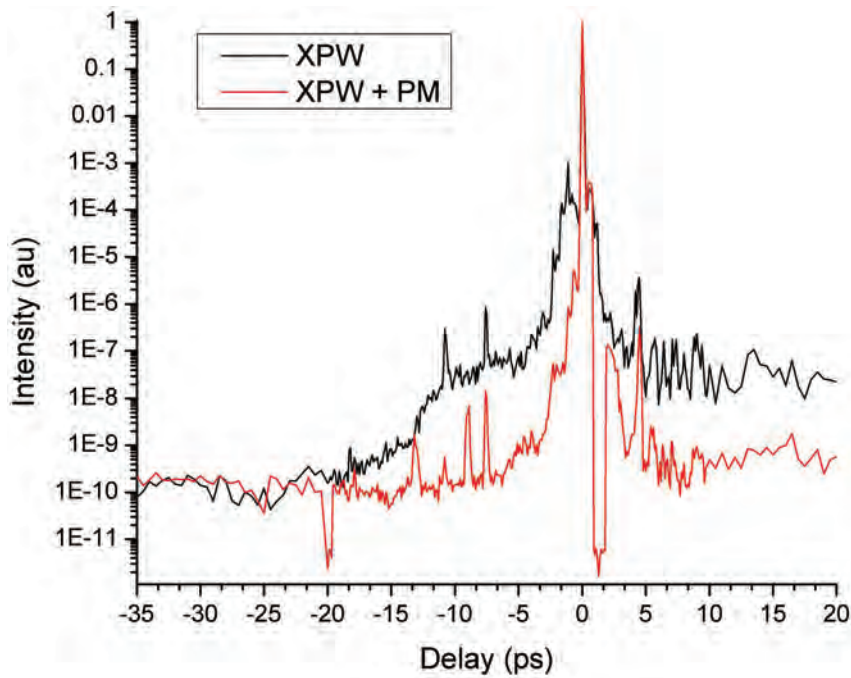


Figure 1.5: LWS-20's high-dynamic temporal intensity contrast by implementing XPW or XPW and subsequent PM. Figure obtained from [125].

Chapter 2

Laser-plasma I

The light source used in this work was already introduced in the previous chapter. Now, in this chapter we explain briefly the interaction of light with matter, and by matter we mostly mean plasma, a mixture of free electrons and immobile background ions. For this purpose, we first start by how matter is ionized under such strong fields (sec.2.1). Subsequently, we describe how a single electron is influenced by an electromagnetic wave (2.2) and immediately see that by focusing highly powerful multi-TW lasers to almost the diffraction limit λ_L , instantaneous energies of multi-MeV are reachable within a half laser cycle. We analyze the scenarios of laser acceleration in vacuum (VLA) in sub-sec.?? as well as ponderomotive acceleration in sub-sec.2.2.1. In sec.2.3, we will review various effects about the propagation of laser fields in underdense plasmas (sec.2.3.1) from analyzing the index of refraction. We will point important concepts and phenomena regarding "propagation" in overdense plasmas, such as solid-targets (sec. 2.3.2), serving as a prequel to sec.4.1.1 in the fourth chapter. Lastly, we will comment on a well-known computational tool scientists use to understand better the complicated physics beneath all these interactions in sec.2.4.

2.1 Laser-driven ionization mechanisms

Before deepening into the propagation of light in plasmas, such plasmas must be generated. A plasma is a medium where electrons and ions are moving freely. Particularly, in this work the plasma response is limited to the electron dynamics and the ions ($M_{ion} \gg m_e$) are assumed to remain as a constant background. Laser-driven typical ionization mechanisms are determined by the Keldysh parameter $\gamma_K = \sqrt{E_{ion}/2U_p}$, where E_{ion} is the ionization potential of a bound electron and U_p is the laser ponderomotive potential, i.e. the energy acquired by an electron within the laser field as discussed later in 2.2. At low laser intensities, $I_L \approx 10^{12} \text{ W cm}^{-2}$, $\gamma_K \gg 1$, an electron can absorb N photons $Nh\nu \geq eE_{ion}$ and surpass the binding potential. This is multi-photon ionization (MI). At modest intensities, $I_L \approx 10^{15} \text{ W cm}^{-2}$, $\gamma_K \ll 1$, the mechanism is dominated by tunnel ionization (TU). In this regime, the laser field bends the binding potential and allows a bound electron to quantumly tunnel the barrier. In particular, at extremely high intensities $I_L > 10^{16} - 10^{17} \text{ W cm}^{-2}$, the laser field is so strong that the electron can be freed

Ion (Z^*)	E_{ion} (eV)	Intensity (W cm^{-2})
$\text{He} \rightarrow \text{He}^+$	24.6	1.4×10^{15}
$\text{He}^+ \rightarrow \text{He}^{+2}$	54.4	8.8×10^{15}
$\text{W}^{+59} \rightarrow \text{W}^{+60}$	2575	4.9×10^{19}
$\text{W}^{+73} \rightarrow \text{W}^{+74}$	69525	1.7×10^{25}

Table 2.1: Required intensity given by Eq.(2.1) to ionize different ions.

spontaneously. This type of ionization is referred to as barrier suppression (BSI). The threshold laser intensity $I_{L,\text{BSI}}$ for BSI to occur is [54]:

$$I_{L,\text{BSI}} [\text{W cm}^{-2}] \approx 4 \times 10^9 \frac{(E_{\text{ion}}[\text{eV}])^4}{Z^{*2}} \quad (2.1)$$

where Z^* is the charge of the ionized atom. For instance, the required intensities to ionize some ions are shown in Table.(2.1). Typical intensities used in LWFA experiments, included the ones in this work, are on the order of $10^{18} \text{ W cm}^{-2}$. Moreover, most of the times the gas emanating from the nozzle is Helium. Full ionization thus occurs long before the main peak arrives at the interaction (see sec.1.1.2) and the assumption that laser light propagates in plasma is valid. Solid targets made of, for example Tungsten, are not completely ionized in the parameter range of current 80mJ LWS-20. Complete ionization of Tungsten $\text{W}^{73+} \rightarrow \text{W}^{+74}$ would require $1.7 \times 10^{25} \text{ W cm}^{-2}$, or about 3 J of energy within 2 optical cycles focused to the diffraction limit, not reachable by any laser technology available nowadays. At $I_L = 6 \times 10^{19} \text{ W cm}^{-2}$, the electron density in a Tungsten solid target would theoretically be, according to Eq.(2.1):

$$n_e = Z^* n_i = \frac{Z^* N_A \rho}{A}, \quad (2.2)$$

which after putting numbers for our case: $Z^* = 60$, $N_A = 6.02 \times 10^{23}$, $\rho = 19.3 \text{ g cm}^{-3}$ and $A = 183.85$, results in $n_e = 3.8 \times 10^{24} \text{ cm}^{-3}$. Thus, a fully ionized 400 nm diameter Tungsten hemisphere containing $2 \times 10^9 \text{ W}^{+74}$ ions would yield 25 nC.

2.2 Single electron in a highly intense electromagnetic field

The propagation of any electromagnetic wave $E(t)$, $B(t)$ through any medium is ruled by the Maxwell equations [73]:

$$\vec{\nabla} \cdot \vec{E} = \frac{\rho}{\epsilon_0}, \quad (2.3)$$

$$\vec{\nabla} \times \vec{E} = -\frac{\partial}{\partial t} \vec{B}, \quad (2.4)$$

$$\vec{\nabla} \cdot \vec{B} = 0, \quad (2.5)$$

$$\vec{\nabla} \times \vec{B} = \frac{1}{c^2} \frac{\partial}{\partial t} \vec{E} + \mu_0 \vec{j}. \quad (2.6)$$

$$(2.7)$$

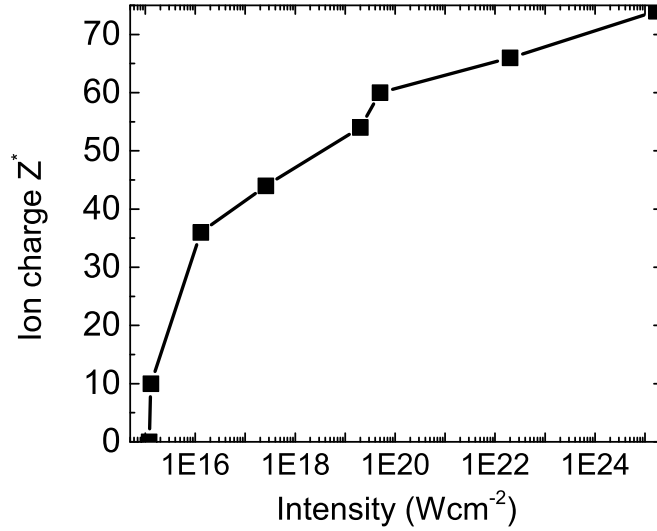


Figure 2.1: Tungsten ion charge W^{+Z^*} as a function of the laser intensity according to Eq.(2.1).

where ϵ_0 and μ_0 are the vacuum permittivity and the permeability, respectively; $c = 1/\sqrt{\epsilon_0\mu_0}$ the speed of light in vacuum, ρ is the charge density and \vec{j} is the current density. The electric \vec{E} and magnetic field \vec{B} , propagating with a wave vector $\vec{k}_L = \frac{\omega_L}{c} \vec{e}$, where $\omega_L = \frac{2\pi c}{\lambda_L}$ is the angular frequency, can be rewritten as a function of the vector potential $\vec{A} = \vec{A}_0 \cos(\omega_L t - \vec{k}_L \cdot \vec{x})$ and the scalar potential ϕ_L :

$$\vec{E}_L(\vec{x}, t) = -\frac{\partial}{\partial t} \vec{A} - \vec{\nabla} \phi_L,$$

$$\vec{B}_L(\vec{x}, t) = \vec{\nabla} \times \vec{A}.$$

In laser-plasma physics, there are two main laser concepts which determine the regime of the interaction: intensity I_L and ponderomotive energy $\propto I_L \lambda_L^2$. The intensity is the spatio-temporal energy density. For a laser pulse of duration τ_L , $I = \Phi/\tau_L$, where Φ is the photon flux. For this work, typical intensities of $10^{18} - 10^{20} \text{ Wcm}^{-2}$ were employed, leading to $\Phi \approx 5 \times 10^3 - 5 \times 10^5 \text{ Jcm}^{-2}$, or $10^{14} - 10^{16} \text{ photons } \mu\text{m}^{-2}$. The motion of a charged particle with a nonzero rest mass (an electron of e and m_e , respectively) in vacuum under the action of the laser field is given by the Lorentz and energy equations:

$$\frac{d\gamma\vec{v}}{dt} = -\frac{e}{m_e}(\vec{E} + \vec{v} \times \vec{B}), \quad (\text{Lorentz eq.}), \quad (2.8)$$

$$\frac{d\gamma}{dt} = -\frac{e}{m_e c^2}(\vec{v} \cdot \vec{E}), \quad (\text{Energy eq.}), \quad (2.9)$$

where $\vec{p} = \gamma m_e \vec{v}$ is the electron's momentum and $\gamma = \sqrt{1 + |\vec{p}|^2/(m_e c)^2}$ is the gamma factor of the electron. While the first term on the right side of the Lorentz equation above represents the linear response of the electron due to \vec{E} , the second term on the right side leads to a nonlinear response $\vec{v} \times \vec{B}$, which is responsible for the ponderomotive force. From Eq.(2.9), it can be

deduced that the quiver velocity of an electron within an electromagnetic half-cycle is given by: $v_{\text{quiver}} = \frac{eE_0}{\omega_L m_e} = \frac{eA_0}{m_e}$. For a linearly polarized field, the electron momentum in the transverse plane \vec{p}_\perp equals the vector potential, \vec{A} . $a_0 \equiv A_0/m_e c$ is commonly used to determine how relativistic the electron becomes:

$$a_0 = 0.854 \sqrt{I_L [10^{18} \text{ Wcm}^{-2}] \lambda_L [\mu\text{m}]}.$$
 (2.10)

The mean kinetic energy of an electron in the reference frame at which the quivering motion of the electron is at rest may be considered as an internal energy W [104]. W is defined as:

$$W = m_e c^2 \left[(1 + \langle a_0^2 \rangle)^{1/2} - 1 \right]$$
 (2.11)

where " $\langle \rangle$ " represents cycle-averaging. This corresponds to $\langle \gamma_{L,\text{quiver}} \rangle = \sqrt{1 + a_0^2/2} \rightarrow \beta_{\text{quiver}} = v_{\text{quiver}}/c = 0.7$, at $a_0 = 1$ or $2.5 \times 10^{18} \text{ Wcm}^{-2}$ using a 740 nm laser. The wiggling is further quantified by the quivering amplitude $l_q = eE_0/m_e \omega_L^2$. The classical ponderomotive potential $U_p = (eE_0)^2/4m\omega_L^2$ [112] corresponds to the energy of a quivering electron at its oscillation frame at very low intensities, $a_0 \ll 1$. At higher intensities, $a_0 \gg 1$, many laser-matter interactions are described as a function of a_0 . For instance, the electric field of the laser $E_0 = a_0/\lambda_L [\mu\text{m}] \times 3.21 \text{ TVm}^{-1}$. In the laboratory frame, it can be further deduced that the normalized momentum of an electron, originally at rest, under the influence of a linearly polarized electromagnetic wave will be determined by following expressions:

$$\tilde{p}_y = a_0 \cos \phi$$
 (2.12)

$$\tilde{p}_x = \tilde{p}_y^2/2,$$
 (2.13)

$$= \frac{a_0^2}{4} [1 + \cos 2\phi],$$
 (2.14)

$$\tilde{p}_z = 0.$$
 (2.15)

where \tilde{p} is the normalized electron momentum to $m_e c$ and $\phi = \omega_L t - \vec{k}_L \cdot \vec{x}$. Furthermore, the corresponding gamma factor and the final kinetic energy E_{kin} of the electron is just given by:

$$\gamma_{L,\text{lab}} = 1 + \tilde{p}_x,$$
 (2.16)

$$E_{\text{kin}} = (\gamma_{L,\text{lab}} - 1)m_e c^2$$
 (2.17)

$$= \frac{a_0^2}{4} [1 + \cos 2\phi] m_e c^2.$$
 (2.18)

The maximum energy gain under this scheme is then $\Delta E = m_e c^2 a_0^2/2$. From the formulas above 2.18, we could obtain maximum energies $E_{\text{kin}} \approx 100$'s keV and 10 MeV for $a_0 = 1$ and 8, respectively. Is it really so easy to gain energy in a travelling wave? No! In fact, many controversy has come to this topic due to Lawson-Woodward theorem[87, 162] (LWT). It states that an electron traveling in a straight trajectory along the laser axis from $z = -\infty$ to $z = +\infty$ with $v_z \approx c$ gains no net energy throughout its path in the laser field. The theorem permits acceleration if one of the following conditions is broken[54]:

1. The laser field is in vacuum, with no interfering walls or boundaries,

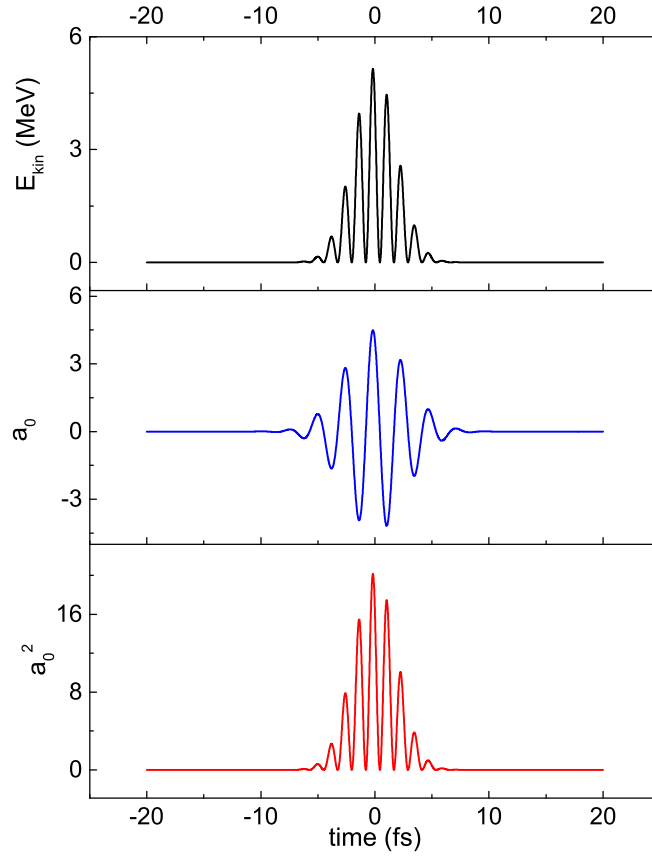


Figure 2.2: Top: Electron kinetic energy E_{kin} acquired instantaneously from the laser in the laboratory frame, using Eq.(2.18). Middle: Normalized vector potential a_0 . Bottom: Normalized instantaneous intensity a_0^2 .

2. The electron is highly relativistic along the acceleration path,
3. no static or magnetic fields are present,
4. the interaction region is infinite,
5. ponderomotive forces are neglected.

The main reason why an electron gains zero net energy after the laser field has passed through is the phase slippage between them. Nevertheless, the idea of an electron gaining high energy in the laser field has been very appealing and has caught the attention of many scientists and it is referred to as Vacuum Laser Acceleration (VLA)[40]. In spite of the fact that in a realistic scenario, i.e. a intense laser pulse focused tightly onto a solid target, most of the previous conditions from LWT are broken, it is still not enough for high energy gain and so far experimental results have only reported poor “vacuum acceleration” of about 10’s keV gain[115]. The key to finally discriminate

between the classical quivering regime and the real VLA[147] is the sub-cycle, i.e. attosecond, injection of relativistic electron beams. In this regime, the electron bunch propagates trapped within two half-cycles of the laser field[149] while gaining energy. Although different theories have tried to address the VLA mechanism using different laser polarizations[40, 159, 158, 111, ?], the final picture results in an energy gain in the ponderomotive potential well of the laser, even where “ponderomotive acceleration” is commonly referred to as a cycle-averaged process.

2.2.1 Ponderomotive force

The ponderomotive force originates from the finite spatio-temporal extension of the laser profile. Since $\vec{a} \equiv \vec{a}(r)$, Taylor-expansion of the laser field in the transversal direction yields an extra nonlinear component in the force of the light on the electron: $F_p = -m_e c^2 / \gamma_L \nabla(a^2/2)$. A similar expression is also deducible from Eq.(2.9). The ponderomotive force can be also understood as the light pressure I_L/c on a certain particle or target. This force pushes away the electrons from the most intense regions as shown in Fig.(2.3). The angle θ at which the electron scatters can intuitively be inferred from the relationship between p_\perp and p_x in 2.15:

$$\tan \theta = \frac{p_\perp}{p_x} \propto \frac{1}{a} \quad (2.19)$$

Nonlinear ponderomotive acceleration was profoundly studied [62] and resulted in a more detailed

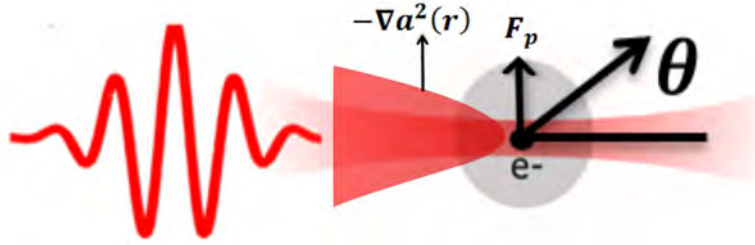


Figure 2.3: Sketch of a ponderomotively scattered electron by a focused laser beam (inspired by Fig. 3.4 in Gibbon’s book [54])

formula for θ which depends mainly on its initial velocity β_0 and the intensity of the laser:

$$\tan \theta = \frac{\sqrt{2(\frac{\gamma_L}{\gamma_0} - 1)/(1 + \beta_0)}}{\gamma_L - \gamma_0(1 - \beta_0)} \quad (2.20)$$

where $\gamma_0 = 1/\sqrt{1 - \beta_0^2}$ and $\gamma_L \equiv \langle \gamma_{L,quiver} \rangle$. For slow electrons, the scattering takes place towards to 90° .

As mentioned earlier, negligence of ponderomotive effects is one of the assumptions on which the Lawson-Woodward theorem applies. Ponderomotive accelerated electrons have been measured

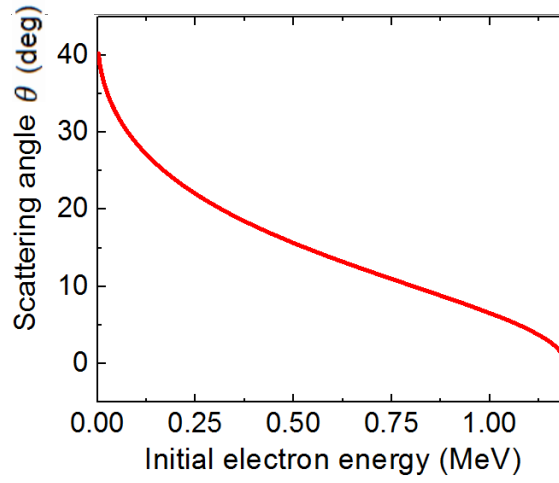


Figure 2.4: Scattering angle as a function of the electron's initial velocity, calculated from Eq.(2.20) at $a_0 = 4.5$, without cycle averaging.

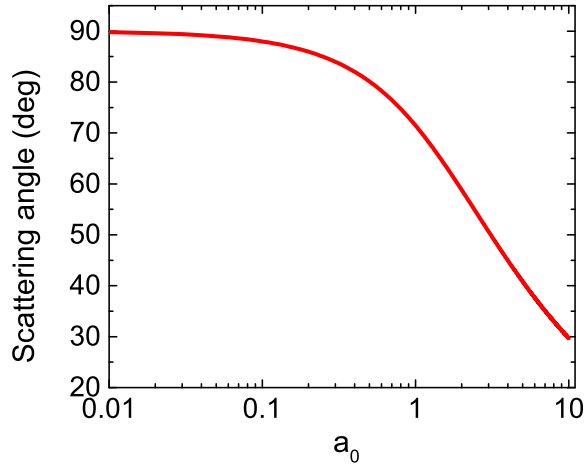


Figure 2.5: Scattering angle as a function of the normalized laser vector potential a_0 , calculated from Eq.(2.20) without cycle averaging for $\beta_0 = 0$.

by [96]. This mechanism of energy gain is very inefficient at higher electron energies due to the $1/\gamma_L$ scaling of F_p .

The classical picture of an electron quivering within the laser breaks down when the driver field is intense enough and limited to almost a single cycle. The description of the laser a_0 as a symmetric envelope is not valid and must be substituted by $a_0 \cos(\phi(t) + \varphi_{\text{CEP}})$, where φ_{CEP} is the carrier-envelope phase (CEP). This has immediate consequences on the electron's response: observables such as scattering angle or electron energy would now depend on the optical field or waveform of the driver. Such a variety of phenomena provides applicability of near-single cycle laser-driven particle sources for novel and future technologies.

2.3 Propagation of electromagnetic waves in plasmas

Gas, nano-scale targets or any material under a highly intense laser field, is ionized and becomes thus plasma. Plasmas' reaction to light, as any other material, is well described by its dielectric function, i.e. index of refraction. In this section, we explain the spatio-temporal evolution of electromagnetic waves in plasma by analyzing the changes caused by/to the laser. This is a very complex 3D process where the plasma and the laser act on each other, resulting in many phenomena which are the keys to understand further applications. Firstly, we introduce the dielectric constant ϵ according to the Drude model [109]:

$$\epsilon(\omega) = 1 - \frac{\omega_p^2}{\omega^2} \quad (2.21)$$

where $\omega_p = n_e e^2 / \epsilon_0 m_e$ is the plasma frequency, the natural oscillation frequency of electrons in a plasma of density n_e . For our analysis, temperature effects in warm plasmas will be neglected. For more information, consult ([41, 134]). The index of refraction of a plasma can be determined by solving Helmholtz Eq. in vacuum:

$$\nabla^2 \vec{E} + k^2 \vec{E} = 0, \quad (2.22)$$

where $k^2 = \omega^2 \epsilon(\omega) / c^2$. Assuming a plane wave of the type $e^{i(\vec{k} \cdot \vec{x} - \omega t)}$, the equation above yields the dispersion relationship of a wave propagating in a plasma:

$$\omega^2 = \omega_p^2 + c^2 k^2 \quad (2.23)$$

from where the laser ($\omega \equiv \omega_L$) group and phase velocity are deduced:

$$v_{gr} = \frac{\partial \omega_L}{\partial k} = c\eta, \quad (2.24)$$

being $\eta(\omega) = \sqrt{\epsilon(\omega)} = \sqrt{1 - \omega_p^2/\omega^2}$. A more exact expression is [102]:

$$\eta(r, z, t) = \sqrt{1 - \left(\frac{\omega_p^2}{\omega_L^2}\right) \frac{n_e^*(r, z, t)}{n_e \gamma_L(r, z, t)}} \approx 1 - \frac{1}{2} \left(\frac{\omega_p^2}{\omega_L^2}\right) \left(1 + \frac{\delta n_e(r, z, t)}{n_e} - \frac{a_0^2(r, z, t)}{4}\right) \quad (2.25)$$

where $\delta n_e = n_e^* - n_e$ resembles the density perturbations along the wakefield.

Before deepening into the details from Eq.(2.25), some basic concepts can be introduced with the Drude model. The density $n_e/n_c(\omega) = 1$ at which the plasma becomes reflective to an electromagnetic wave, the so so-called critical density, is $n_c = \omega^2 \epsilon_0 m_e / e^2$. In the case of our laser, $\lambda_L = 740$ nm, $n_c = 2.0 \times 10^{21}$ cm⁻³. The linear group velocity of the laser is given by $v_{gr} = c\eta \approx c\sqrt{1 - n_e/n_c}$ with a Lorentz factor of $\gamma_{gr} = \omega_0/\omega_p$, since $\eta < 1$ [33]. Laser plasma interactions are divided in underdense interactions $n_e/n_c < 1$ and overdense $n_e/n_c > 1$. Regimes such as LWFA in a gas using current CPA technology are normally realized at $n_e/n_c \approx 10^{-2} - 10^{-3}$, while solid-target experiments, $n_e/n_c \approx 10^2 - 10^3$. For both cases, the transmitted wave along the propagation direction z has the form: $e^{inz\omega_p/c}$. In the case of overdense plasmas, the index of refraction is imaginary and it results in an evanescent wave with a scale length of $\delta_p = c/\omega_p$, which is normally referred to as skin depth.

2.3.1 Underdense plasmas

Temporal changes due to density perturbations

Like any other medium, a index of refraction not equal to 1 corresponds to a dispersive material. When dealing with ultra short pulses, in particular below 5 fs, dispersion should be avoided or controlled. The group velocity dispersion GVD, $\frac{d}{d\omega} \left(\frac{1}{v_{gr}} \right)$, introduces a net second-order contribution to the Taylor-expanded wave vector $k(\omega)$, refereed as chirp β , along the plasma longitudinal extension $L_{plasma} \approx 200 \mu\text{m}$. The pulse duration of a chirped laser pulse increases in the following way:

$$\tau_{\text{CHIRP}} = \sqrt{\tau_{\text{FL}}^2 + \text{CHIRP}^2} \quad (2.26)$$

where $\text{CHIRP} = 4 \ln(2)\beta/\tau_{\text{FL}}$ for Gaussian pulses. The amount of chirp becomes critical when $\tau_{\text{FL}} \approx \text{CHIRP}$. The chirp acquired by a laser pulse of wavelength λ_L is a function of the electron density n_e :

$$\beta = \text{GVD} \times L_{plasma}, \quad (2.27)$$

$$\beta = \frac{\lambda_L}{2\pi c^2} \left[\frac{n_e}{n_c} \left(1 + \frac{3}{2} \frac{n_e}{n_c} \right) \right] \times L_{plasma}. \quad (2.28)$$

The GVD for 200 μm plasma and the critical Fourier limit pulse duration $\tau_{\text{FL}} = \text{CHIRP}$ are plotted in Fig.(2.6).

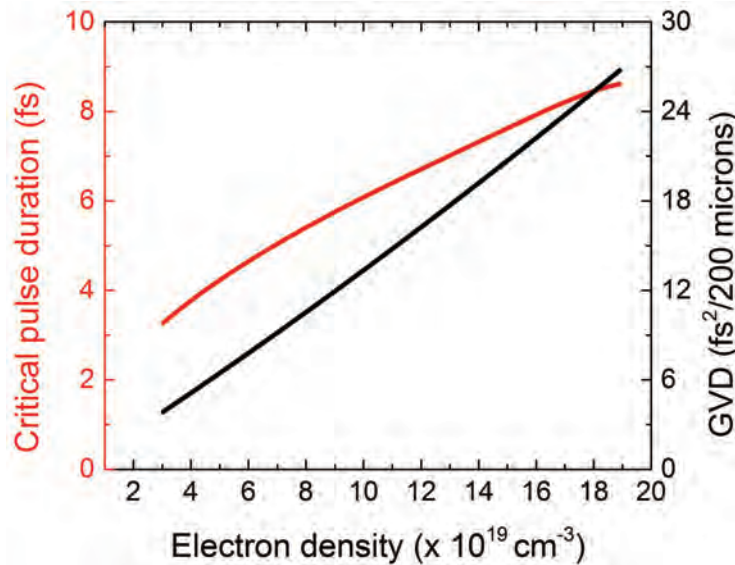


Figure 2.6: Left) Critical pulse duration at which the plasma becomes dispersive enough. Right) The group velocity dispersion (GVD) for different densities and 200 μm plasma.

In our case, for a density of 10^{20}cm^{-3} , $\beta \approx -14 \text{fs}^2$ for $L_{plasma} \approx 200 \mu\text{m}$. This amount of dispersion is already large enough to have a significant effect on a 5 fs pulse. Dispersion is a linear phenomenon and takes place regardless of the laser intensity. In the multi-dimensional

(r, z, t) scenario of a highly intense $a_0 > 1$ laser pulse focused to a gas, the laser ionizes the gas generating plasma (about 100 fs before the main peak) whereas the electrons are pushed away from highly-intense laser front via ponderomotive scattering, as explained before. Assuming a completely ionized gas, the laser front leaves an electron depleted region behind it, where $\delta n_e < 0$. Thus, the local electron density $n_e^*(r, z, t)$ has consecutively a multi-dimensional profile within the laser pulse extension, as expressed in Eq.(2.25) which modifies the spatio-temporal structure of the laser. In the temporal domain, new wavelengths are created or a complete spectral shift of the laser takes place when $\partial\eta/\partial t \neq 0$ during the pulse due to self-phase modulation:

$$\phi_L = \omega_L t - k_L z, \quad (2.29)$$

$$\frac{\partial\phi_L}{\partial t} = \omega_L - \frac{2\pi z}{\lambda_L} \frac{\partial\eta}{\partial t} \quad (2.30)$$

A local increase of the plasma density $\partial\eta/\partial t < 0$ would correspond to generation higher frequencies or blue shift, whereas an electron density depletion $\partial\eta/\partial t > 0$ would red-shift the laser pulse or allow the creation of lower frequencies spectral components. Depending on the ratio between the blow-out region and the laser longitudinal extension, there are multiple types of local density gradients in LWFA [153]: mixed (for example in SM-LWFA) or monotonic (Blow-out regime). Different spectral shifts have been reported so far in recent experiment [46]. As mentioned before, the plasma is a dispersive medium and, unlike glass, the red is slower than the blue. Therefore, continuous interplay between nonlinearities and dispersion can lead either to pulse compression or elongation [7]. As explained in the beginning of this chapter, the front of the laser pulse is constantly pushing away and accelerating electrons in the forward direction. Due to this continuous loss of energy, the front part of the laser pulse is etched away. Moreover, self-steeping also occurs due to the slow-down (negative dispersion) of the red-shifted front part of the laser due to the density depletion [92, 133, 153, 33, 157]. As a conclusion, significant nonlinearities have a direct effect the group velocity of the laser.

Spatial changes due to density perturbations

If ionization still takes place at the front part of the laser, the recent plasma will consecutively be more dense on axis and $\delta n_e > 0$. Thus, $\partial\eta/\partial r > 0$. Therefore, the difference between the phase velocities along the laser wavefront would lead to ionization de-focusing of the rest of the pulse. On the other hand, if complete ionization took place long before the main pulse, the electron-depleted region $\delta n_e < 0$ behind the laser front part has naturally a transversal profile, where $\partial\eta/\partial r < 0$ and the rest of the pulse is focused. This effect is referred to ponderomotive self-focusing which is normally only important for laser pulses that are significantly longer than the plasma wavelength. Ponderomotive forces also lead to an electron density compression in front of the pulse which, on the other hand, defocuses the front of the laser beam.

Relativistic effects

At relativistic intensities $a_0 \gg 1$, the plasma becomes also relativistic due to the inertia of the electrons. Thus, $\omega_p \rightarrow \omega_p/\sqrt{\gamma_L}$. The multidimensional dependence of γ_L is straightaway

inherited from the 4D laser profile. Therefore, $a_0 \gg 1 \rightarrow \eta \approx 1$, and the laser propagates faster where it is more intense. In the temporal domain, this leads to pulse compression via relativistic self-steepening. Furthermore, a transverse variation of $\gamma_L(r)$ leads to relativistic self-focusing $\partial\eta/\partial r < 0$, provided the most intense region is on axis. Relativistic self-focusing contributes to hinder diffraction, as long as $c\tau_L \approx \lambda_p$ and $w_0 \geq \lambda_p$. The consecutive interaction between diffraction and focusing forces for several Z_R 's is referred to as channel [148, 61]. Relativistic corrections to the index of refraction occur above a given threshold laser peak power: $P_{\text{crit}} = 17n_c/n_e[\text{GW}]$ [140]. For our LWFA experiments $< 5\%$ undercritical, $P_{\text{crit}} \approx 0.3 \text{ TW}$, while the employed effective peak power was $P \approx 1 \text{ TW}$. Self-focusing $\frac{P}{P_{\text{cr}}} \leq 3$ is still considered within the weakly non-relativistic scenario[121]. On the other hand, the ponderomotively-triggered density compression in front of the laser pulse causes a decrease in the index of refraction which compensates the self-focusing relativistic corrections [136, 57]. Due to this compensation, low intensity ($a_0 < a_{0,\text{cr}} = (\omega_p\tau_L)^{-1}\sqrt{4\ln(2)/[1+(k_p w_0/4)^2]}$) Gaussian laser pulses ($a_{0,\text{cr}} \approx 1.3$ for our $< 5 \text{ fs}$ laser experiments), yet $\frac{P}{P_{\text{cr}}} > 4$ due to the low density, which are not too-tightly-focused ($k_p w_0 > 2\pi$) in tenuous plasmas ($\omega_p\tau_L < 1$) behave as if in vacuum, where nonlinearities have not yet produced effects on the pulse shape. Slightly above-threshold $\frac{P}{P_{\text{cr}}} \geq 1$ short pulses $c\tau_L < \lambda_p$ cannot self-guide since the index of refraction has an own time scale of ω_p^{-1} . The local group velocity of the laser depends naturally on the laser parameters as well. A perturbative study [133] yielded that the group velocity Lorentz factor $\gamma_{gr,NL} \approx \gamma_{gr} \times (1 + 0.088a_0^2)$, in a case of a resonant Gaussian pulse in the linear regime ($a_0 \ll 1$).

2.3.2 Overdense plasmas

Plasma scale length

According to Eq.(2.1), ionization of solids already takes place at intensities around 10^{15} Wcm^{-2} . Actually, MI processes take the lead and start ionizing the material even at lower intensities 10^{12} Wcm^{-2} . In any case, this means that plasma is already generated much before (≈ 100 's fs) the main laser peak arrives (see section 1.1.2). Plasmas expand at roughly the speed sound:

$$c_s = \left(\frac{Z^* k_B T_e}{m_i} \right)^{1/2} = 3.1 \times 10^7 \left(\frac{T_e}{\text{keV}} \right)^{1/2} \left(\frac{Z^*}{A} \right)^{1/2} \quad (2.31)$$

where k_B is the Boltzmann constant, T_e is the electron "temperature" and m_i is the ion mass. The plasma density profile is thus exponentially decaying, at a scale length $L = c_s t$, assuming the plasma expands isothermally [85], as illustrated in Fig.(2.7). Taking into account the intensity contrast, $10^{-4} - 10^{-5}$ at 1 ps, the electron temperature is about 0.1-1 keV and $Z^* \approx 10 - 20$ from Eq.(2.1), resulting in $L \approx (0.01 - 0.1)\lambda_L$. At poor contrasts, 10^{-5} at 10's of ps, $L > 2\lambda_L$. The level of energy contained in such intensity pedestals caused by ASE results fatal for plasma confinement within $\ll \lambda_L^3$, such as nanoscale targets. Uncontrolled expansion of the target due to early ionization leads to a decrease of the plasma density which increases the original skin depth. For this reason, in laser-solid experiments, techniques such as XPW or a plasma mirror are implemented to improve and control the high dynamic range temporal contrast of the laser pulses. In our case, about 10^7 at 5 ps before the main peak. Access to the laser contrast is thus key to all solid-target experiments.

Skin depth

As explained in section 2.3, the laser field cannot propagate inside an overdense plasma, only up to the skin depth $\delta_p = (\lambda_L/2\pi)\sqrt{n_c/n_e}$. For a $100 n_c$ solid target, $\delta_p \approx 12$ nm at $\lambda_L = 740$ nm. In the limit of $L \rightarrow 0$, an incoming electric field E_z encounters a target at $x = 0$ with a plasma profile which resembles a Heaviside function, as shown in Fig.(2.8). The "transmitted" wave through such plasma is an evanescent field:

$$E_{\text{skin}} = E_z(x = 0) \exp(-x/\delta_p) \quad (2.32)$$

Depending on the application, this may or not be the ideal situation.

Relativistic transparency

In a similar fashion as in section 2.3.1, relativistic corrections to the electron density results in changes in the refraction index of the plasma and in the skin depth. Thus, an extremely intense light pulse can propagate in a overdense plasma for intensities above a critical value $a_{0,cr}$ where $\omega_p/\sqrt{\gamma_L} \leq \omega_L$:

$$a_{0,cr} \geq \sqrt{2} \frac{n_e}{n_c} \quad (2.33)$$

The equation above applies in the case of a semi-infinite Drude plasma. A laser of $a_0 \approx 1000'$ is still far away from being constructed, though. Nevertheless, spherical targets of dimensions $R \gg \delta_p$, can become transparent to an intense laser pulse if $R \approx \delta\sqrt{\gamma_L}$. Thus, an effective skin depth $\delta_p \rightarrow \delta_p\sqrt{\gamma_L}$, would enable the laser to propagate completely through a nano-scale target of about $\ll \lambda_L$ nm size as seen in Fig.(2.9), interacting with almost all the target particles [54, 36].

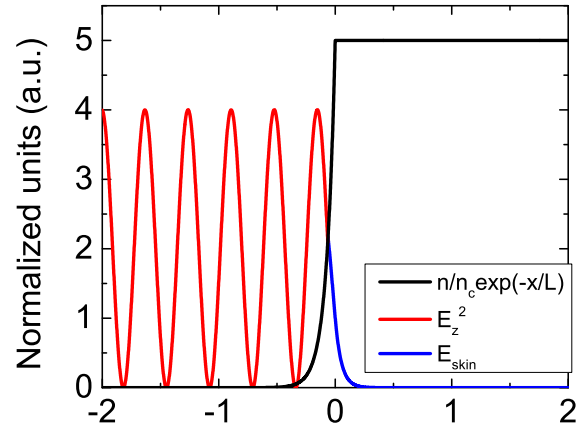


Figure 2.7: Normalized incident electric field in an overdense plasma with $n/n_{cr} = 5$ and $a_0 = 2$ with plasma scale length $L = \lambda_L/10$ and no relativistic corrections.

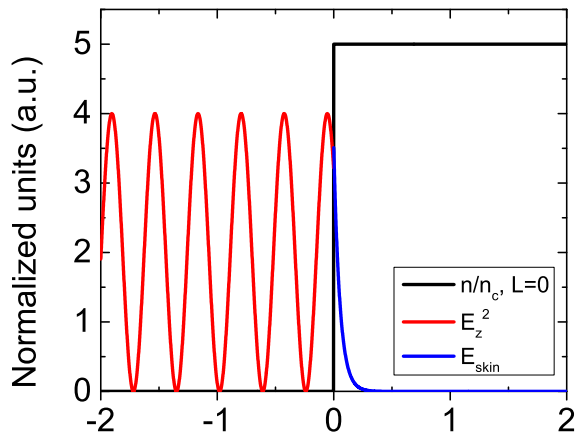


Figure 2.8: Normalized incident electric field in an overdense plasma with $n/n_{cr} = 5$ and $a_0 = 2$ with no plasma scale length and no relativistic corrections.

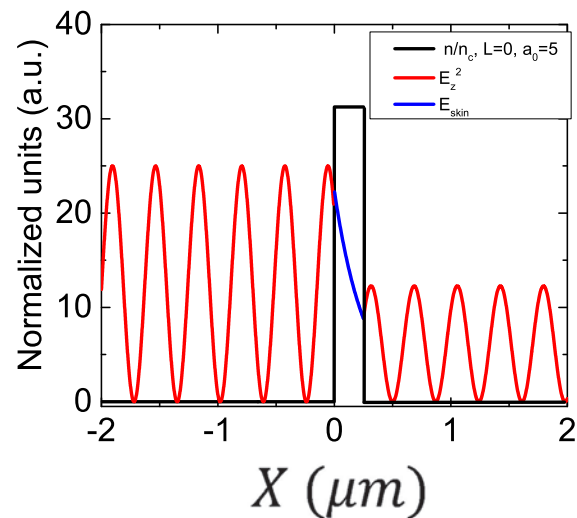


Figure 2.9: Normalized incident electric field in an overdense plasma 250 nm thick with $n/n_{cr} = 5$ and $a_0 = 5$ with no plasma scale length and relativistic corrections.

2.4 Particle-in-cell simulations (PIC)

In the last section of this chapter, we will briefly comment on the theoretical and computational tools to obtain a deeper knowledge of the experiments, particularly in laser-plasma interactions. Plasma's fluid nature can be routinely simulated. Yet, for most highly intense laser-plasma applications, a hydrodynamic description fails to describe processes such as "self-injection" or "particle trapping" in laser accelerators (see sec.3.1 in the following chapter). Large amplitude plasma waves tend to break releasing high energy particles whose motion cannot be described by a fluid modeling. These particular interactions cover a range of densities between $10^{16} - 10^{26} \text{ cm}^{-3}$ at electron's temperatures ranging over more than 7 orders of magnitudes. These scenarios involve an extraordinary number of particles, e.g. $N \approx 10^{11}$ for 10^{24} cm^{-3} in a volume of only λ_L^3 . In order to speed up time and save computational resources, Particle-in-cell (PIC) simulations handle with a statistically significant number of "macroparticles" distributed in different "cells" of a 2 or 3D grid instead ($\approx 1 \times 10^8$ electrons, which represent many particles simultaneously). The motion of an electron in an electromagnetic field, as viewed in sec.2.2, is ruled by Lorentz Equation 2.9, which is invariant for the mass charge ratio of the particle. Therefore, such macroparticles will behave similarly as the real particles. The macroparticles are originally initialized on a grid, where the current j_k and charge density ρ_k are calculated. Secondly, the electric E_k and magnetic B_k fields are solved through the Maxwell Eq. 2.7 all over the grid. As a final step, the macroparticles motion is derived in a chronological way $k \rightarrow k + 1$ at time steps of δt by solving the Lorentz Equation numerically. Iteration of these last three steps throughout the whole simulation box results in a fully-relativistic calculation of the macroparticles momenta and position in the phase space.

Different codes have been developed by different groups around the world. Some examples are: Virtual-laser-plasma laboratory (VLPL) [120], VORPAL [107] or EPOCH [36]. Laser-plasma physics at relativistic intensities and near-critical plasmas $0.1n_e/n_c$ or in overdense scenarios is extremely rich and a variety of different phenomena take place. PIC simulations provide the scientific community a tool to understand the dynamics of any interaction. Figures 2.10a, 2.11a and 2.12a show different scenarios where PIC codes are applicable. Figure (2.10a) shows the interaction between a nano-scale needle with a extremely intense laser field. Electric and magnetic fields as well as the charge distribution across the whole grid is retrievable. Underdense applications, such as laser-driven plasma accelerators, can also be well simulated, as shown in Fig.(2.11a). Particle-in-cell codes often resemble the experimental data well in terms of electron peak energy, but not in terms of charge, as well displayed in Fig.(2.12a).

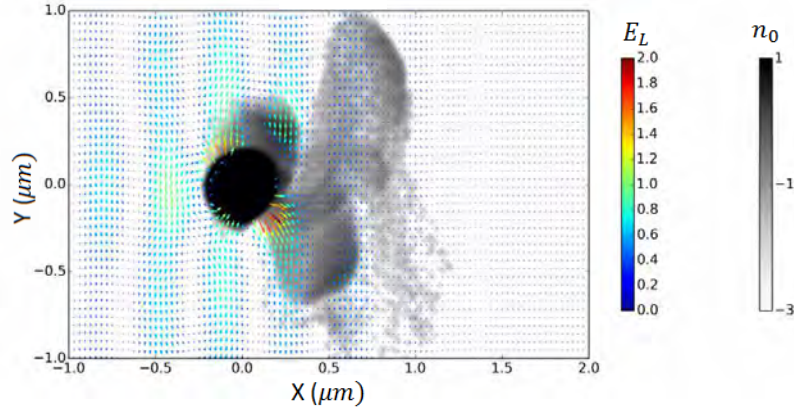


Figure 2.10: Normalized radial electric field and log-distribution of the electron distribution emitted from a 200 nm $100 n_e/n_{cr}$ solid target under the influence of a highly intense $a_0 = 4.5$, 4.5 fs laser pulse, calculated using EPOCH code. A full analysis is found in chapter 4.

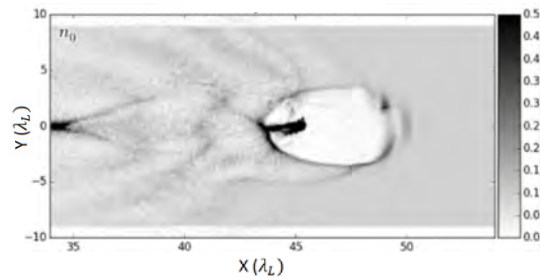


Figure 2.11: Snapshot of a strongly broken plasma wave driven by an ultra-intense $a_0 = 7.5$ fs pulse through a $0.1 n_e/n_{cr}$ gas target. This ion cavity propagating with the laser field is referred to as "bubble". Learn more about laser-driven plasma waves and their capabilities to accelerate particles in the next chapter. Simulations done by Longqing Yi using VLPL code.

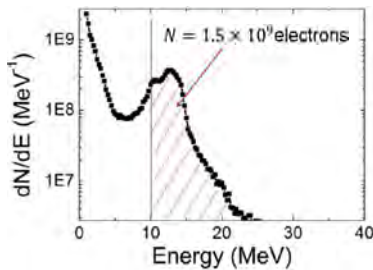


Figure 2.12: Electron spectrum out of the interaction in the case above (Fig.(2.11a)).

Chapter 3

Laser wakefield electron acceleration

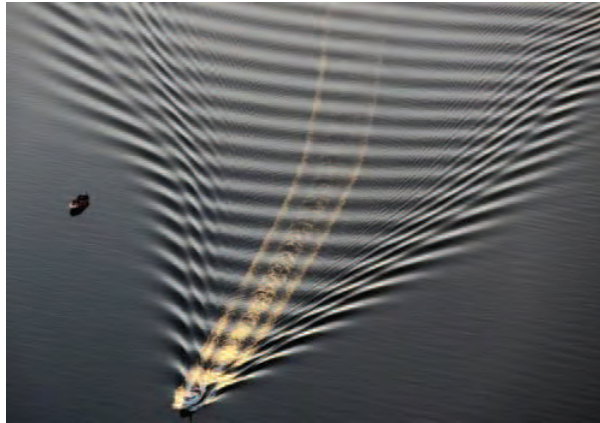


Figure 3.1: Boat-driven wake.

Highly intense laser-plasma physics have various applications [54], some of which are even capable to compete against very-well known and state-of-the-art conventional technology. Plasmas have the advantage to support enormous electric fields under which normal matter breaks down. In the previous chapter sec.2.2.1, we introduced the ponderomotive force of a highly intense laser pulse. In an underdense plasma (see sec.2.3), a propagating intense enough pulse pushes electrons out of the most intense regions, in a rather mechanical fashion. Similar to the wake generated by a boat at sea shown in Fig.(3.1), the laser generates large amplitude density perturbations, which can sustain electric fields E_{plasma} much larger than current accelerators (10 – 50 MV/m). Moreover, an electron can actually "surf" the "plasma waves" generated by the laser for a distance L_{surf} and gain the corresponding energy $eE_{\text{plasma}} \times L_{\text{surf}}$. Although "plasma waves" have been studied for a long time, the picture of a surfing electron in a laser-driven wake was first published by [144]. This energy gain mechanism is referred to as Laser wakefield acceleration (LWFA) and in the first section of this chapter sec.3.1, we will introduce the needed theoretical knowledge to understand and interpret the experimental results presented later in this work in sec.3.3. In sub-sec.3.1.1, we will first explain how the wake is generated and how large can E_{plasma} be. Afterwards, we will specify the conditions under which an electron can actually "surf" in sub-

sec.3.1.2, followed by different estimations on L_{surf} as well as the electron's maximum energy gain according to different theories in sub-sec.3.1.3. We will make emphasis in sub-sec.3.1.4 on how the injection of the surfing electrons into the wave is optimized by tailoring the plasma density profile, e.g. "the sea level". To conclude the theoretical introduction, we will briefly comment on the feedback-effect of "surfer" on the wave and on the acceleration in sub-sec.3.1.5. As a short remark for this chapter, the plasma temperature is not taken into account and rather "cold" electrons are always assumed until the moment they start to "surf".

3.1 Basics of LWFA

3.1.1 Wakefield generation and wavebreaking limit

Excitation of collective motion of electrons in plasmas is possible by focusing a laser pulse of frequency ω_0 and duration τ_L into an underdense plasma of density n_e . The Poisson equation is used to determine the static potential ϕ along the density perturbations in the plasma. Starting from the Maxwell, Lorentz and the continuity equation, analytical expressions for the normalized density $n = n_e/n_0$, electron fluid velocity \mathbf{u} and the scalar potential ϕ are summarized in a ordinary differential equation for ϕ . The combined action of the laser ponderomotive force and space-charge effects between electron and ions generates electron sheaths propagating behind the laser with a phase velocity $v_{ph} = \omega_p/k_p$, which is equal to the laser pulse group velocity v_{gr} . Such a coherent structure is called the wakefield or plasma wave. In the quasi-static approximation where all quantities depend only on the co-propagating variable $\partial/\partial\xi$ and not on time $\partial/\partial\tau \approx 0$, the final expression for the ϕ is written as [41, 54]:

$$\frac{\partial^2 \phi}{\partial \xi^2} = k_p^2(n - 1) = k_p^2 \gamma_p^2 \left\{ \beta_{ph} \left[1 - \frac{\gamma_{\perp}^2}{\gamma_p^2(1 + \phi)^2} \right]^{-1/2} - 1 \right\} \quad (\text{Poisson eq.}) \quad (3.1)$$

where $\gamma_{\perp} = 1 + u_{\perp}^2 = 1 + a^2$, $\gamma_p = (1 - \beta_{ph})^{-1/2}$ and $\beta_{ph} = v_{ph}/c$. The other variables, together with the laser pulse a , are then related between each other through algebraic expressions obtained from:

$$u_{\perp} = a_{\perp} \quad (\text{from Lorentz eq.}) \quad (3.2)$$

$$\gamma_p - \beta_{ph} u_z - \phi = 0 \quad (\text{from Lorentz eq.}) \quad (3.3)$$

$$n(\beta_{ph} - \beta_z) = \beta_{ph} \quad (\text{from continuity eq.}) \quad (3.4)$$

where $\beta_z = u_z/c$. From the equations above, numerical solutions are found for the plasma variables for a given density and laser parameters. See Fig.(3.2). For very low laser intensities, the solution for the potential ϕ , field $\left(\propto -\frac{\partial \phi}{\partial \xi}\right)$ and charge perturbation $\left(\propto \frac{\partial^2 \phi}{\partial \xi^2}\right)$ is a sinusoidal one. The separation between the electron spikes is the plasma wavelength $\lambda_p[\mu\text{mu}] = 3.3 \times 10^{10}/\sqrt{n_e}[\text{cm}^{-3}]$. For higher laser intensities and electron densities, the electric field originated between these electrons sheaths can reach levels as large as 100-1000 GV/m. The amplitude of such a wake, for a constant laser intensity, reaches its maximum under resonant conditions, that is

to say, when the laser pulse duration is approximately the half of plasma wavelength, $c\tau_L \approx \lambda_p/2$. Assuming all electrons oscillate at ω_p in a cold plasma in one spatial dimension, where the thermal electron energy is negligible, the magnitude of this field is given by the expression

$$E_{\text{WB}}[\text{Vm}^{-1}] = cm_e\omega_p/e \approx 96\sqrt{n_e(\text{cm}^{-3})} \quad (3.5)$$

where E_{WB} is referred to as cold-wavebreaking field. More accurate expressions can be found in [41] taking into account relativistic effects, $E_{\text{WB}} \rightarrow E_{\text{WB}}\sqrt{2(\gamma_{ph} - 1)}$, where $\gamma_{ph} \approx \gamma_{gr} = \omega_0/\omega_p$. An initial plasma temperature would also decrease the value of E_{WB} , according to [134]. The magnitude of this field will be used only as a reference and therefore Eq.(3.5) is enough to describe the processes treated in this work. Moreover, electric fields higher than Eq.(3.5) have been observed in PIC simulations in a highly nonlinear 3D scenario [121, 152]. This, however, exceeds the content of this thesis. Relativistic effects such as the increase of the electron mass at high intensities is visible in Fig.(3.2). One example is the elongation of the plasma wavelength $\lambda_p \rightarrow \lambda_p\sqrt{\gamma_{ph}}$ which is pronounced at intensities beyond $a_0 > 4$, as seen in Fig.(3.2).

The coherence or the structure of the plasma wave is broken when the electron displacement exceeds the plasma wavelength. Wavebreaking occurs when the plasma sheaths become extremely dense (see $a_0 > 4$ in Fig.(3.2)) and the amplitude of the field exceeds E_{WB} ; in this case, the wave crashes in a similar fashion as the ocean waves at shore. This is referred as wavebreaking limit: the maximum amplitude of an electrostatic standing wave allowed within the fluid model [41]. The presented 1D fluid model starts to be invalid for $a_0 \gg 1$. Due to the multi-dimensional structure of the wakefield and the laser pulse, more correct amplitudes of the wavebreaking field were obtained in PIC simulations. In a 2D or 3D scenario, the curvature of the plasma sheaths due to a density depletion or relativistic electron mass increase on axis leads to intersections between the electron trajectories and eventually causes wavebreaking at a certain distance behind the driver at lower electric fields in comparison with the 1D case [17]. Fast electrons whose displacements exceed the plasma wavelength would leave the plasma wave and fall in the accelerating region of the electric field. The excitation of very large electrostatic waves takes place in a regime close to the wavebreaking limit and therefore it is of high interest.

3.1.2 Electron injection into the wakefield

An accelerator propagating with the speed of light is the result of wakefield excitation. There are different ways to inject fast electrons into the accelerator. Injection means to place externally or internally an electron bunch in the correct phase of the longitudinal field. Injection should be done very close to the rear of a plasma period where the acceleration is the strongest. Trapping and therefore energy gain, however, occurs when this bunch has an initial velocity higher than the wakefield itself $v_e > v_{ph}$. Trapping can therefore occur at any position in the accelerating phase and not necessarily where the acceleration is the strongest. If the injected electron has not enough momentum, it will only slip backwards with respect to the wakefield and remain untrapped and the leaves the plasma period. A trapped electron bunch would have thus a longitudinal dimension of $< \lambda_p \approx \text{few} - \text{fs}$, as measured by [13, 93].

In order to inject and fulfill the trapping conditions, different ways have been studied following two main directions: either putting more energy into the background plasma to heat the injected

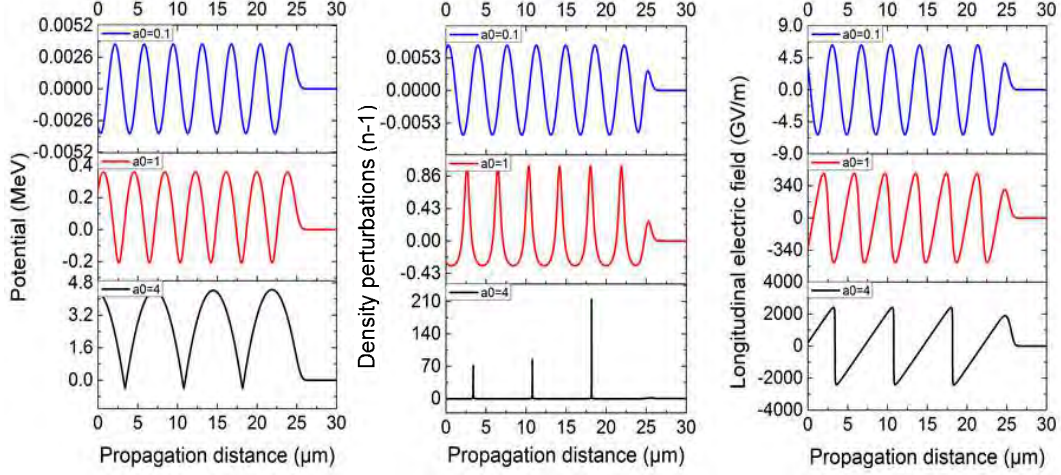


Figure 3.2: One-dimensional wakefield in the quasi-static approximation. Simulation parameters: $8 \times 10^{19} \text{ cm}^{-3}$, $\tau_L = 5 \text{ fs}$.

electrons, such as colliding-pulses injection[48], decreasing the phase velocity of the accelerator, such as down-ramp injection [17], or injecting the electrons at the correct phase such as ionization injection [26] and the one presented in this work: sharp-density transition, the so-called, shock-front injection [131]. All these technologies were developed in order to avoid wavebreaking. In the latter case, some few fast electrons stay in the plasma wave and have enough momentum ($v_e > v_{ph}$) to get self-trapped in the accelerating phase. This process is named self-injection. Self-injection is an extremely non-controlled process. Some degree of tunability is obtained, at least, by changing the background density and target size [51, 5]. However, these parameter also influence the acceleration and the final electron parameters. This fast-dynamic process depends highly on the local properties of the density and the laser along the propagation length. At these high intensities, stopping the injection of unwanted electrons becomes critical and hard to realize [77]. In particular the absolute energy spread ΔE and the dark current, exceed the values obtained with external injection mechanisms and in a large proportion the level of conventional accelerators. This type of injection relies, as no other injection method does, on the laser performance, intensity and nonlinearities taken place in the plasma.

Trapping conditions and the electron evolution in the plasma wave is described by the Hamiltonian [40]

$$H(\tilde{p}, \xi) = \sqrt{1 + \tilde{p}^2} - \beta_{ph}\tilde{p} - \phi(\xi) \quad (3.6)$$

where $H(\tilde{p}, \xi) = \text{const}$ represent electron trajectories. In particular, the separatrix $H(\tilde{p}, \xi) = H(\tilde{p}_{ph}, \xi_{min})$, where $\phi(\xi_{min}) = \phi_{min}$, distinguishes the trapped electron orbits from the non-trapped. In a sinusoidal potential $\phi = \phi_0 \cos \psi$, where $\psi = k_p \xi = k_p(z - v_{ph}t)$ is the phase, the region $-\pi < \psi < 0$ is accelerating for negative charged particles while from region $0 < \psi < \pi$ is decelerating. In Fig.(3.3), the phase space is plotted and the trapped trajectories are red-filled. From the plot, two facts are clear: (i) the trapping condition (in this case, $p_{ph} \approx 4.5 \text{ mc}$ for the simulation parameters; and (ii) the energy gain limitation, $\tilde{p}_{max} \approx 20$.

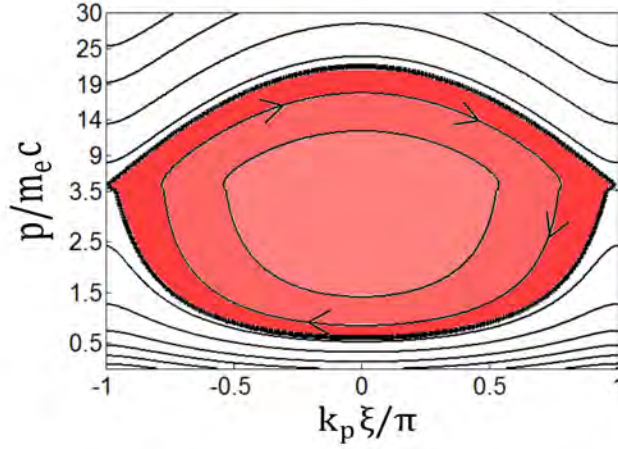


Figure 3.3: Phase space diagram following the Hamiltonian in Eq.(3.6). Simulation parameters: $8 \times 10^{19} \text{ cm}^{-3}$, $\tau_L = 5 \text{ fs}$.

3.1.3 Electron energy gain limitations

Eventually, the electrons propagate much faster speed than the laser group velocity and the wakefield itself: $\tilde{p}_{\text{max}} \gg \tilde{p}_{\text{ph}}$. Beyond the distance at which the electron surpasses the accelerating region, it starts to decelerate. This phenomenon is called dephasing. In the linear regime, $a_0 = 0.1$ in Fig.(3.2), the slippage from the accelerating and focusing region takes place at $\lambda_p/4$ [41]. In a weakly nonlinear regime ($a_0 \approx 1$), the field is no longer sinusoidal but rather linear within a plasma period. Thus, phase slippage occurs at $\lambda_p/2$. The time at which dephasing occurs depends on the wake phase velocity v_{ph} . In a 1D linear scenario, v_{ph} was shown to be equal to the laser group velocity $v_{gr} = c\eta = c\sqrt{1 - n_e/n_c}$ to order $O(a_0^2)$ [133], which mainly depends on the laser dispersion in the plasma and therefore in the electron density. At high intensities when a_0 approaches 1, this is no longer valid and nonlinear corrections to the phase velocity must be taken into account. Thus, $\gamma_{ph,NL} = \gamma_{gr}(1 + 0.10a_0^2 - 0.12a_0^4 + 0.05a_0^6)$ for $a_0 \ll 1$ for a resonant Gaussian pulse. Due to the laser and density parameters of our experiments, this work lays on a transition between a linear and nonlinear scenario. Therefore a weakly nonlinear plasma wave is assumed and $v_{ph} \approx v_{gr}$. In the laboratory frame, the distance at which dephasing manifests is $L_d = c\tau_d$:

$$\frac{L_d}{v_{ph}} - \frac{L_d}{c} = \frac{\lambda_p/2}{c}, \quad (3.7)$$

$$\Rightarrow L_d \approx \frac{\lambda_p/2}{1 - \eta}, \quad (3.8)$$

$$L_d \approx \frac{\lambda_p/2}{(1 - (1 - 1/2\lambda_0^2/\lambda_p^2))}, \quad (3.9)$$

$$L_d \approx \lambda_p^3/\lambda_0^2. \quad (3.10)$$

Following Eq.(3.10), a basic estimation of the maximum obtainable electron energy from an

accelerator scales as:

$$E_{max} = eE_{WB}L_d, \quad (3.11)$$

$$\propto \omega_p \lambda_p^3, \quad (3.12)$$

$$\propto \lambda_p^2 (\propto \tau_L^2) \quad (3.13)$$

Different laser parameters lead to different scenarios (see TABLE I. in [92]). In the blow-out regime, not only the wake phase velocity is important but the dynamics of the bubble are as well taken into account. In this case of high intensities, relativistic corrections to the plasma period, nonlinearities such as self-etching and multi-dimensional effects are taken into account and a new formula is derived:

$$L_{d,3D} = \frac{4}{3} \sqrt{a_0} \frac{\lambda_p^3}{\lambda_0^2}. \quad (3.14)$$

Dephasing is an intrinsic energy limitation of the accelerator: an infinitely long accelerator would yield the same electron energy as an accelerator with a length of L_d . Due to the extreme scaling, the dephasing length L_d is in the order of 10-mm's ($n_e \approx 10^{18} \text{ cm}^{-3}$) to m's ($n_e \approx 10^{17} \text{ cm}^{-3}$). In resonant plasmas, dephasing within 100 μm is only possible employing laser pulses about 5 fs duration.

Other limitations which hinder the dephasing are the extinction of the wakefield. This is caused by a reduction of the driver's intensity: either by diffraction or by energy depletion. The diffraction of the laser is characterized by the confocal length $b = 2Z_R = 2\pi w_0^2/\lambda_0$. In plasmas, self-focusing can lead to optical guiding of the laser pulse, as mentioned in sub-sec.2.3.1. Such a guiding is induced by transverse shaping of the index of refraction caused by: externally tailored-density channels, density laser-induced blow-out or relativistic increase of the electron mass when $a_0 \gg 1$. Keeping the laser intensity high along several Z_R is a requirement nowadays to reach GeV level [90, 89], unless the laser is of PW-level and the beam waist is multi-100's μm [57]. Laser diffraction and plasma lensing are neutralized producing a very long ($\gg Z_R$) plasma channel at a given so-called "matched laser focal spot" w_{match} [148].

Finally, the generation of the wakefield consumes the laser energy. The official definition of the depletion length L_{dp} is the distance at which the laser has lost half of its energy in the wakefield generation. Theoretical studies predict that $L_{dp} \propto 1/a_0^2$ for weakly relativistic interactions while $L_{dp} \propto a_0$ for $a_0 \gg 1$ [41]. Matching the depletion length and the dephasing length is the goal of large accelerators employing big laser systems, though at high intensities, $a_0 \gg 1$, depletion becomes significant since laser-electron interactions are more strongly coupled. Depletion-limited accelerators turn to be more efficient. Theoretical estimations reach even 20% conversion efficiency [121]. Current state-of-the-art systems reach GeV-level acceleration but at efficiencies about 1%. In our experimental case, this limitation proved to be negligible.

More robust and detailed scaling laws have been published by Lu [92] and GP [58] for self-trapped particles in the wakefield. Each of these studies and predictions has their own limitation. In the case of Pukhov, the acceleration reaches an end after total consumption of the laser energy at very high intensities. Lu's work addresses longer lasers and lower intensities. In the latter work, the prediction for the maximum obtainable electron energy is limited by an earlier

dephasing due to self-etching at the front of the pulse. In this thesis, the blow-out scaling laws will be only presented for comparison purposes, since the applied intensities are far below the threshold $a_0 > 4$. Nevertheless, the theoretical predictions provide a good reference value for the maximum obtainable electron energy and for the laser spot size in to operate the accelerator without significant laser-diffraction limitations, at least up to 2-3- Z_R .

In a fully 3D highly nonlinear regime, treated in GP's work, the final electron energy is given by the formula:

$$E_{max} \approx 0.65mc^2 \sqrt{\frac{P}{P_0} \frac{c\tau_L}{\lambda_0}} \quad (3.15)$$

where $P_0 = m^2c^5/e^2 = 8.7$ GW. In this thesis, the applied peak power was about 3 TW within the spatial FWHM from 9 TW on target using the sub-5 fs laser system. Eq.(3.15) leads to a final energy of 12 MeV. This formula does not scale with the laser pulse duration $\sqrt{\tau_L}$ as Eq.(3.13), τ_L^2 . In GP's work, the pulse duration must only fulfill $c\tau_L < R$, where $R \approx k_p^{-1}\sqrt{a_0}$ is the bubble radius. Since R is linked naturally to the plasma wavelength, the upper limit of the electron density is determined by the pulse duration whereas the minimum density limit corresponds to a matched bubble radius so that the interaction is still relativistic, i.e. $a_0 > 1$.

$$n_c \frac{P_0}{P} < n_e < n_c \sqrt{\frac{P}{P_0} \frac{1}{(\omega_L \tau_L)^3}} \quad (3.16)$$

From the density interval displayed above, it can be deduced that a threshold laser power of $P > P_0(\omega_L \tau_L)^2$ is needed for acceleration to take place. For our experimental conditions, around 1 TW peak power should suffice the laser requirements.

In Lu's work, the energy gain is given by the expression:

$$E_{max} \approx \frac{2}{3}mc^2 \left(\frac{\omega_0}{\omega_p}\right)^2 a_0 \approx mc^2 \left(\frac{P}{P_0}\right)^{1/3} \gamma_p^{1/3}. \quad (3.17)$$

which also leads to 10 MeV in the sub-5 fs experimental conditions at $1 \times 10^{20} \text{ cm}^{-3}$. Lu's prediction has a similar scaling on λ_p as Eq.(3.13), apart from the factor corresponding to the laser intensity, a_0 . Both expressions Eq.(3.15) and Eq.(3.17) assume that the laser pulse spot size w_{match} ($1/e^2$) equals the bubble radius R . In both of these studies, the ponderomotive force of the laser $k_p \nabla a_0^2 / \gamma_\perp$ equals the space charge force of the ion cavity $k_p R$. Therefore, $k_p R \approx k_p w_{match} \approx \sqrt{a_0}$. The matched laser spot size can be rewritten in a more comfortable way: $d_{match}^{FWHM} \approx 0.85^{-1} \lambda_p \sqrt{a_0}$, and it is $\approx 5.5 \mu\text{m}$ for the sub-5 fs case ($a_0 \approx 2$ and $\lambda_p = 3.3 \mu\text{m}$). Theoretical predictions for the amount of charge accelerated ($\approx \text{nC}$) are far off the so far observed in the experiments (≈ 10 's pC).

3.1.4 Externally injected electron beams: shock front

In order to reach the quality provided by conventional technology using laser-plasma accelerators, not only aiming for higher electron energies should be the main goal but special attention should be also put to the electron parameters such as energy spread, emittance, charge, stability, tunability, among others. As it was hinted previously, fulfilling the trapping conditions can be achieved by tailoring the plasma density profile, without utilizing wavebreaking and

self-injection. A long ($\gg \lambda_p$) down-ramp reduces slowly the phase velocity of the wakefield: $\beta_{ph} \approx \beta_{gr}(1 + |\xi|\lambda_p^{-1}d\lambda_p/dz)^{-1}$ [56]. Electrons from the plasma background get trapped continuously [17]. As it will be shown later, the wakefield can be very well approximated to a weakly nonlinear accelerator in the laboratory frame. Therefore, continuous injection is translated in a broader energy spread in the generated electron beam. A sharp density transition ($\ll \lambda_p$), on the other hand, results in a sudden injection localized in space and time. In a two-density plasma profile, where $n_1 = \alpha n_2$ (α typically 1-2, the relative change in the plasma wavelength and in the phase velocity are given by:

$$\frac{\Delta\lambda_p}{\lambda_{p,1}} = \frac{\lambda_{p,2}}{\lambda_{p,1}} - 1 \approx \sqrt{\alpha} - 1, \quad (3.18)$$

$$\frac{\Delta v_{ph}}{v_{ph,1}} = \frac{\beta_{ph,2}}{\beta_{ph,1}} - 1 \approx \left(1 - \frac{1}{2} \frac{n_1}{n_c}\right) \left(1 + \frac{1}{2} \frac{n_2}{n_c}\right) + O\left(\frac{n_1}{n_c}\right) \approx \frac{n_2(\alpha - 1)}{2n_c} + O\left(\frac{n_1}{n_c}\right). \quad (3.19)$$

From the expressions above, it is clear $\Delta\lambda_p/\lambda_{p,1} \gg \Delta v_{ph}/v_{ph,1}$, indicating that plasma wavelength abruptly increases. The trapping mechanism of shock front works the following way: A wakefield is generated at the density region n_1 in a regime where wavebreaking is avoided. The relative position between the first plasma sheath (orange-filled in Fig.(3.4)) and the laser $\xi_1 \approx \lambda_{p,1}$ remains invariant after the density transition, whereas "the bubble" or the first period after the laser expands suddenly in the second density region as the wakefield is being generated ($1 \rightarrow 2$). By such a sharp density transition, the cold electrons from the sheath in the first region are automatically localized somewhere in the accelerating region of the wakefield (3). Most of the injected thermal electrons start to accelerate but do not fulfill the trapping conditions and correspondingly fall back (4). After intense dynamics and space-charge effects, only a portion of the initially injected electron bunch will finally get trapped and accelerated. This easy but effective method has proved to work using long (≈ 30 fs [14]) as well as short < 10 fs laser pulses [132].

The exact injection position within the first plasma period behind the laser on the second density region is determined by: $\xi_{inj} = \lambda_{p,1}$. The density ratio is limited to $\alpha < 4$, otherwise the injection position is localized where the longitudinal field is decelerating. For all of the experiments, unless specified otherwise, $\alpha \approx 1.6-2$. Moreover, it has been observed experimentally that shock-front injected electron beams reach the same output energy as the self-injected ones [24]. This is a clear proof that most of the injected electrons fall back with respect to the wakefield and get trapped almost at the end of the bubble.

3.1.5 Beamloading

Beamloading is referred to as the change in the plasma electric field E due to the presence of a highly "loaded", i.e. high charge, electron beam. Its maximum value E_{max} , as well as its slope $dE/d\xi$ may be altered, influencing directly the accelerated beam parameters. A decrease of longitudinal field results immediately in a lower electron peak energy. Nevertheless, a change in the slope across the beam's longitudinal extension may even result in an optimized and reduced absolute energy spread ΔE . High loads produce the so-called "field flattening" ($dE/d\xi \approx 0$), or in an extreme case, "field reversing" ($dE/d\xi < 0$). For low charges and ($dE/d\xi > 0$), the trailing

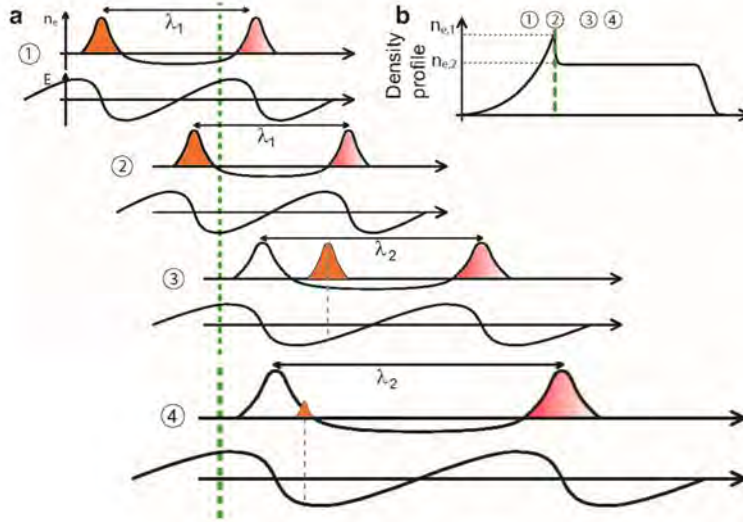


Figure 3.4: Injection and trapping mechanism using a sharp density down-ramp transition: shock front. This is inspired in Fig.(1.10) from [12].

and front part of the electron bunch are under the presence of different values of E , resulting in an unavoidable energy spread. An optimal balance between injected charge, electron peak energy E_p and absolute energy spread is found during the "field flattening". For even larger loads, the latter improvement is reversed and the output ΔE results even larger as in the low charge case. In order to take advantage of these effects, a detailed and controlled injection is required. It is intuitive that the accelerator's design determines whether to produce low charge $Q_1 < Q_2$ high peak energy $E_{p,1} > E_{p,2}$ beams or vice versa. Beamloading was studied theoretically and experimentally [160, 154, 123, 124]. Assuming a sinusoidal wake and an injected beam of charge $q = -eN$ of a cross section A which produces a density perturbation of δn , the total field in the plasma $E = E_{wake} + E_{beam}$ cancel each other for charges above $N \approx 1.5 \times 10^8 / \sqrt{n_e [10^{18} \text{ cm}^{-3}]}$. In our work, highly dense plasmas $n_e \approx 10^{20} \text{ cm}^{-3}$ were used, for which charges approximately above 2.4 pC are already significant, while for $n_e \approx 10^{19} \text{ cm}^{-3}$, 8 pC. Further studies in the blow-out regime set a threshold for field-flattening and the maximum charge which could be loaded to keep a constant E is:

$$\left(\frac{Q_{trap}}{\text{nC}} \right) \times \left(\frac{E}{\text{GV/m}} \right) \approx 0.5(k_p R)^4 \quad (3.20)$$

which yields approximately 8 pC for 150 GV/m at $a_0 = 1.5$, assuming matching conditions ($k_p R \approx \sqrt{a_0}$). These values written above are meant to contextualize the reader within the plasma accelerators feasibilities.

3.2 LWFA experimental setup

Once the basic theoretical LWFA foundations were explained, as well the spatio-temporal changes of the laser pulse in an underdense plasma in sub-sec.2.3.1, the reader should be ready to under-

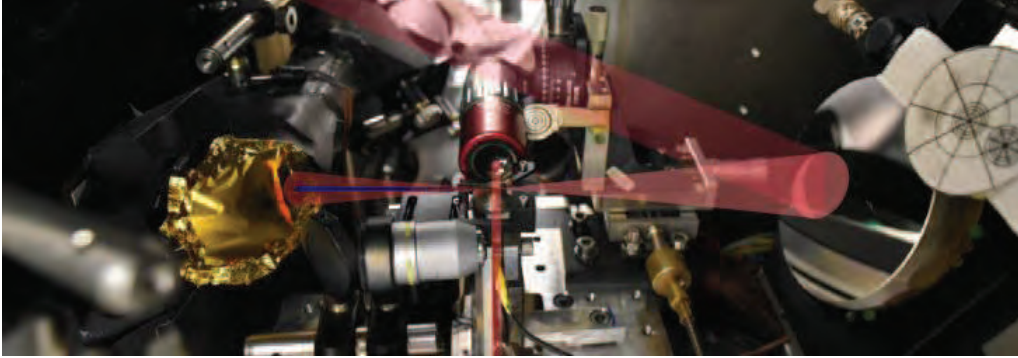


Figure 3.5: Experimental setup for laser wakefield acceleration using the sub-5 fs LWS-20. The laser beam is focused by a $F\#4$ 30° off-axis parabolic mirror in the helium gas emanating from a supersonic de Laval nozzle. 20 cm's after the interaction, the laser is reflected by a $3\ \mu\text{m}$ gold foil while the accelerated electron beam penetrates the foil and propagates further for its characterization. A probe-beam propagates across the nozzle perpendicularly to the driver to image the interaction via shadowgraphy [13]

stand the experimental results presented in this work. But before that, we need to introduce the conditions under which the experiment took place and the methodology we followed to measure the data. Laser parameters, such as intensity or focal spot size, as well as the experimental setup are presented in sec.3.2.1. Conventional diagnosis of the electron parameters (charge, spatial profile, divergence, spectrum) are described and more importantly, we give details on how we tailor the plasma density profile using a razor blade in sub-sec.3.2.2, in order to optimize the injection into the wakefield.

3.2.1 The LWFA chamber

The laser beam is delivered from the sub-5 fs LWS-20 laboratory to the electron acceleration chambers after approximately 20 meters of vacuum beamline. In the LWFA chamber, the laser beam is immediately split into two beams through a holed-mirror. These beams have a ratio of 1:10 in size, therefore we will call the larger beam the *driver beam* and the other one, the *probe beam*. For the first results of this thesis, the driver beam is focused with a $F\#4$ 30° off-axis parabolic mirror, see Fig.(3.5) to a spot size w_0 of about $4.7\ \mu\text{m}$ (see Fig.(3.6)) on a $300\ \mu\text{m}$ de Laval supersonic nozzle, where w_0 is the radius of the beam at $1/e^2$ of its peak intensity. The gas target, as well as the blade holder, the microscope objective for focus observation and long-working-distance objective for side-view imaging, were fixed to a 3D motorized stage with reproducibility down to $10\ \mu\text{m}$, approximately.

The laser focal spot size was day-to-day characterized and optimized with an adaptive mirror. For this purpose, a 10x microscope objective was employed to magnify the laser at its focal plane and image it outside the LWFA chamber. The shot-to-shot peak intensity fluctuations were measured to be normally 5%, even down to 3%. Pointing stability was on the order of $10 - 20\ \mu\text{rad}$. The energy content in the focal spot FWHM was about 28-35%, typical for flat-top

laser systems. The energy on target was normally 50-60% of the laser right after amplification due to losses in the compression bulks and the beamline, i.e. 40 mJ. For the LWFA experiments using this focusing geometry, a peak intensity of $1.2 \times 10^{19} \text{ W cm}^{-2}$ ($a_0 \approx 2.3$) was reached in vacuum.

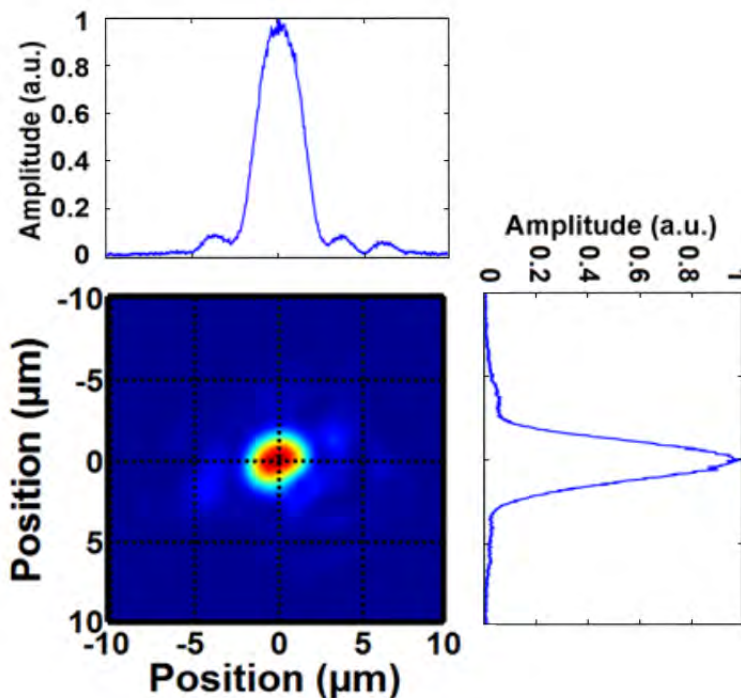


Figure 3.6: Laser spatial profile focused by an F#4 off-axis parabolic mirror to $5.5 \mu\text{m}$ (FWHM).

The gas nozzles were previously characterized in [66, 24]. Electron density characterization was based on interferometry and Rayleigh scattering and cross-checked with plasma wave direct observation and a wavefront measurements from the probe pulse (Phasics). Supersonic nozzles have the advantage of providing flat-top gas density profiles at about a diameter distance, i.e. $200 - 300 \mu\text{m}$, away from the gas exit. Electron densities of about $7 - 21 \times 10^{19} \text{ cm}^{-3}$ were employed to excite the wakefield. After right compression of the laser pulse, electron beams are observed on absolute-calibrated [15] scintillating BIOMAX screens about 20 cm away from the source (Fig.(3.5)). Electron parameters such as spatial profile, divergence, pointing and charge are measured and analyzed on this screen. A $3 \mu\text{m}$ gold foil is inserted just before the BIOMAX to reflect the driver beam in order to reduce laser-induced background in the scintillation signal measurement.

Once the previous electron properties have been measured, the BIOMAX screen is removed and the electron spectrum can be measured using the same technique: the electron beam enters a permanent magnetic dipole through a 1 cm pinhole and is deflected according to its energy. Another BIOMAX foil is placed at one side of the magnet and it is imaged by three cameras. The

third camera observed the electron beams whose energy corresponded to energies above 16 MeV and were not clearly resolved while the first two the energies from 1-16 MeV with high resolution. The magnetic field inside the spectrometer was measured and used for calibration. The electron tracks are depicted in Fig.(3.7). For all measurements, it is assumed that the FWHM spatial extension of the beam (≈ 3 mm) as well as its FWHM divergence (≈ 25 mrad), does not affect the final measurement of the spectrum. The experiments done with the 8 fs LWS-20 by [12] used a similar setup for the beam's spatial and charge characterization, but a larger spectrometer was implemented [135].

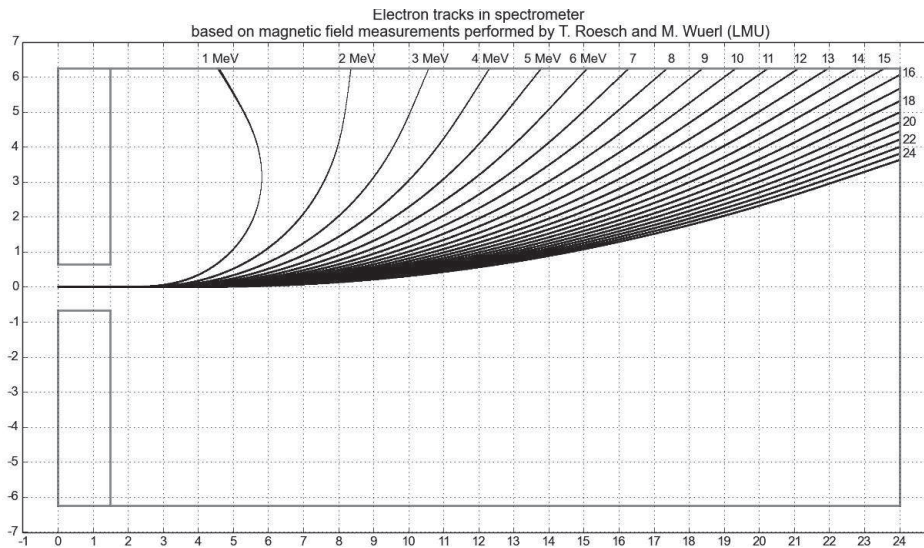


Figure 3.7: Electron dispersion inside the dipole magnet used with the sub-5 fs LWS-20.

The probe beam propagated perpendicularly to the driver across the gas nozzle and it was imaged through a long-working distance 20x long working distance microscope objective to a CCD camera outside the chamber. This special diagnostics allowed us to retrieve the electron density at exactly the laser height, the focal plane of the laser at very low densities, plasma channel formation, the electron injection positions into the wakefield across the plasma via shock-front visualization or by observing a small saturated spot in the image which corresponds to the electron radiation during its initial acceleration. For some experiments, the transmitted laser parameters such as energy and spectrum were measured. The driver beam was coupled out after the interaction by means of a Fused silica wedge and imaged outside the chamber.

3.2.2 Shock-front generation

Following the description in [18], from Euler's equation and from the conservation of mass, the following relationships for a fluid of density ρ , velocity u , pressure p in a steady flow through a

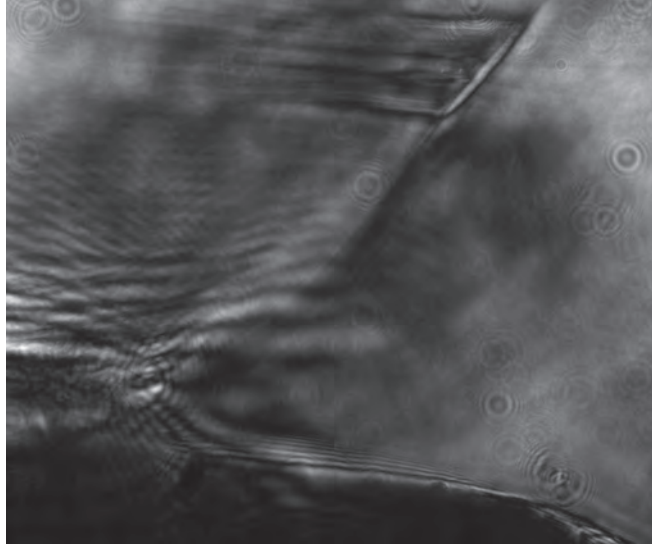


Figure 3.8: Visualization of the shock front on the sideview camera.

cavity of cross-section A , should be fulfilled:

$$u \, du = -\frac{dp}{\rho}$$

$$\frac{d\rho}{\rho} + \frac{du}{u} + \frac{dA}{A} = 0$$

From which the area-velocity relation is deduced as a function of the Mach number, $M = u/v_s$ where $v_s = \sqrt{\left(\frac{\partial p}{\partial \rho}\right)_s}$ is the sound speed:

$$\frac{du}{u} = \frac{dA/A}{M^2 - 1} \quad (3.21)$$

From Eq.(3.21), it is clear that u is increasing with the cross-section A , for $M > 1$.

Furthermore, a sudden density transition can be experimentally realized by placing a razor blade directly at the exit diameter of a supersonic de Laval gas jet. Due to its supersonic nature, the gas flow cannot adapt itself to the razor blade before reaching it and creates a shock front (see Fig.(3.8) of thickness on the μm -scale and two density regions which ratio is determined principally by the projection of the Mach number M , $M \sin(\alpha)$. For most of the results, a Mach number of 5 is assumed and an angle $\alpha \approx 17^\circ$. The density ratio is given by:

$$\frac{n_2}{n_1} = 1 - \frac{2}{\kappa + 1} \left(1 - \frac{1}{(M \sin(\alpha))^2} \right) \quad (3.22)$$

where $\kappa = 5/3$ is the specific heat ratio for mono-atomic gases. For $\alpha_{cr} = \arcsin(1/M) \approx 12^\circ$, the density jump disappears. The density ratio is therefore a function of the Mach number, mainly. As first mentioned in [131], the density jump used in the experiments is about 1.6, as shown in Fig.(3.9). For $M \gg 1$, the density ratio tends to 1/4 for a gas like He. As seen in sub-sec.3.1.4, this limit corresponds exactly to the zero field position. As explained in [130], the

Mach number at the nozzle output with a fixed nozzle length varies as the ratio between the exit hole and inner waist diameter changes. For all experiments, a ratio of 1 : 3 was used and an opening half-angle of 20° .

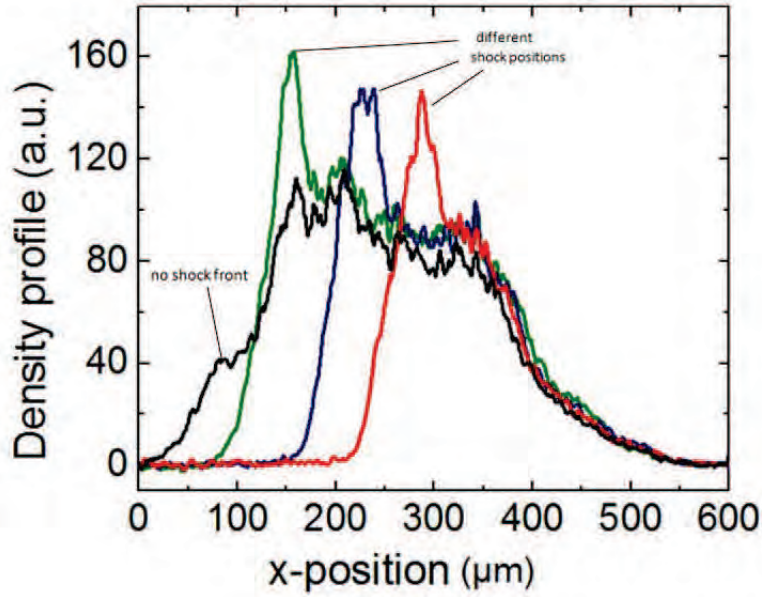


Figure 3.9: Measured density profile of a $300 \mu\text{m}$ nozzle via Rayleigh scattering implementing shock front for different positions, as well as without any razor blade [24]. The position of the razor blade was $270 \mu\text{m}$ above the top of the nozzle.

The width of the shock front increases the farther away the razor blade is. It has been observed in previous experiments [131, 14] that the absolute energy spread ΔE of the electron beams was somewhat larger than what will be shown in this thesis $5 - 10 > 3 \text{ MeV}$. The shock front width is directly connected to ΔE : in these former experiments, the laser position was about $500 \mu\text{m}$ from the razor blade while in the experiments shown in this thesis, the laser propagated only $100 - 200 \mu\text{m}$ away. Furthermore, it was recognized by the authors in [14] that shock front was difficult to implement for multi-mm gas targets without compromising the spectral quality in terms of $\Delta E \leq 5 \text{ MeV}$.

3.3 LWFA experimental results

Finally, the experimental results! They intend to shed light on the electron acceleration mechanism and the evolution of the electron bunch in the phase-space. In particular the fundamental accelerator's energy limitation as described in sub-sec.3.3.1. As explained in the sub-sec.3.1.3 in the LWFA's introduction, the maximum obtainable energy of an ideal and infinite laser-plasma accelerator is limited by dephasing. Due to the strong scaling of the accelerator's parameters, see Eq.(3.10), this slippage takes place within $60\text{-}300 \mu\text{m}$'s when the wakefield is excited by

ultra-short < 10 -fs laser pulses. For the sake of completeness, we decided to include the results obtained with the 8 fs LWS-20 as well. This work consists of the first systematic measurement of this effect. In order to study in detail new phenomena occurring during acceleration, the spectral quality of the beam and its volume in the phase space matters. For this purpose, shock front is the ideal injection mechanism. Its implementation with larger gas targets (multi-mm's) must, nevertheless, be further developed: placing the razor blade above the whole nozzle causes instabilities and fluctuations on the injection position and the shock-front width. Yet, for the $300 - 500 \mu\text{m}$ nozzles required for < 10 fs short lasers as the ones delivered by the LWS-20, the latter issue is not problematic. Our results are described by a simple 1D model (3.3.1), discussed in (3.3.1) and supported by experimental proofs and PIC simulations (3.3.1).

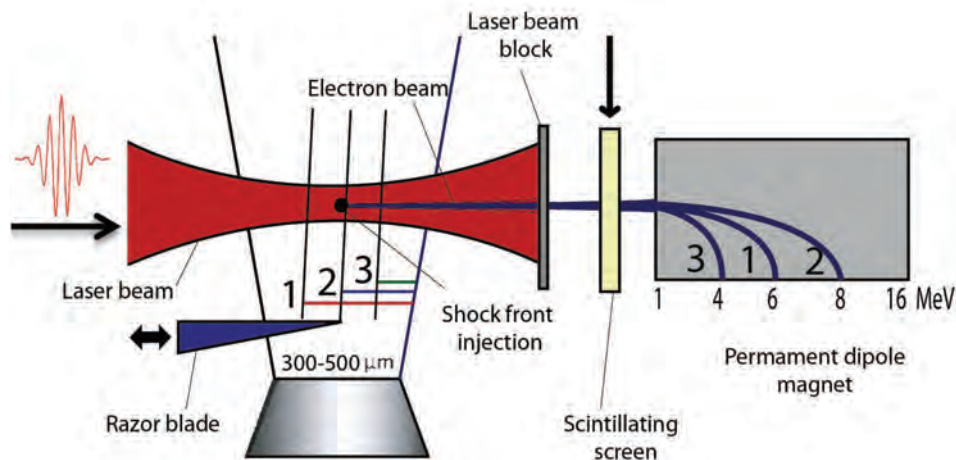
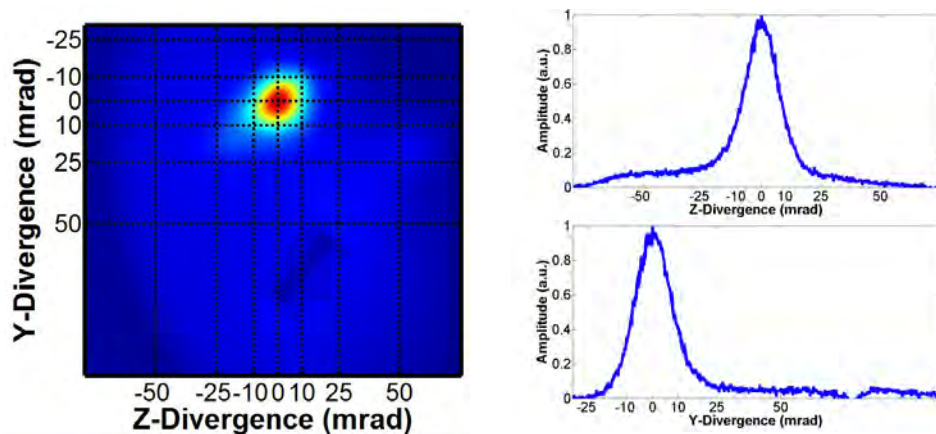


Figure 3.10: Illustration of the experimental setup when scanning the injection position along the laser propagation direction. Different injection positions are displayed $x_1 < x_2 < x_3$, corresponding to different acceleration lengths $L_1 > L_2 > L_3$.

3.3.1 The dephasing effect

Measurements

Once the laser is compressed, focus diagnosis has been checked, the razor blade set $100 \mu\text{m}$ above the jet exit, gas jet position scanned with $10 \mu\text{m}$ resolution and backing pressure tuned to release gas at $n_e \approx 10^{20} \text{cm}^{-3}$, as illustrated in Fig(3.10). Firstly, suboptimal acceleration was observed. Highly fluctuating electrons beams with rather low charge are observed. By chirping the beam about $+10$ - 20fs^2 the performance of the accelerator improves considerably. As mentioned in the introduction, the group velocity dispersion in plasma at these high densities is on the order of $-7 \text{fs}^2/100 \mu\text{m}$. In all experiments, the alignment and tuning of the experimental parameters was done by only looking at the electron beam profile, not its energy. The accelerator, at its best performance, delivers 25-35 mrad (FWHM) divergence with down to 8 mrad pointing fluctuation (record value) beams with few-pC (See Fig.(3.11a)).



(a) Typical electron beam

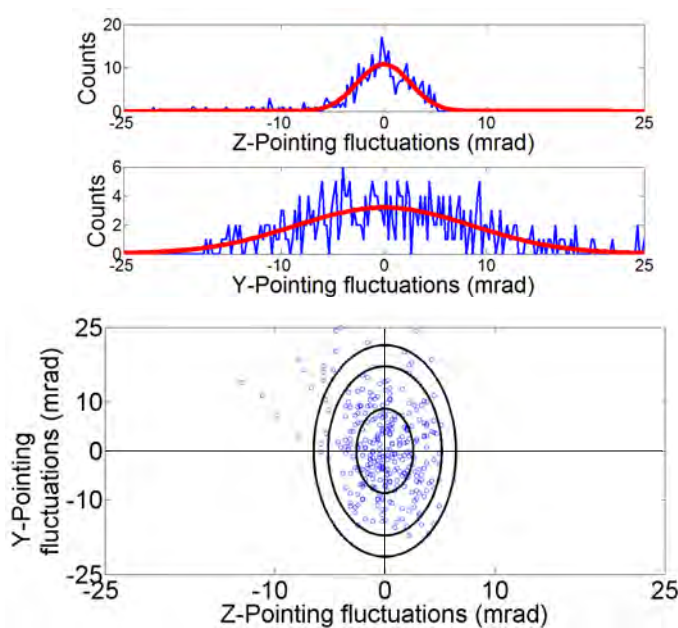
(b) Pointing fluctuations. Circles have radius of $R = \text{std}, 2\text{std}, 2.5\text{std}$

Figure 3.11: Typical spatial properties of the electron beam

In order to study the dephasing effect, the acceleration length was scanned at different densities: $4 - 21 \times 10^{19} \text{ cm}^{-3}$. The acceleration length had been normally scanned by changing the size of the gas target [29, 51]. In this work, we injected an electron bunch at different positions of the accelerator by scanning the razor blade along the gas nozzle. Although it is difficult to absolutely determine the acceleration length at which the electron bunch reached the maximum energy, the relative position between the injection points are determined with sub- $10\mu\text{m}$ resolution. Therefore, and up to some constant, both methods are equivalent. We then observed how the main electron parameters such as charge, divergence and energy spectrum varied along the

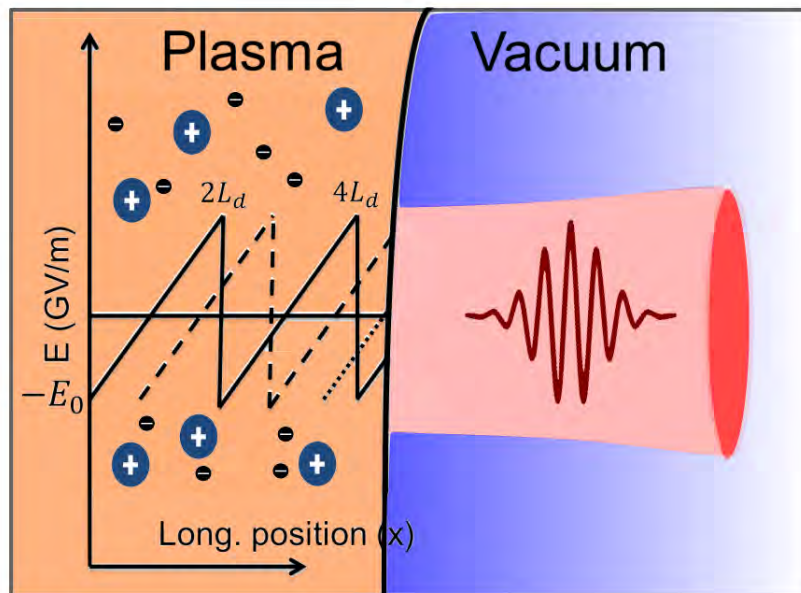


Figure 3.12: Analogy of the wakefield in the laboratory frame. Different line styles of the electric field correspond to different acceleration lengths, i.e. injection positions.

acceleration length.

A simple model

The laser-excited wakefield which travels at the laser’s group velocity can be thought of as a steady accelerator in the laboratory frame of the same size of the gas jet, with an alternating field and a periodicity of $2L_d$ as depicted in Fig.(3.12). In order to make valid the previous approximation, it is required that the maximum accelerating field E_0 remains constant along the whole accelerator. In this way, the inserted electron bunch will be accelerated with the same way at all injection positions. In the case of wakefield depletion or extinction by either loss of laser energy or diffraction, the field vanishes along the increasing longitudinal coordinate. These two limitation factors will be discussed later. Such a simple model assumes several approximations:

1. The whole wakefield generation takes place in a flat-top electron density profile, where effects from plasma gradients at the edges are insignificant.
2. In a 1D-like weakly nonlinear plasma wave[41], where nonlinearities are not significant and relativistic effects are not taken into account. Such a scenario fits well to shock-front injection[131, 14]. In a strongly nonlinear scenario such as blow-out [92, 121], higher deviations are expected. This is because the phase velocity of the wakefield is more complex [33, 133] and the dephasing effect is much more dependent on the highly-dynamic “in situ” laser parameters. In the case which we address, the longitudinal electric field in the first plasma period scales roughly linearly with the position in the co-moving frame.
3. The accelerating field also scales linearly within the laboratory frame during dephasing.

4. Any dynamical changes of the first plasma period, referred as bubble, or variations in the group velocity of the laser are not included. Thus, it does not cover the whole physical picture [92, 33, 34, 133, 57] and rather assumes a constant accelerating field.
5. Beamloading does not play a significant role.
6. Electron beam interactions with the laser are not significant. Most LWFA experiments in the last decade have taken place under the condition $c\tau_L \leq \lambda_p/2$. These are either the input values or after self-compression in plasma [46]. Condition 6 is fulfilled therefore at least until the dephasing point even for strongly nonlinear cases.

The accelerating field can thus be written, until the first dephasing period, as a function of position in the laboratory frame x :

$$E(x) = E_0 - \frac{E_0}{L_d}x; \quad 0 \leq x \leq 2L_d. \quad (3.23)$$

Based on our model, the minimum energy for the electron to get trapped corresponds to $E_b = m_e c^2(\gamma_p - 1)$, where $\gamma_p = \lambda_p/\lambda_0$. So analytically, integrating the field $E(x)$ from Eq.(3.23) from $x = 0$ up to a certain acceleration length L_a provides the output electron energy E_p .

$$E_p(L_a) = e \int_0^{L_a} E(x) dx + E_b = eL_a E_0 (1 - L_a/2L_d) + E_b \quad (3.24)$$

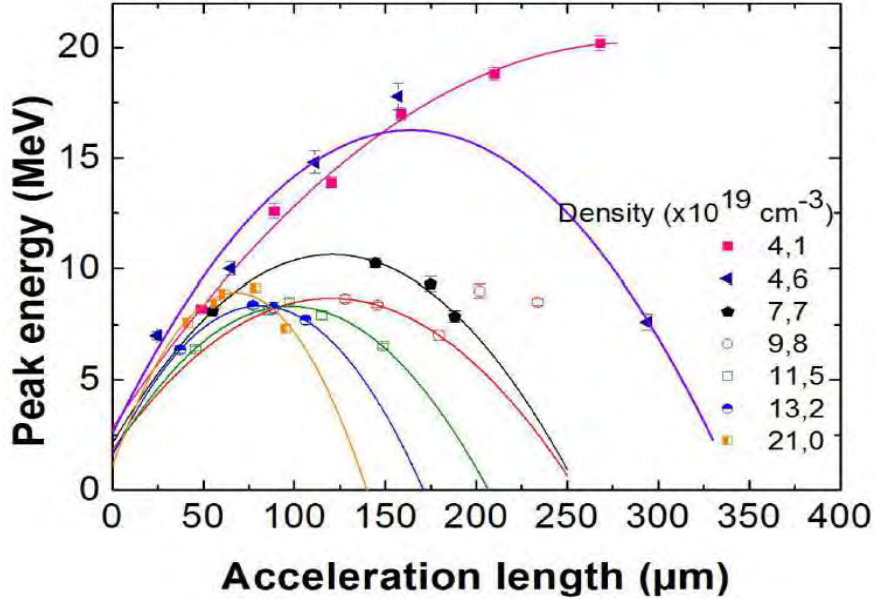


Figure 3.13: Peak energy of the electron spectrum for sub-10-fs laser pulses vs. acceleration lengths for various electron densities. The error-bars indicate standard error over 50 shots. The lines are fits using Eq.(3.24).

Discussion

The peak energy of the electron scales quadratically with the acceleration length Eq.(3.24). For lower densities, $eE_0Ld \gg E_b$. However, in our highly dense plasmas, this last term is not negligible ($E_b \approx 1 - 3 \text{ MeV}$). Fig.(3.13) shows different sets of peak energies as functions of the acceleration lengths for different densities. As mentioned before, the absolute lengths are difficult to measure. Yet, the acceleration lengths plotted in Fig.(3.13) were calculated in the following way:

1. Plot the peak energy with respect to the injection position, measured directly from the plasma channel observation. Larger injection positions would correspond to shorter acceleration lengths.
2. Fit a parabola via least-squares method and mirror (invert) it with respect to the center of the parabola. This corresponds to the $L_a = \text{const.}$ -injection position relationship.
3. Shift the parabola along the x-axis until the y-intersection matches E_b . The acceleration length plotted in Fig.(3.13) is then the distance between the y-axis and the inverted and shifted injection positions. The plasma gradient is not relevant for the retrieval of the final results since E_b is calculated directly from the electron density measurements. The fit remains thus only with two degrees of freedom left.

After fitting then our experimental results with Eq.(3.24), the maximum accelerating field E_0 as well as the dephasing length L_d are obtainable. The dephasing lengths calculated from the fits match well the 1D weakly nonlinear formula Eq.(3.10). Our results match also very well the theoretical predictions by Lu in [92] in the 3D nonlinear regime given by Eq.(3.14), see Fig.(3.14), although this is not our range of operations. This is not surprising since these both formulas yield similar results in a weakly-relativistic regime where $a_0 \approx 0.8 - 1.5$. Relativistic corrections to plasma wave phase velocity, discussed in section 3.1.3, which determines the trapping energy E_b , would lead to a 5% difference in the retrieved dephasing length. The physics captured by Lu's work is based on two main phenomena: strong self-focusing and etching of the laser front (See section 2.3.1). The first is quantitatively characterized by P/P_{cr} , while the second one by the red-shift of the laser spectrum. P/P_{cr} values used by other groups in the blow-out regime: $P/P_{cr} \geq 5$ [51, 99, 45, 29]. Shock-front injection, on the other hand, is realized in such a way that nonlinearities are not so significant ($P/P_{cr} \approx 2$) [14], or as in this work, ($P/P_{cr} \approx 3$) for both laser systems. Furthermore, $P/P_{cr} = 2.7$ is considered to be marginally around the breaking-threshold [121]. Lastly, red-shift of the spectrum was not observed.

Additional results [29, 118] are plotted as well to validate our model for other densities and laser parameters, as long as nonlinearities or relativistic effects do not play a significant role [29]. Longitudinal self-injection proves to work under similar conditions as the ones required by our model. Our results also support the energy scaling $\propto \lambda_p^2$ from Eq.(3.13), since $\frac{20 \text{ MeV}}{8 \text{ MeV}} \approx \frac{5 \mu\text{m}}{3 \mu\text{m}}$.

In order to claim that dephasing was the limiting factor in the acceleration process, laser depletion or diffraction must be insignificant. Complementary measurements (See Fig.(3.15) and Fig.(3.16)) were done in this direction, in particular:

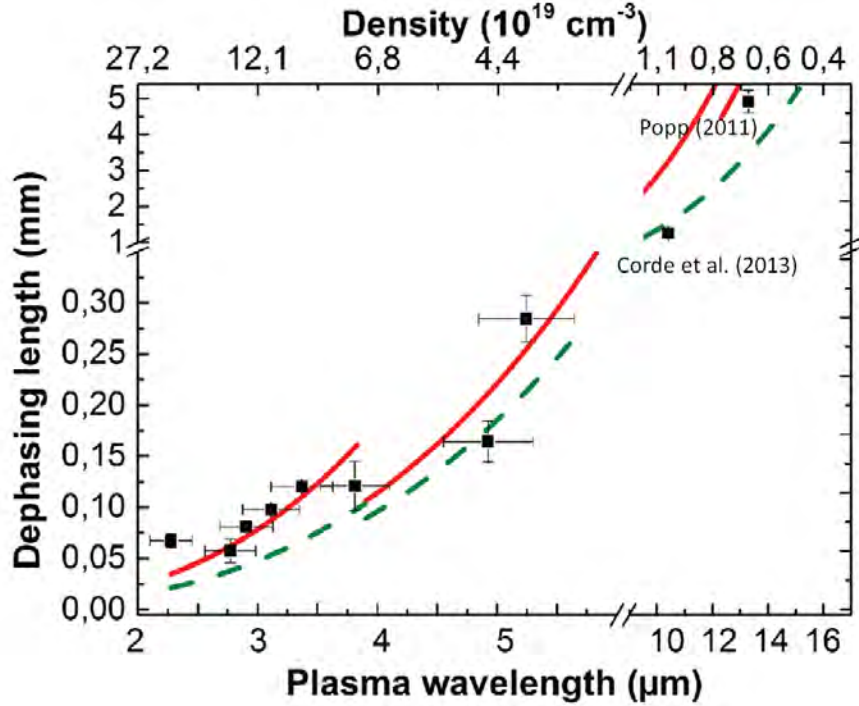


Figure 3.14: Measured (black squares) and predicted dephasing lengths according to $L_{d,3D}$ (red continuous line from Eq.(3.14) using $a_{0,5\text{fs}+\text{CHIRP}} = 1.5$ and $a_{0,8\text{fs}} = 0.8$; and L_d (gray dashed-line from Eq.(3.10)). The results at $\lambda_p = 11$ and $13 \mu\text{m}$ corresponded to an $a_0 = 2.5$ and 2.9 , respectively.

- Laser energy depletion and spectral transmission:** The laser energy was measured after the interaction and only 10-20% depletion was observed. For this purpose, a fused silica wedge was implemented after the nozzle and sent the laser beam outside the chamber and imaged by a lens to the energymeter. The scattered light from the energymeter was used then to measure the spectrum. Moreover, the transmitted spectrum after the interaction showed some depletion beyond 850 nm and the generation of new frequencies from 500-580 nm with an amplitude of about 10% with respect to the laser components around 580 nm (see Fig.(3.15)). Although its origin may not be directly related to a nonlinear process produced by the density perturbations within the wakefield but to ionization. The new frequencies have a relative small amplitude and therefore imply that the process itself was not as non-linear as certain injection mechanisms, such as transverse self-injection [29, 46]. This measurement is a good experimental proof to support our model and claim that we did not enter the strongly blow-out regime.
- Laser diffraction:** The laser diffraction was measured in vacuum through routine focal spot diagnosis. The Rayleigh length is calculated by fitting the evolution of the laser focal spot FWHM size along the longitudinal direction as shown in Fig.(3.16). From the fit, $Z_R = 101 \pm 7 \mu\text{m}$. Although the dynamics of the focal spot during the interaction were

not measured, the plasma channel observation showed an interaction longer than $b = 2Z_R$, the confocal length. Since the focal spot size is comparable to the plasma wavelength, self-focusing will not change the laser evolution significantly [148]. The matched FWHM spot size for $1 \times 10^{20} \text{ cm}^{-3}$ is about $3.3 \mu\text{m}$, comparable to the measured focal spot size. Furthermore, the confocal length is longer than approximately all the acceleration lengths depicted in Fig.(3.13).

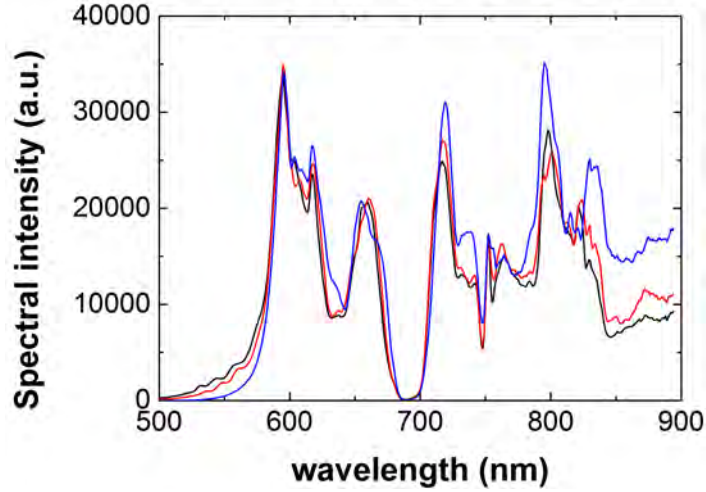


Figure 3.15: Transmitted spectrum after the interaction for 15 bars backing pressure (black), 20 bars backing pressure (red) and no gas (blue).

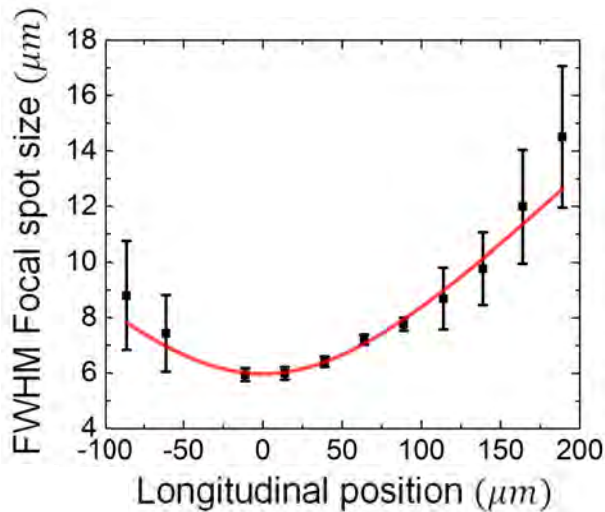


Figure 3.16: FWHM focal spot size scan in vacuum using a $F\#4$ off-axis parabola. The continuous line corresponds to a $w(x) = w_0 \sqrt{1 + (x - x_0)^2 / Z_R^2}$ fit.

- **Re-acceleration after dephasing:** One of the most important results of this chapter is the re-acceleration of the electron beam, back to its previous maximum energy, once it

has dephased and slowed down. It has been observed in many times (See Fig.(3.13) at $n_e = 9.8 \times 10^{20} \text{ cm}^{-3}$ and Fig.(3.18f)). This proof demonstrates that the wakefield is not extinct after the electron has been accelerated significantly longer than L_d . This result is considered to be extraordinarily relevant and will be discussed in more details later, although it has not been possible to reproduce it in PIC simulations.

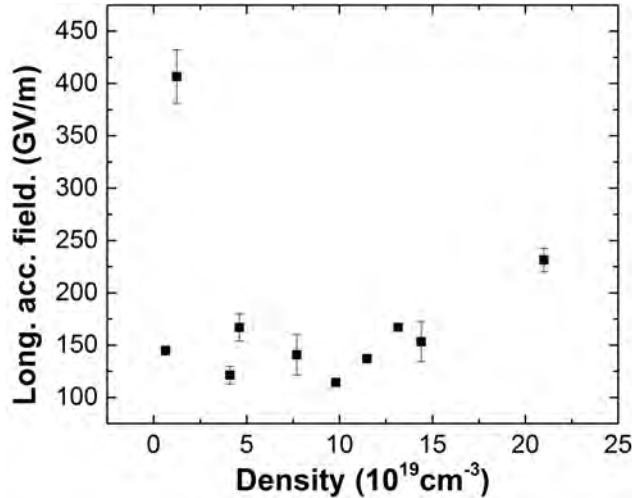


Figure 3.17: Measured longitudinal accelerating field for different densities. The two data points at the lowest densities correspond to the [29, 118].

The retrieved accelerating fields from the fits range from 100-250 GV/m. These fields are about 4 orders of magnitude higher than what conventional accelerators work today with. Yet, they are about 4 times smaller than the cold non-relativistic wave-breaking field from Eq.(3.5). This fact can be attributed to the poor charge separation provided the relative low intensities and the high densities with which the experiment took place. Full electron blow-out occurs for intensities in the order $a_0 > 4$, according to simulations [74]. In our case, due to poor charge separation, the density perturbations are relatively small. Since the applied intensity is similar in all cases, no clear correlation between the measured field and the density can be observed (See. Fig.(3.17)). Furthermore, LWFA driven by few-mJ (less photons) lasers is still being under research, which may differ in reality from the usually reported Joule-level cases.

As mentioned before, the electron energy is the main observable of the dephasing effect. Nevertheless, the small space the electron bunch occupies in the phase space allows the complete characterization of the dephasing process with other important observables such as divergence, charge or energy spread. The sensitivity of electron parameters such as the absolute energy spread depends of course on the injection mechanism. For the results using the 8-fs version of the laser, the shock front was used in a sub-optimal way. Due to laser instabilities and the fact that the injection took place several hundreds of micrometers away from the razor blade, the energy spread of the bunches was larger and the peak energy stability was also affected. Yet, general observations are supported by the old results in [130, 12] and more strongly by the new ones presented in this thesis.

For most of the experiments regarding dephasing, electron parameters were measured for 5 different injection positions. Nevertheless, a highly detailed measurement was realized and it is shown below. We can learn more about the re-acceleration by taking a closer look at the electron spectra.

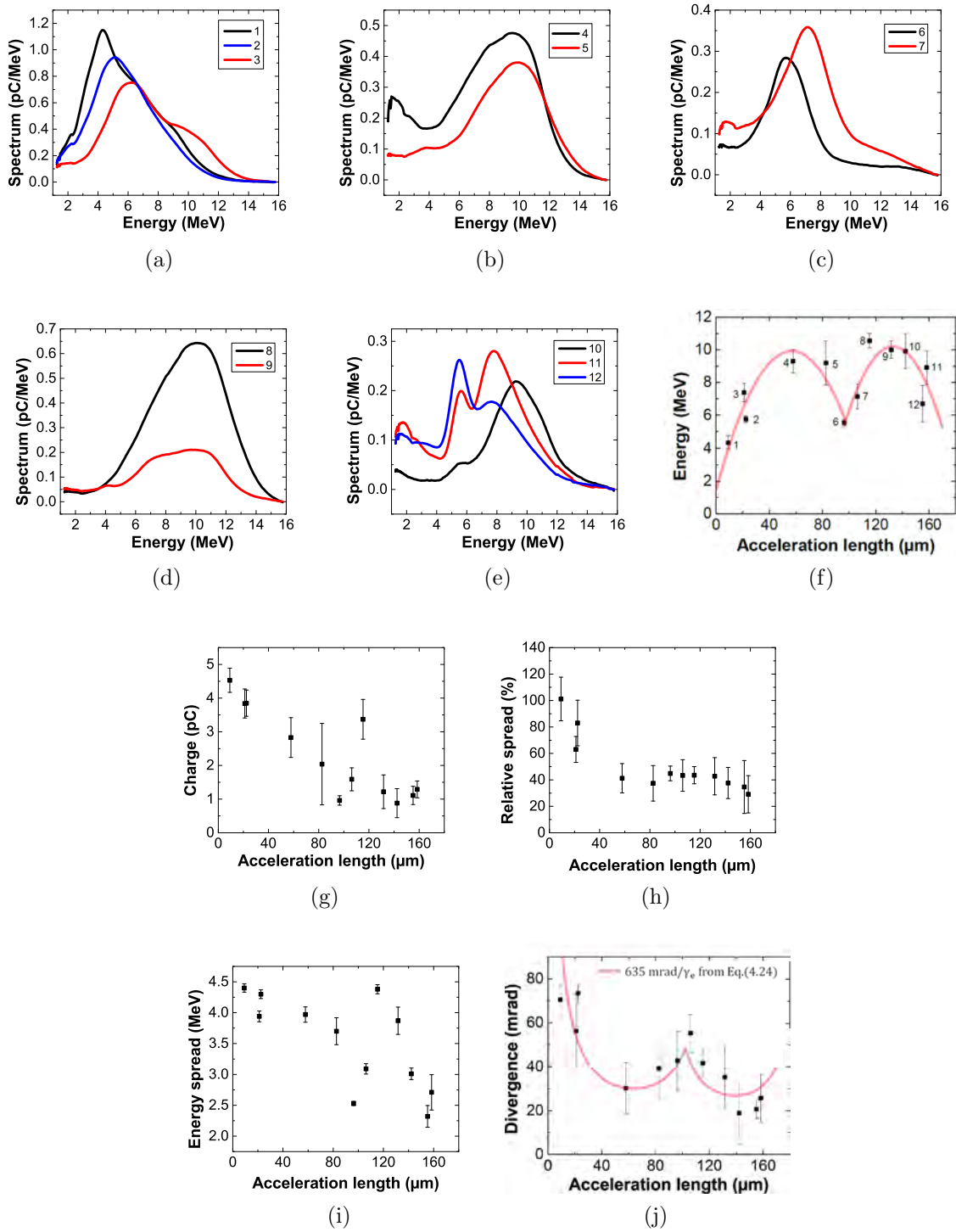


Figure 3.18: Insight into the dephasing process. (a-e) correspond to electron spectra, (f) the peak energy, (g) charge, (h) relative energy spread, (i) absolute energy spread and (j) the FWHM divergence as a function of the acceleration length.

In Fig.(3.18a-e), we plot a sequence of spectra corresponding to different acceleration lengths as depicted in Fig.(3.18f). In this sort of movie, many features are observed:

1. For long enough acceleration lengths $L_a > L_d$, the peak energy of the dephased electron beam increased again, as seen in Fig.(3.18f). Although this effect was not seen in PIC simulations, we believe to be originated from the phase-space rotation of the beam. Shock-front injected electrons occupy a small volume within the plasma period and such phenomena become observable. After reaching the first dephasing point, the electrons enter the decelerating phase and become slower than the plasma wave itself, falling back with respect to the laser. Those particles with enough momentum, ($E_b > 1.4 \text{ MeV}$ at the end of the plasma period) will get re-trapped in the acceleration region. In Fig.(3.18b) a new bunch at low energies is generated (spectrum 4) and further accelerated (spectrum 6-7) in Fig.(3.18c). The whole process is described in Fig.(3.19).
2. The absolute energy spread seemed to remain constant up to the first dephasing point, which is characteristic to the shock-front technique. See also [14].
3. The relative energy spread improved by almost a factor of 3, proportional to the energy gain. After the first dephasing point, $\Delta E/E$ remained approximately constant.
4. There is a continuous loss of charge, $0.3 \text{ pC}/10 \mu\text{m}$, during this first part of the acceleration up to $L_a \approx 100 \mu\text{m}$ and later remained approximately constant.
5. We plot also the divergence of the beam as a function of the acceleration length. Due to conservation of the normalized transverse emittance, the beam divergence scaled as $1/\gamma_e$, where $1/\gamma_e$ is the gamma factor of the electron bunch. The fit in Fig.(3.18j) corresponds to the gamma factor obtained from Eq.(3.24) with the fitted values. From these observations, we also expect the charge loss to occur in a homogeneous fashion throughout the beam and therefore, not affecting the divergence significantly.

The results above show a significant improvement of the general electron beam parameters as the dephasing effect manifests. Moreover, these results show also that our model describes well the relevant process even beyond the dephasing length.

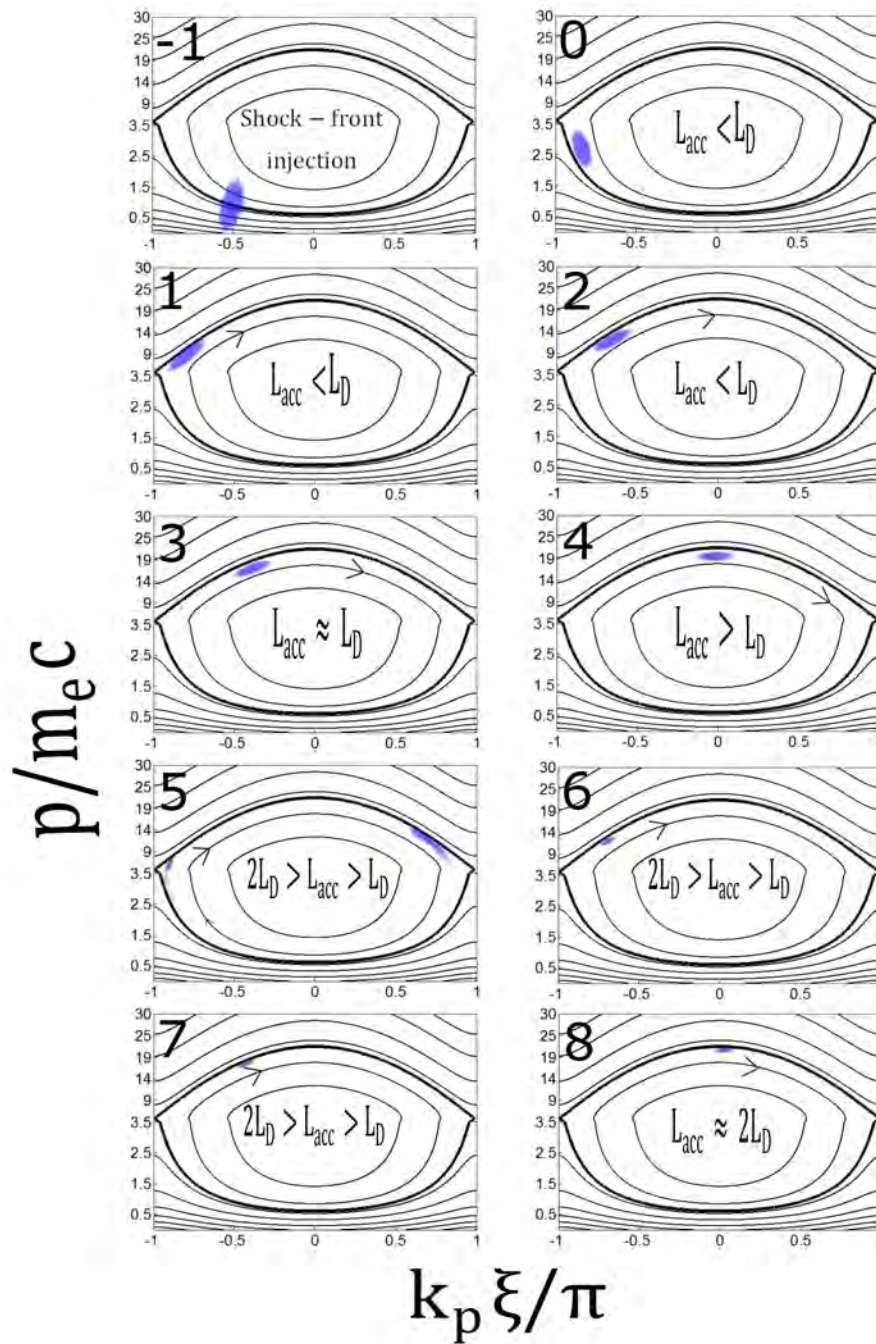


Figure 3.19: Scheme of the electron bunch evolution in the phase space for different acceleration lengths (1-8).

PIC simulations

Jiancai Xu performed 3D PIC simulations using the code VORPAL [107] to investigate details of the dephasing process, the injection technique and help us to support our experimental results. The simulation box was $20 \times 30 \times 30 \mu\text{m}^3$ and moved with the laser pulse. It was divided into $400 \times 300 \times 300$ cells, each one containing one macro particle inside.

Fig.(3.20) sheds light on the details of the trapping mechanism by showing a simulation where the wakefield propagates through a plasma at $4 \times 10^{19} \text{cm}^{-3}$. The laser employed has 8 fs duration and $a_0 = 0.75$. In the first row, the wakefield in the x-y plane is shown. In the second row, the longitudinal electric field. Underneath them, we plot the ratio between the relative position of the electron bunch with respect to the middle of the bubble (where the longitudinal electric field is zero) and the relative position of the middle of the bubble with respect to the end of the bubble, $Q = (x_{mid} - x_{elec}) / (x_{mid} - x_{end})$. The injection position is located at 0 μm . For self-injection, this ratio becomes 1, since injection occurs at the very rear of the bubble. Using shock front, the injection position is “somewhere” in the accelerating phase (depending on the density jump in the transition). For a density jump of 1.6, like in the case above, $Q \approx 0.6$ initially. Once injected, most of the thermal electrons in the bunch are outrun by the laser in the first μm 's of propagation until some of the electrons gain enough momentum to be trapped, at $Q > 0.7$ and begin to be accelerated. Because of this, we claim that shock-front injection will not practically shorten the final dephasing length. Moreover, it has been already observed in previous experiments [24, 131] that the maximum obtainable electron energies in both cases are similar.

In Fig.(3.21b), we obtain insight into the dephasing effect. In this case, the plasma field has reduced its amplitude considerably around 200 μm (see long-dashed line). Its decelerating field is not as strong as expected and the final electron energy stays constant. The dephasing point turns out to be around 120 μm (short-dashed line). The relative energy spread reduces by a factor of 6 up to the dephasing point and then it remained approximately constant, as observed in Fig.(3.21a). The absolute energy spread reduced by 25% up to the dephasing point and then increased again. This contraction and expansion of the absolute energy spread seems to come from the flip of sign of the longitudinal field. In the spectra shown in Fig.(3.21c), and more in detail in Fig.(3.22), only a significant decrease in the amplitude is observed, rather than the width. The absolute energy spread increases at the very end of the simulation, due to depletion and reduction of the accelerating field. In the experiments using 8 fs laser pulses, the absolute energy spread reduction is not so obvious due to technical reasons, for instance, the width of the shock front. Yet, the charge depletion during the dephasing process was recognized. The simulations corresponding to the 8 fs case confirm that the electric field is strong at least for 200 μm , allowing us to claim that dephasing was the limiting factor in terms of energy.

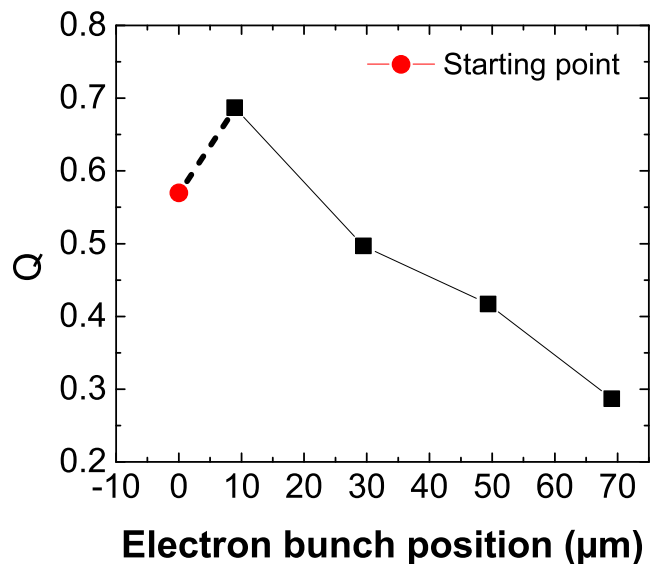
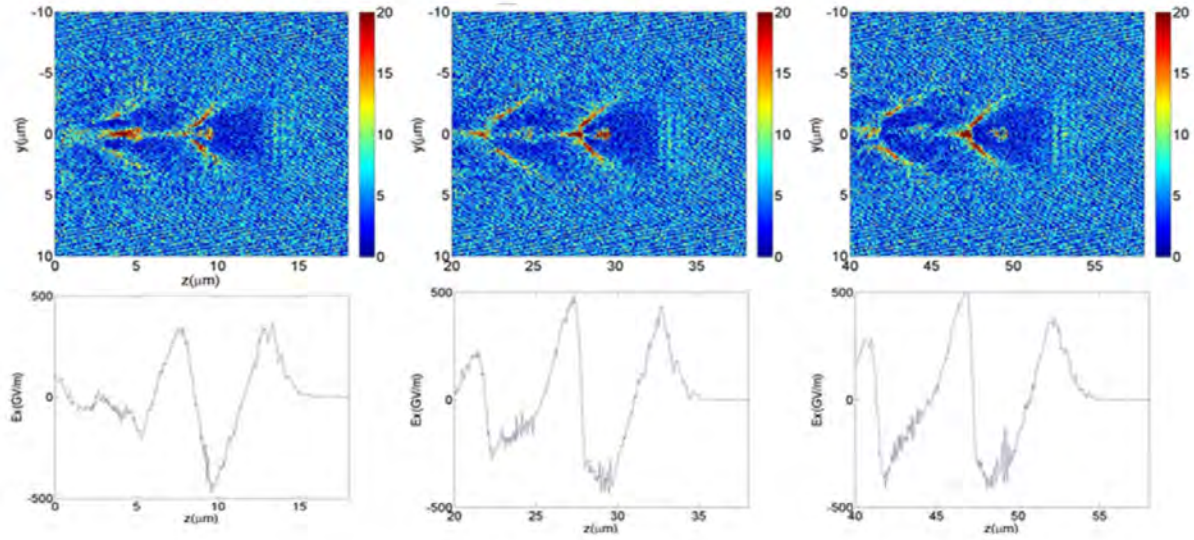


Figure 3.20: Parameter Q as a function of the electron bunch position in the co-moving frame.

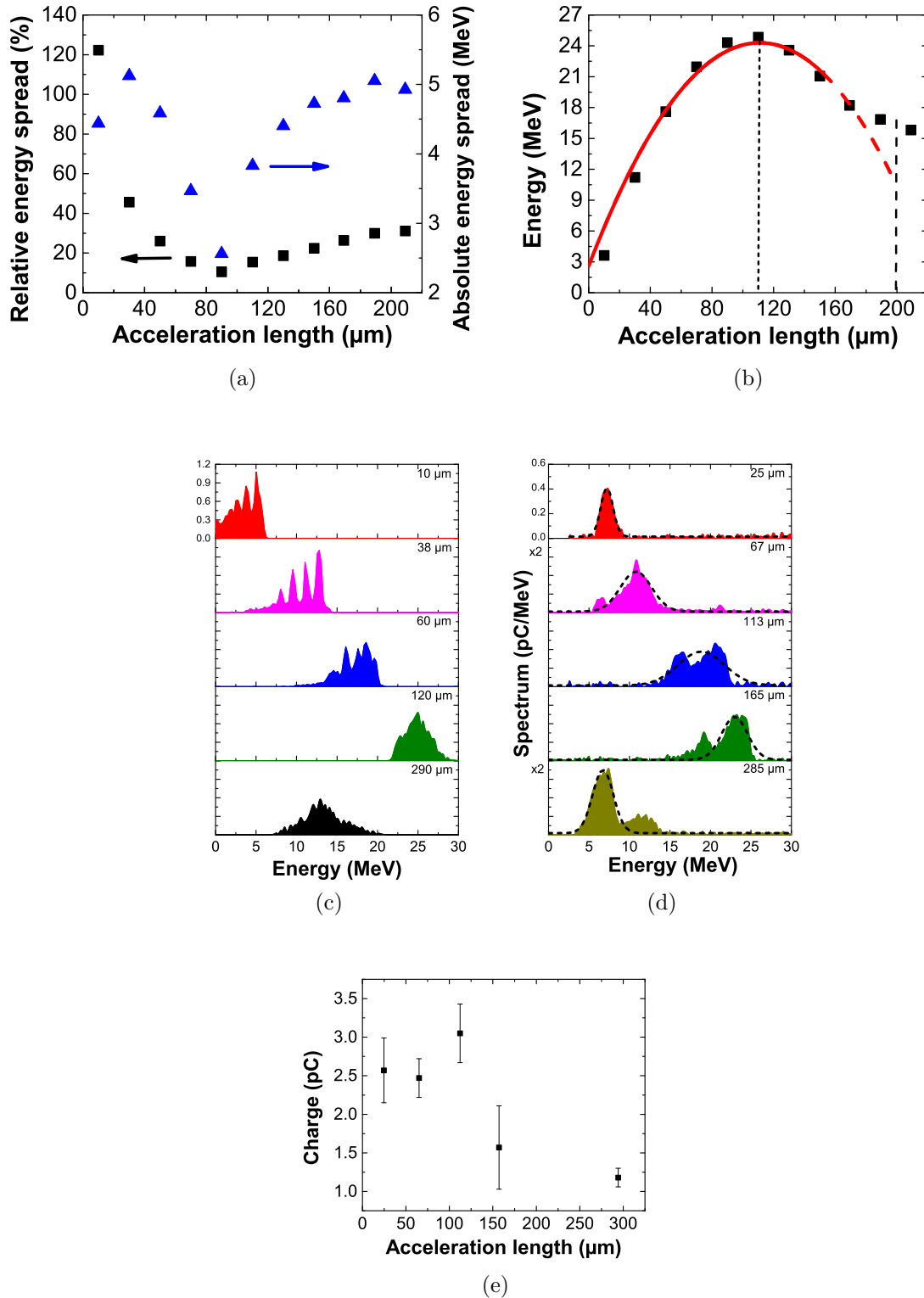


Figure 3.21: (a),(b) and (c) Simulation results of a wakefield excited by an 8-fs laser pulse with a normalized electric field of $a_0 = 0.75$ at a density of $4 \times 10^{19} \text{cm}^{-3}$ (d) Typical experimental shots for different acceleration lengths, labeled on the top-right corner; (e) Measured averaged charge as a function of the acceleration length.

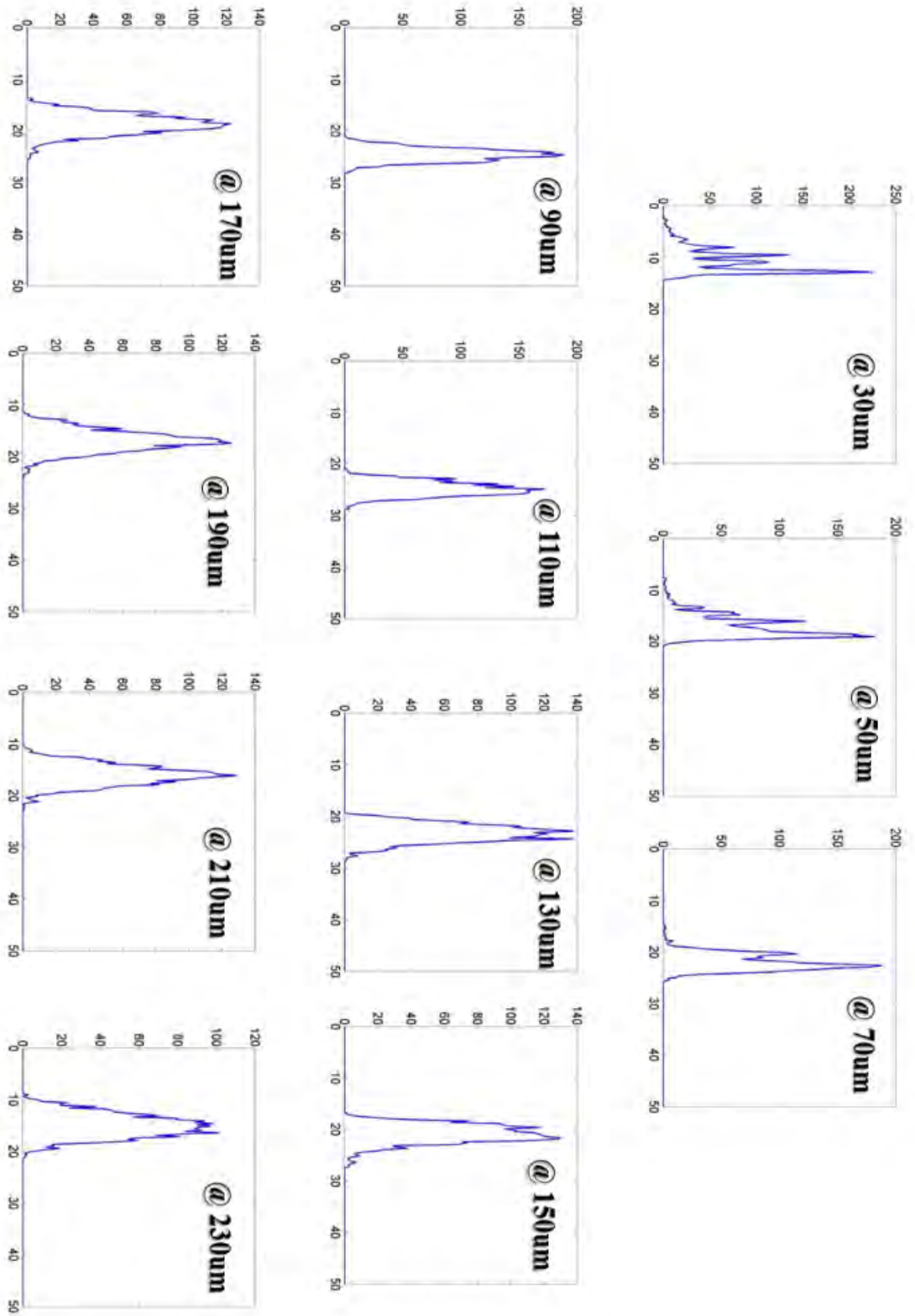


Figure 3.22: Simulated electron spectra with an 8 fs laser pulse with $a_0 = 0.75$ at a density of $4 \times 10^{19} \text{ cm}^{-3}$.

In the 5 fs simulations, we confirmed our hypothesis that the wakefield was optimal after chirping the laser pulse. The wakefield excited by a fully compressed laser pulse was extinct after 40 μm . After chirping, simulations showed (i) that the accelerating field was still strong up to 110 μm , which is the longest dephasing length measured for this laser; and (ii) the wakefield was approximately constant along the acceleration length, in particular up to 70 μm . The latest points, however, already show the extinction of the plasma wave (See also Fig.(3.25)). During the previous experimental campaign with the 8-fs version, this effect was negligible. Fig.(2.6) shows us both: the dispersion as well as the pulse duration at which, in a matched plasma $\lambda_p = c\tau_L/2$, dispersion will become significant.

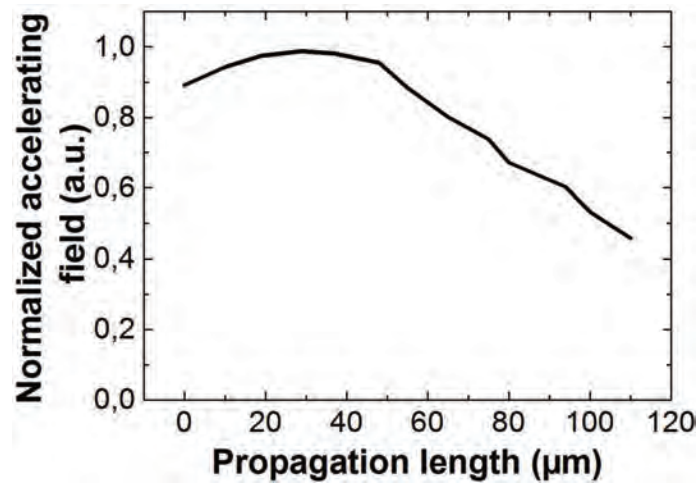


Figure 3.23: Simulated longitudinal electric field for 5 fs+20 fs² laser pulse with $a_0 = 1$ at a density of $1 \times 10^{20} \text{ cm}^{-3}$. Laser focal plane, as well as the shock front position, is $x = 0$.

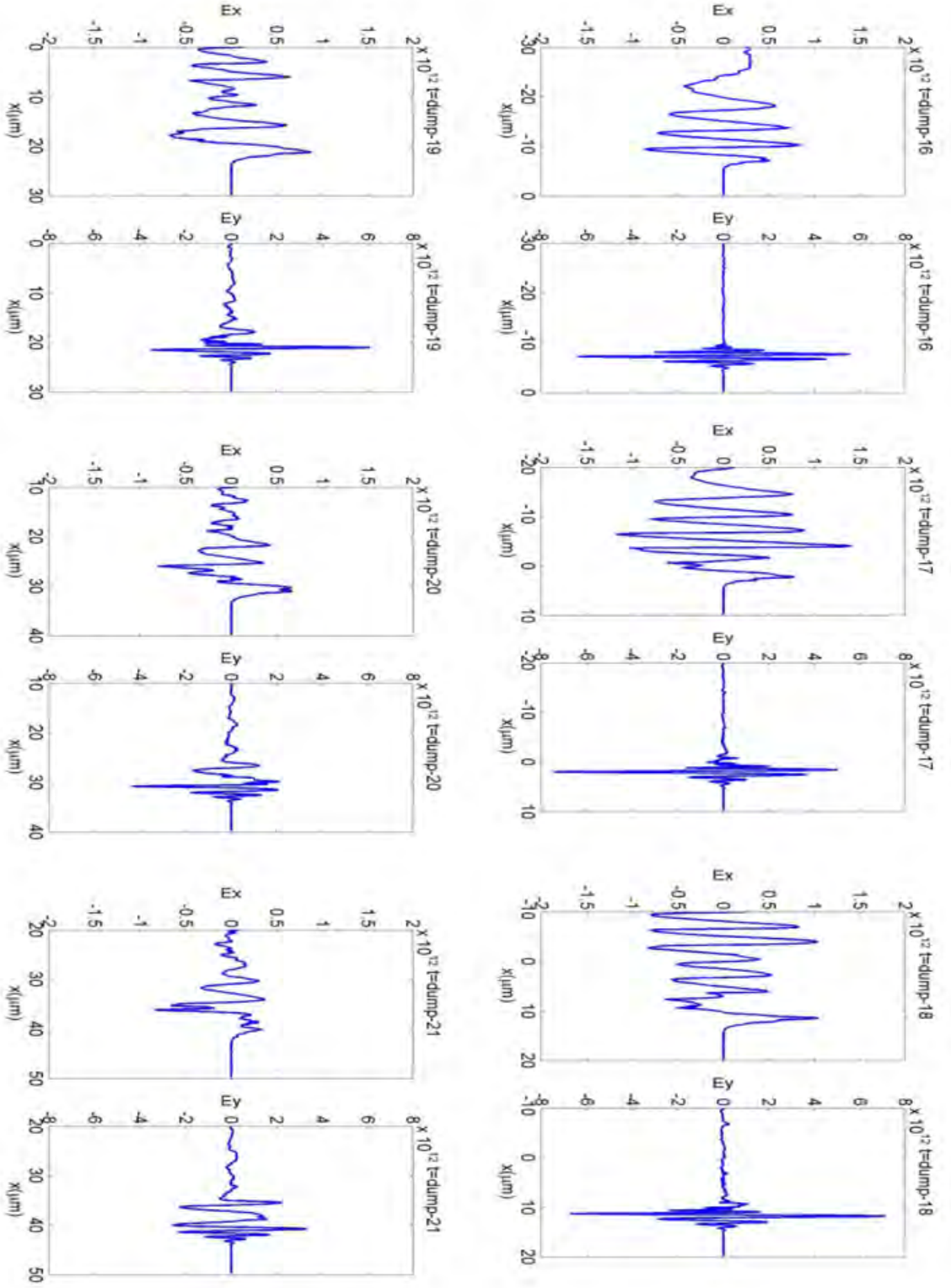


Figure 3.24: Simulated laser and wakefield evolution with an 5 fs laser pulse with $a_0 = 1$ at a density of $1 \times 10^{20} \text{ cm}^{-3}$. Laser focal plane, as well as the shock front position, is $x = 0$.

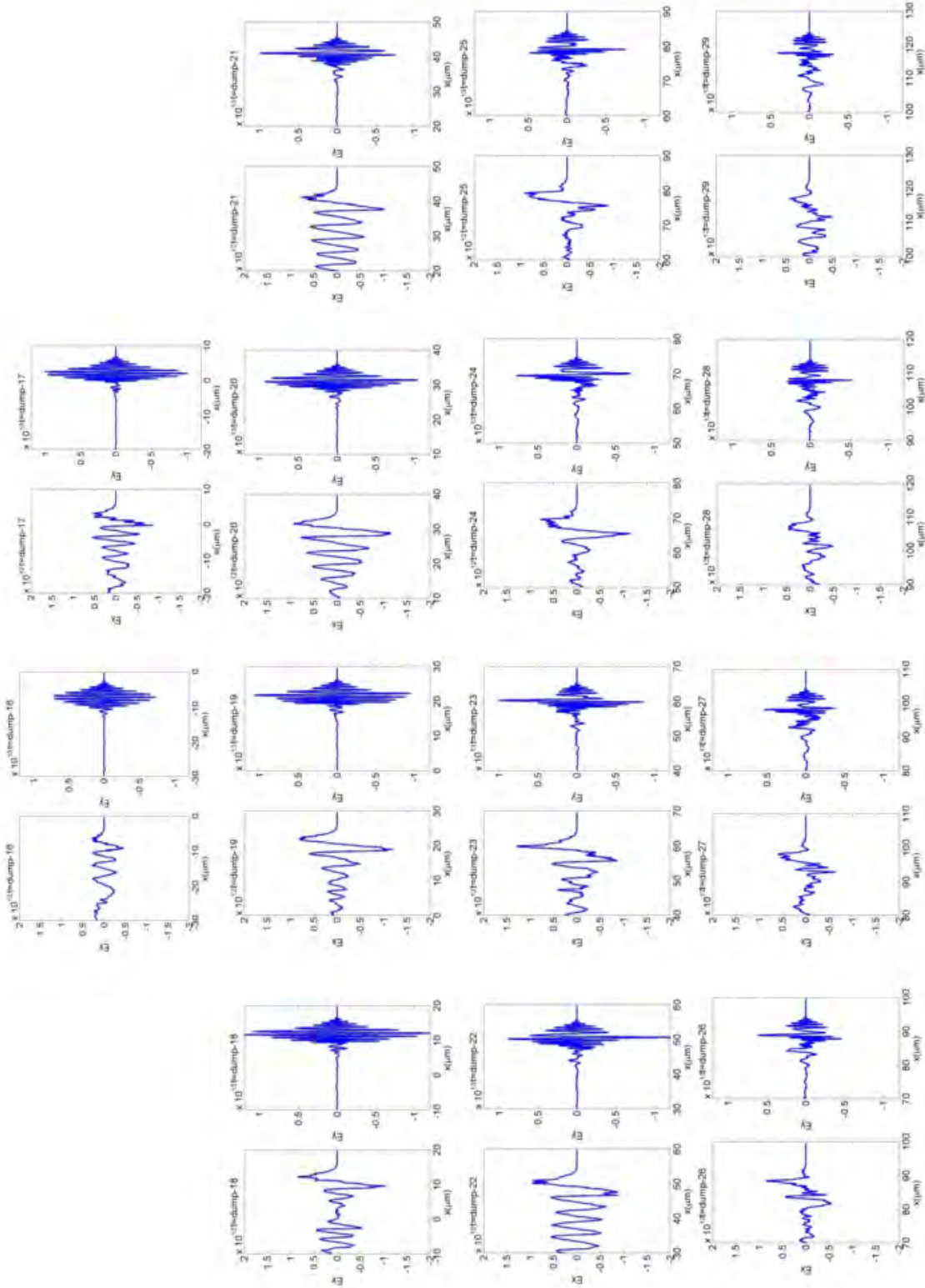


Figure 3.25: Simulated laser and wakefield evolution with $5\text{ fs}+20\text{ fs}^2$ laser pulse with $a_0 = 1$ at a density of $1 \times 10^{20}\text{ cm}^{-3}$. Laser focal plane, as well as the shock front position is $x = 0$.

Our model used in Eq.(3.24) assumes a constant longitudinal peak field E_0 . The increase of the field during the acceleration, due to self-focusing, would lead to a non-symmetric parabolic shape, which experimental results do not support, as observed in Fig.(3.13). Another important effect we observed in simulations is an acceleration of the laser group velocity in the chirped cases, as can be observed in Fig.(3.26). By chirping and keeping the focal plane at the same shock-front injection position, the laser has a lower, yet more stable and constant peak intensity. Nonlinearities in this fashion are reduced such as self-etching or self-steepening, associated normally with a red-shift in the laser spectrum, which slows down the wakefield. According to the simulations, the unchirped case presents a dephasing around $30 - 40 \mu\text{m}$ for these densities but it elongates up to $60 \mu\text{m}$ for the chirped case. So far, the analysis of the 5 fs case has been made more qualitatively, putting major emphasis on the wakefield evolution based on Fig.(3.24) and Fig.(3.25). Less emphasis has been put on the electron spectrum since it shows less resemblance with the experimental results. For the unchirped case, the maximum electron peak energy matches quantitatively well after setting $a_0 = 1$. On the other hand, in the chirped case the electron energy is almost 2.4 times higher than what measured for the same input intensity, due to the retardation of the dephasing.

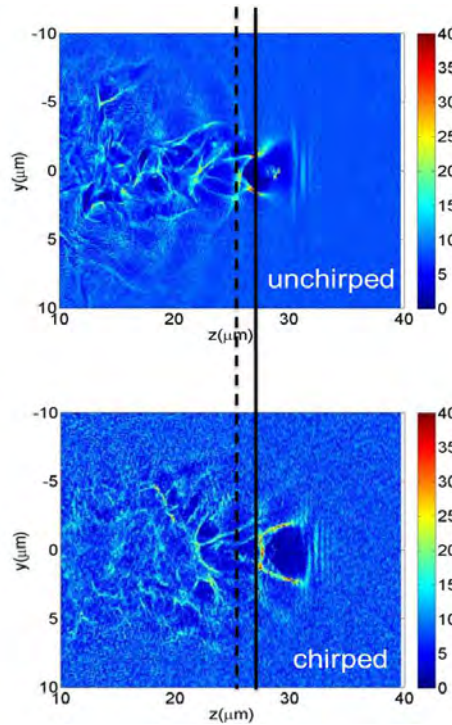


Figure 3.26: Snapshot of the wakefield excited by an unchirped (top) and a chirped pulse (bottom).

We could learn from the simulations (i) the need to chirp the laser pulse to assure the excitation of a wakefield for longer distances and (ii) reducing the input intensity suppresses nonlinear effects which would slow down the wakefield phase velocity. Moreover, the electron bunch charge diminishes as it approaches dephasing and its absolute energy spread is also reduced, as observed in the experimental data. Since the chirp is longitudinal, 2D simulations are appropriate to

simulate the laser group velocity. Furthermore, we had previously observed that shock-front injected beams are correctly reproduced in terms of final energy and energy spread in 2D as well as in 3D simulations. This is attributed to the well-known fact that for shock front, a non-linear plasma wave is initially excited but below the threshold for self-injection [131, 13], thus the process is less chaotic and lower intensities are required. At higher densities, $n_e > 8 \times 10^{19} \text{cm}^{-3}$, the agreement between simulations and experimental observations is not so good as it is with the 8 fs results.

Chapter 4

Relativistic attosecond nanoplasmonics

In the last chapter, we learned about the excitation of collective motion in underdense plasmas. Large amplitude charge oscillations reaching fields in the order of 100 GVm^{-1} were driven by the combined action of the ponderomotive and electrostatic forces. By relying on an external injection mechanism, electrons were accelerated to relativistic energies within 10's of μms , delivering sub-10 MeV few-fs quasimonoenergetic electron bunches. In this chapter, similar concepts are reviewed in overdense plasmas. Since laser-matter interaction in solids is a very broad field, sec.2.3.2 represented only a tiny prequel to what in the following pages comes. In particular, it was discussed how deep an electromagnetic field propagates in a solid before being reflected or scattered. The first section of this chapter (4.1.1) is a continuation of sec.2.3.2, starting with the absorption of the laser light by driving resonant plasma waves in solids in this small region (δ_p) where the laser can actually penetrate. The concepts of an overdense plasma and laser-matter interactions involve a handful of different targets, geometries and physics. Specifically, the action of the laser field upon targets whose spatial dimensions are limited to a fraction of an optical wavelength ($< 800 \text{ nm}$) belongs to the nanophotonics realm. Following the different absorption mechanisms, the next topic will concern the scattering of laser light on these nano-scale targets (sec.4.1.1). Nanoscale targets have proved to react completely different under the influence of an electromagnetic wave and possess surprising features. Their ability to enhance the incoming field by a factor of 10-100's, has motivated scientists to keep on working in this direction. Moreover, the intrinsic time-scale of nanotargets is $1 \text{ nm}/c \approx 3 \text{ as}$, the attosecond range. Unlike the wakefield generation where the physics are mostly described by the envelope of the laser ($\gg 1 \text{ fs}$), the dynamics of ultrafast-nanophotonics vary considerably within a half optical cycle ($< 1 \text{ fs}$). Furthermore, if the whole target is naively thought as an electron cloud which is uniformly accelerated by a strong laser field, it is straightforward to think of an attosecond electron source traveling almost at the velocity of light, thus relativistic. In a similar fashion as in LWFA, an injected electron within a plasma wave occupies a fraction of the plasma wavelength which again results in $\ll 1 \text{ fs}$ for an overdense target. Thus, there are so many indications relating "attosecond" with "nanosolids" that we can intuitively consider the attosecond range belongs intrinsically to the nano realm at some point. A review on attosecond nanophotonics will take

place in sec.4.1.3 which serves as a strong motivation for the experiment presented later on in this chapter: the generation of few-MeV sub-fs electron pulses in the framework of relativistic attosecond nanophotonics (RANP).

4.1 Nano-solids basics

4.1.1 Laser-plasma II: Light absorption and scattering in nano-solids

Optical analysis of any nanosolid starts by assuming the harmonic oscillator model introduced by Lorentz, where the electrons oscillate under the action of a weak oscillating driver $E \cos(\omega_L t)$. In this model, the dielectric function of a metal is written as a sum of j -different oscillators of resonances $\omega_{0,j}$ of the system and the free plasma electrons[19]:

$$\epsilon(\omega) = 1 - \frac{\omega^2}{\omega_L^2 + i\gamma_{ie}\omega_L} + \frac{\omega^2}{\omega_{0,j}^2 - \omega_L^2 - i\gamma_{ie}\omega_L} \dots \quad (4.1)$$

where $\gamma_{ie} = \nu_{ie}^{-1}$ is the damping constant of the plasma bulk determined by ion-electron collision rate ν_{ie} . These collisions lead to high ohmic absorption if the term γ_{ie} is not negligible. Moreover, large absorption is also expected near a resonance, $\omega_L \approx \omega_{0,j}$. Yet, how much laser energy at $I_L > 10^{15} \text{ Wcm}^{-2}$ can be absorbed by a solid target? Surely, the larger the propagation region is, the more laser is absorbed. Therefore, the plasma scale length L plays a fundamental role in describing which process takes the lead in absorbing the laser energy. Secondly, collisional absorption does not play any role in the context of highly intense femtosecond laser interactions. At $I_L \lambda_L^2 \geq 10^{15} \text{ Wcm}^{-2} \mu\text{m}^2$, the plasma temperature increases extremely fast and typical kinetic energies are $E_{kin} = 100$'s keV so that collisions $\nu_{ie} \propto E_{kin}^{-2} \ll \omega_L$, become ineffective[54]. Therefore, we will deal in the next section with collisionless absorption mechanisms.

Collisionless absorption of the laser field in solids

Resonant absorption

The propagation of an electric field into a solid was already sketched in Fig.(2.7) and Fig.(2.8). At normal incidence, the incoming electric field E_L has no component in the density's gradient direction (x), whereas at oblique incidence angle θ , decoupling of the electromagnetic E_{em} and electrostatic E_{es} fields is done by solving the Helmholtz equations for an incident electric field $\vec{E}_L = (E_x, E_y, E_z)e^{ky \sin \theta - \omega_L t}$ [104]:

$$\frac{\partial^2 E_x}{\partial x^2} + \frac{k_L^2}{\beta^2}(\eta - \sin^2 \theta)E_x = i \frac{k_L}{\beta^2}(1 - \beta^2) \sin \theta \frac{\partial E_y}{\partial x}, \quad (4.2)$$

$$\frac{\partial^2 E_y}{\partial x^2} + \frac{k_L^2}{\beta_e^2}(\eta - \sin^2 \theta)E_y = i \frac{k_L}{\beta^2}(1 - \beta^2) \sin \theta \frac{\partial E_x}{\partial x}, \quad (4.3)$$

$$\frac{\partial^2 E_z}{\partial x^2} + k_L^2(\eta - \sin^2 \theta)E_z = 0. \quad (4.4)$$

where β is the product of the phase and group velocity of the electrostatic wave. Thus, there is no source-term on the right hand side for E_z , making s -polarized light, i.e. $E_L = E_z$ decoupled and of purely electromagnetic nature. In the case of $L \ll \lambda_L$ and $E_L = E_z$, the index of refraction can be linearized and the penetrating field follows an Airy function shape, resembling Fig.(2.7). It can be shown that at $n_{\text{turning}} = n_{cr} \cos(\theta)^2$ and p-polarized incident laser, the density perturbation has a singularity and, unlike E_z , an electrostatic wave $E_{x,es}$ can actually be driven resonantly by the laser field $E_{y,L}$ at $\omega_{es} \equiv \omega_p = \omega_L$ at and $k_{es} \approx k_{em} \approx 0$ at the turning point $n = n_{\text{turning}}$ [104]. These excited electrostatic modes E_{es} depend considerably on the incident angle. At small incident angles $\theta \approx 0$, though much of the intensity reaches the critical point $n_{cr}(\theta) \approx n_{cr}$, the driver $E_{y,L}$ is small and so the E_{es} modes. For an intermedium angle, the excitation is maximum while for very large angles, too much of the incoming laser light is too early reflected and resonance loses efficiency. The resonance finishes at d_R , where the superimposed electric field $|E_x|^2 = |E_{x,es} + E_{x,L}|^2$ reaches its maximum. It scales as $d_R \propto (Lk_1)^{1/3}/k_1$, where $k_1 = k_L/\beta$ and peaks at an angle $\sin \theta \approx (2k_L L)^{1/3}$. These waves are not reconverted in laser light but are absorbed completely by the plasma. In a similar way as in LWFA, plasma waves can be strongly driven when the laser intensity $I_L \geq 10^{18} \text{ Wcm}^{-2}$. Here, as well as in Fig.(3.2), the electro-static modes are no longer sinusoidal but present the typical spike-like behavior in the electron density. At later times, only the first maximum before the returning point remains strong due to posterior wavebreaking and particle trapping. Resonance absorption is quenched when $L \rightarrow 0$ and the classical Fresnel's formulas prevail.

Vacuum heating (Brunel effect)

At steep and highly dense profiles, the resonance absorption picture fades ($\omega_p \gg \omega_L$). The quivering amplitude of the electrons surpasses the plasma scale length and resonance is very ineffective. Nevertheless, other collisionless manners to absorb the laser light are in play: The Brunel effect [11] or vacuum heating [55]. As shown in Fig.(2.8a), a small sheath δ_p of electrons are under the influence of the laser field. Thus, a thermal electron arriving at the surface at the correct time can be pulled into vacuum extremely fast by the laser field ($\ll c/\lambda_L$) and when the field changes its sign, be accelerated back into the target where it is eventually absorbed back the plasma. This model is based on the capacitor approximation. This assumes an obliquely-incident laser field E_L with a component normal to the target surface $E_s = E_L \sin \theta$, extracting a displaced electrons slab of surface density $\Sigma \propto E_s/(4\pi e)$ outwards from its original position. This slab will be pushed inwards, acquiring a final velocity of v_d when it returns to the plasma. It can be derived that the final absorption rate A is [54]:

$$A = \frac{1}{a_0\pi} f \left[(1 + f^2 a_0^2 \sin^2 \theta)^{1/2} - 1 \right] \tan \theta \quad (4.5)$$

where $f = 1 + (1 - \eta_a)^{1/2}$, which is the amplification factor of the incoming laser field at the surface:

$$E_s = f E_L \sin \theta, \quad (4.6)$$

By writing $\eta_a = 1 - (f - 1)^2$ and letting $\nu = a_0 \frac{\sin(\theta)^3}{\cos(\theta)}$, we obtain that in the strongly relativistic limit $\eta_a \approx \frac{4\pi\nu}{(\pi+\nu)^2}$, where $\nu = \frac{\sin(\theta)^3}{\cos(\theta)}$. Hence, the absorption rate is independent of a_0 and even reaches unity at an angle around 70° . Simulations [55] showed a transition between resonance

absorption and vacuum heating as a function of the laser irradiance and the plasma scale length. Absorption values beyond 60% were reached at lower intensities $I_L \approx 10^{14} \text{ Wcm}^{-2}$ and $L/\lambda_L = 0.04$ or at $I_L \approx 10^{16} \text{ Wcm}^{-2}$ and $L/\lambda_L = 0.1$. Vacuum heating mechanism saturated around 15% for very relativistic cases. The reason for this lies in the fact that the capacitor approximation neglects the magnetic field and the term $v \times B$ in the Lorentz eq., which is not longer valid at $a_0 \gg 1$. The majority of electrons which leave into vacuum do not return due to the large magnetic field. Yet, absorptions of 70-80% have been measured at relativistic intensities [21] and very steep targets, much beyond any vacuum heating prediction.

Another important nonlinear collisionless absorption mechanism has been proposed: $\vec{j} \times \vec{B}$ heating [86]. At relativistic intensities, the magnetic field is not negligible anymore. The $\vec{j} \times \vec{B}$ heating handles with similar physics as explained before, with the term E_s being substituted by the nonlinear component of the Lorentz force $\vec{v} \times \vec{B}$. In this scenario, the electrons are ponderomotively accelerated in vacuum and back into the target at double the laser frequency since $v \propto \sin(\omega_L t + \phi)$ and $B \propto \cos(\omega_L t)$, yet the phase relationship between the current \vec{v} and the \vec{B} field is much more complicated. The latter processes, along with many others [104], are not well separated from each other and fail to provide an explanation to high-absorption measurements, supported by PIC simulations. Such a high absorption must have its origin in a resonant-like of process.

According to Poynting's theorem, absorption fundamentally deals with the phase shift ϕ between the generated current $j \propto \sin(\omega_L t + \phi)$ and the driving electric field $E \propto \cos(\omega_L t)$:

$$\nabla \cdot \langle \vec{S} \rangle = -\vec{j} \cdot \vec{E} \propto \frac{1}{2} \sin \phi \quad (4.7)$$

where $I_L = \langle |\vec{S}| \rangle$. The equation above implies that only a phase shift of $\pi/2$ between plasma free electrons and the driver E would lead to a maximum absorption/energy gain. Resonance absorption ($\omega_p = \omega_L$) at very steep ($L/\lambda_L \ll 1$) and highly overdense ($\omega_p/\omega_L \gg 1$) was ruled out for a long time by the scientific community since the electron trajectory in phase space was modeled only by the classical harmonic oscillator model. Yet, new theoretical models were developed based on dividing the target in sub-nanometer slabs and solving a nonlinear oscillator equation for each of them. Hence, larger frequency modes are incorporated to the physical picture, which contribute to the overall phase shift between the driving electric field and the generated current [105]. In this description, the electron sheaths are pulled out of the target into vacuum where they oscillate for a short time before being dragged brusquely back into the target. Layers leaving from the rear of the target are replaced by cold and fresh new layers. This anharmonic resonance model is capable of describing electron energy gains well beyond the laser ponderomotive energy within few-cycles of light, much larger absorption coefficients and applicable to any kind of overdense target.

As seen along this section, the absorption of laser energy is an immensely rich function of the angle of incidence, plasma scale length, laser polarization, skin depth, etc. Moreover, excitation of plasma waves at the surface play a key role in understanding the physics behind the macroscopic absorption coefficients. In the same fashion, scattering of laser light from a plasma target is a combined view of classical electromagnetism and the plasma collective response. In particular, the electrostatic fields rising on the target's surface are of fundamental relevance for acceleration

mechanisms.

Mie plasmons

Very steep gradients lead to the appearance of such surface plasmons (SP's) which are responsible for light scattering processes [95]. We learned in sec.4.1.1, that only p-polarized light excites charge density waves at the interface of any target, therefore there must be a component of the electric field normal to the surface. Choosing the x-axis to be the propagation direction of a wave along the interface between two media at $z = 0$, we have:

$$E_i = (E_x, 0, E_z)e^{-|\kappa_i|z}e^{i(q_ix - \omega t)} \quad (4.8)$$

where $i = 1, 2$ describes the medium at $z < 0$ and $z > 0$, respectively. From applying the Maxwell's Eq. 2.7, one finds:

$$\kappa_i = \sqrt{q_i^2 - \epsilon_i \omega^2 / c^2}. \quad (4.9)$$

Moreover, boundary conditions force the tangential components of the electric fields to be continuous. It can be shown that this implies the following condition [114]:

$$\frac{\epsilon_1}{\kappa_1} + \frac{\epsilon_2}{\kappa_2} = 0, \quad (4.10)$$

which is referred to as the surface plasmon condition, and

$$q_1 = q_2 = q, \quad (4.11)$$

$$q(\omega) = \frac{\omega}{c} \sqrt{\frac{\epsilon_1 \epsilon_2}{\epsilon_1 + \epsilon_2}}. \quad (4.12)$$

which determines the dispersion relationship of the SP's. The solution of $\omega(q)$ to large values of q is given by the solution of:

$$\epsilon_1 + \epsilon_2 = 0. \quad (4.13)$$

which is a special case of Eq.(4.10) for $\kappa_1 = \kappa_2 = q$, called the nonretarded surface plasmon condition, assuming $\omega/c \ll q$. Hence, this relationship corresponds to $\lambda_L \gg R$, since $q \approx 1/R$, where R is the size of the target. The particular case of a plasma medium in vacuum ($\epsilon_2 = 1$), ϵ_1 given in Eq.(2.21), the nonretarded limit converges to $\omega \equiv \omega_{sp} = \omega_p / \sqrt{2}$. Moreover, the expansion of the SP field into vacuum and into the material is characterized by a length of l_i defined by $\kappa_i = 1/l_i$. In particular, l_2 is given by:

$$\kappa_2 = \frac{\omega}{c} \sqrt{\frac{-1}{1 + \epsilon_1}} \quad (4.14)$$

$$\rightarrow l_2 = 1/\kappa_2 = \frac{c}{\omega} \sqrt{\frac{\omega_p^2}{\omega} - 2} \approx \frac{\lambda}{2\pi} \frac{\omega_p}{\omega}. \quad (4.15)$$

. From the equation above, it is easy to realize that the spatial extension of the plasmon in vacuum exceeds the wavelength ($l_2 > 1/q$), while in the material it is limited to the skin depth $l_1 \equiv \delta_p \ll \lambda$, discussed already in sec.2.3.2, leading to a high plasmonic energy density at the

target's surface. A similar analysis under these conditions is done to other types of geometries, such as spherical or cylindrical, where the nonretarded SP condition found to be [114]:

$$l\epsilon_1 + (l+1)\epsilon_2 = 0, \quad l = 1, 2, 3 \dots \quad (4.16)$$

with the corresponding resonances: $\omega_l = \omega_p \sqrt{\frac{l}{l+2}}$, referred to as the Mie plasmon frequencies. In particular, the dipole resonance corresponds to $l = 1$ and $\omega_1 = \omega_p/\sqrt{3}$.

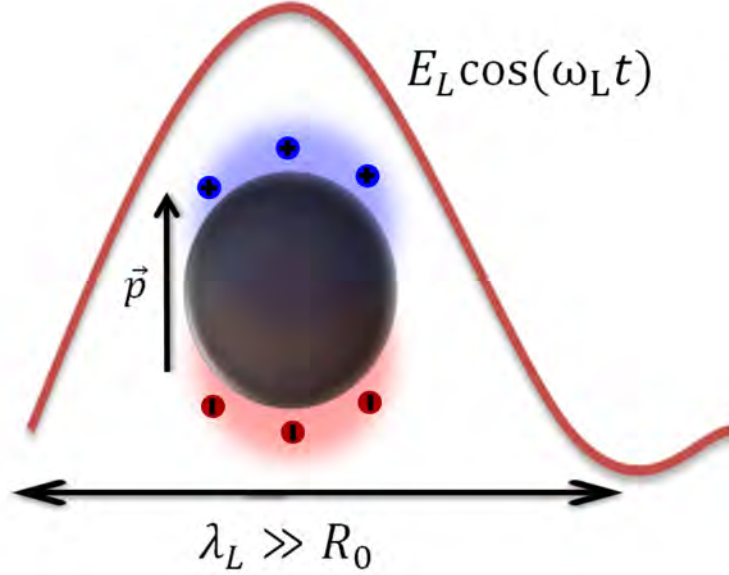


Figure 4.1: Schematic of charge separation in a nanoparticle with radius R_0 .

Inherited from the Lorentz model, surface-bound charge density in nano-scale targets undergo harmonic oscillations at the laser frequency, resembling an antenna \vec{p} under the dipole approximation, i.e. target size much smaller than the laser wavelength. See Fig.(4.1). For nano-scale objects, localized surface plasmon excitation (LSP) takes place. Hence, the laser light penetrates the target up to δ_p and shifts the electrons. Such a coherent and periodic displacement of charges leads to the resonant excitation of plasma waves at the surface driven by the laser field when $\omega_L = \omega_l$. The emitted radiation is related to the degree of polarizability, i.e. the sensitivity of the target under the influence of an oscillatory field. In particular, a metallic sphere of radius R_0 with dielectric function ϵ_1 under the action of an incoming field E_{in} in vacuum ($\epsilon_2 = 1$) will have a polarizability α [165]:

$$|\vec{p}| = \alpha E_{in} \quad (4.17)$$

$$\alpha = \begin{cases} 1 + \frac{\epsilon_1 - 1}{3} \frac{2R_0^3}{r^3}, & r > R_0, \\ \frac{3}{\epsilon_1 + 2}, & r < R_0, \end{cases} \quad (4.18)$$

which reaches a maximum exactly at resonance given by Eq.(4.16) for $l = 1$ [27]. The excited emitting dipole has a larger maximum electric field $E_{scat} \approx 3E_{in}$ at $r \geq R_0$ for $\epsilon_1 \rightarrow \infty$, i.e.

highly dense targets. Yet, these "hot spots" are very localized and non-propagating, i.e. bound to the skin depth. At resonance, the energy removed from the driving laser is due not only to scattering but absorption as well. The scattering σ_{scat} and the absorption σ_{abs} cross sections are [43]:

$$\sigma_{scat} = \frac{8\pi}{3} k_L^4 R_0^6 \left| \frac{\epsilon_1 - 1}{\epsilon_1 + 2} \right|^2, \quad (4.19)$$

$$\sigma_{abs} = 4\pi k_L R_0^3 \text{Im} \left[\frac{\epsilon_1 - 1}{\epsilon_1 + 2} \right], \quad (4.20)$$

and scale as R_0^6 and R_0^3 , respectively. Thus, small particles ($k_L R_0 \ll 1$) are capable of absorbing more energy, whereas larger targets scatter out more laser energy. As a direct consequence, the absorbed energy is more concentrated and the field-enhancement factor is higher in smaller particles. Enhancement factors of $\gg 1$ have been reported in recent experiments[68].

As the dipole approximation fails ($k_L R_0 \geq 1$), higher order modes are excited, with corresponding polarizabilities $\alpha_n \propto \frac{l(\epsilon_1 - 1)}{l\epsilon_1 + (l+1)} R^{2l+1}$. The mode expansion depends mainly on the size parameter $x = 2\pi R_0 / \lambda_L$. A truncation for the number of modes is given by $l_{max} = x + 4x^{1/3} + 2$. Hence, the near field adapts itself strongly to let higher modes be coupled. Nevertheless, even in this multi-mode scenario, the dipolar mode is the one with the largest spatial extent. How resonances affect the plasmonic system is seen very intuitively in the Lorentz model, seen in Eq.(4.1). In the locality of $\omega_L \approx \omega_l$, this particular mode l has a singularity and dominates the dielectric response. A formalism based on Green functions can be found in the literature [138] and is beyond the scope of this work.

A rigorous solution of the Helmholtz equations was calculated in the work of Mie in 1908, who shed light on the interaction of light with a spherical homogeneous target of any particular size in a homogeneous medium. This implies finding a solution of the type:

$$\nabla^2 \vec{E} + k_m^2 \vec{E} = 0; \quad (4.21)$$

with $k_m^2 = \omega^2 \epsilon_m / c^2$, being ϵ_m the relative electric permeability of the surrounding medium and $m = \text{round} \left[\frac{\text{Re}[\epsilon_1]}{\text{Re}[\epsilon_2]} \right]$. The solution to the scattered field in the spherical domain (with unitary $\vec{r}, \vec{\theta}, \vec{\phi}$) is given by a linear combination of the $\vec{M}_{l,m}$ and $\vec{N}_{l,m}$, the vector spherical harmonics. Check [9] for more details on how to determine the "Mie coefficients" of this combination. In Fig.(4.2), we appreciate the incident plus scattered field from nano-scale particles of different radius: 100, 400 and 1000 nm and index of refraction $n = 1.5 + 0.1i$ [108]. All fields are normalized to the incoming one, $E_{in} = 1$. Here, we notice many key aspects:

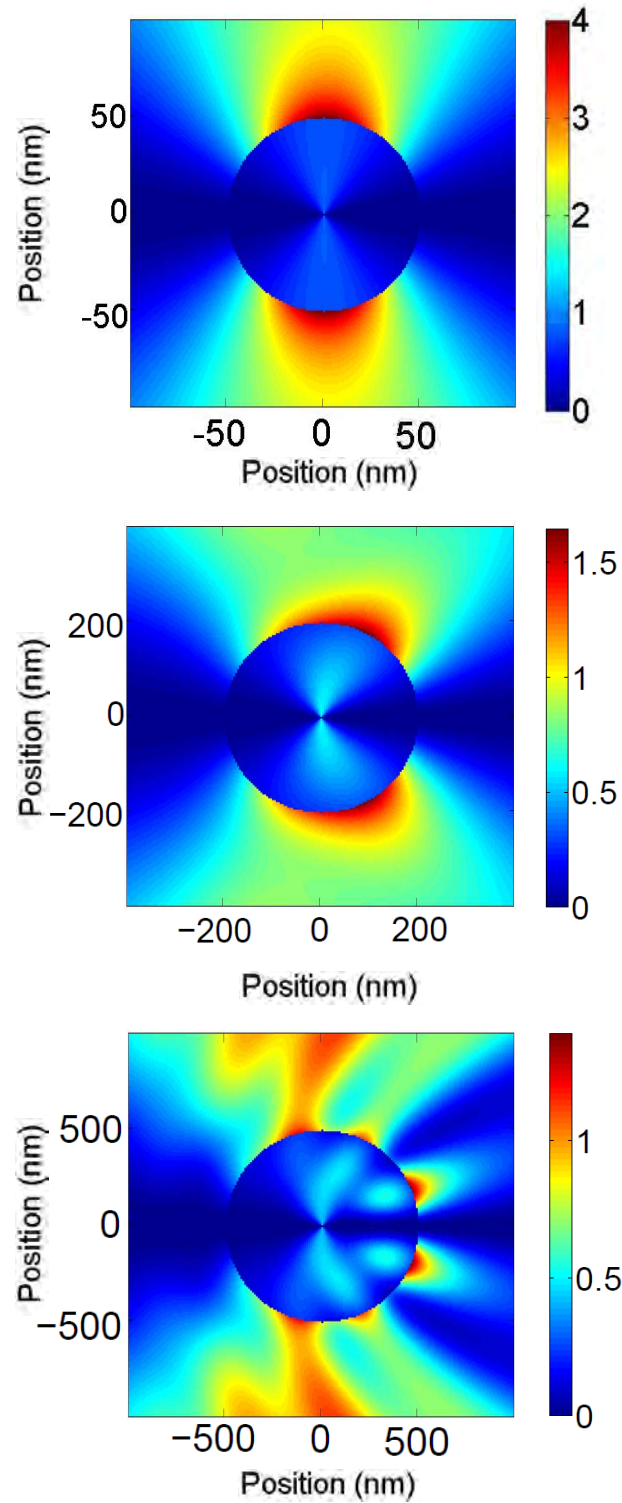


Figure 4.2: Value of radial electric field, normalized to the incident field for particles of radius 50,200 and 500 nm. The color scale indicates the enhancement factor of the incident electric field. Incident field is a plane wave with amplitude $E_{in} = 1$ and $\lambda_L = 740$ nm. Calculations were done using the code from [128]

1. The scattering angles are almost $\pm 90^\circ$ for very small particles $x \ll 1$. The target behaves as a dipolar antenna, the 2 "hot spots" are located at the poles and only the $l = 1$ mode is present. This is the classical Rayleigh regime. Nevertheless for intermediate sizes, i.e. $x \approx 0.5$, higher modes are coupled in and the emission angle shifts in the forward direction to about $\pm 60^\circ$. The role of the other 2 "poles" at the rear of the particle will be discussed later. The target resembles now a quadrupole, due to a significant contribution of the $l = 2$ mode. Finally, for $x \geq 1$, multiple modes are excited and the numerous "hot spots" are located at many positions along the particle's surface, being the 2 most contributing at the very front, at about $\pm 10^\circ$.
2. The field localized at the "hot spots" exceeds the incident field $E_{scat} = \varsigma E_{in}$. The so-called near-field enhancement factor ς is, as mentioned before, higher for smaller particles. Furthermore, these poles are symmetric with respect the equator of the particle.
3. Fig.(4.2) is frozen in time. Yet, the driving field oscillates at ω_L . The whole physical picture is visible in Fig.(4.3) showing the absolute value of radial electric field as a function of the laser cycles and the scattering angle. The SP's temporal duration is a small fraction of an optical cycle, i.e. 100's as. This is the key for the rest of the chapter and it is the strongest motivation for the experiment presented in this chapter.
4. In sub-sec. (4.1.1) we saw that the absorption depends highly on the incident angle at which the laser impacts the target. Therefore, it is not surprising at all that the scattering angle for the different targets also varies, from $\pm 90^\circ$ to 0° .

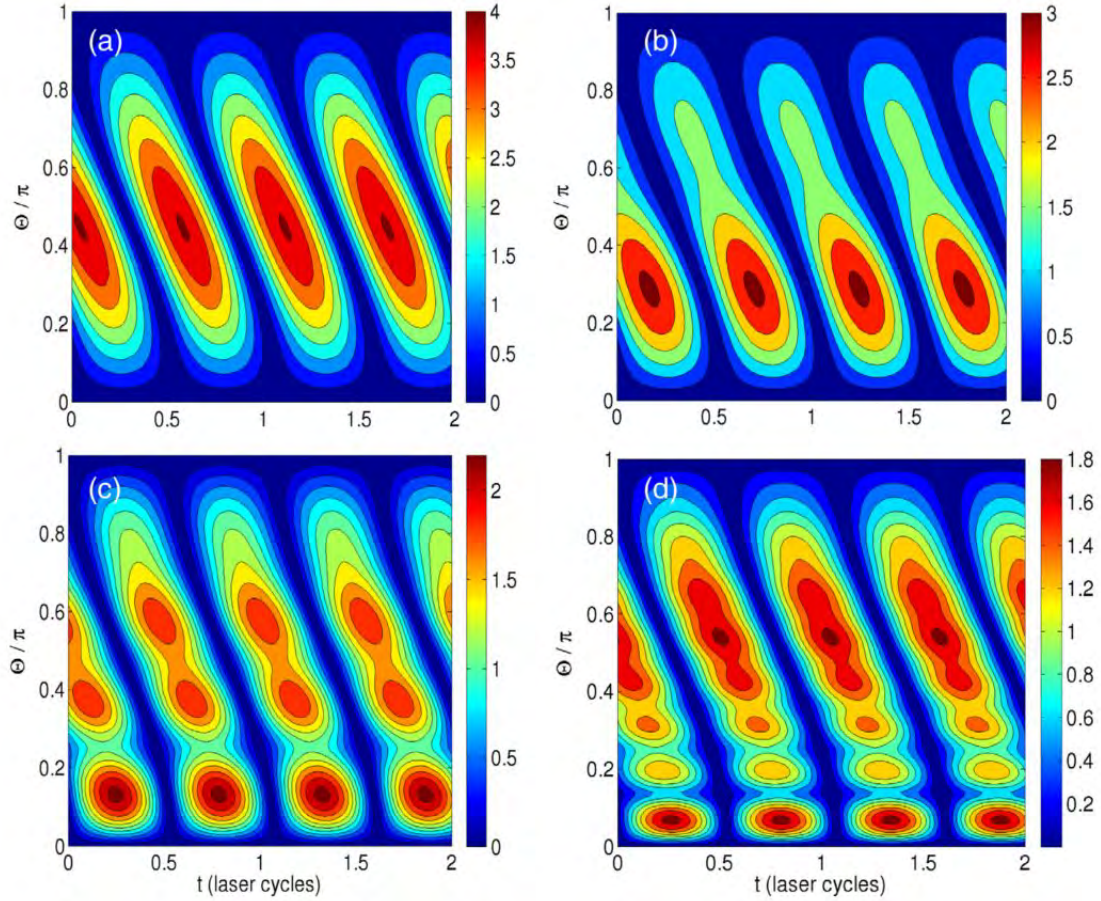


Figure 4.3: Value of the radial electric field normalized to the incident field for a 100 times overdense droplet with $R_0 = 100$ nm (a), 200 nm (b), 500 nm (c), and 1 micron (d) in a incident plane wave of wavelength $\lambda_L = 800$ nm as a function of time and angle on the surface. The color scale indicates the enhancement factor of the incident electric field E_0 , for a constant plane wave amplitude. Figure reproduced from [36].

Nanoplasmonics has yielded incredible promising results up to date. Enhancement factors of $\gg 1$ have allowed modest intensity lasers to reach other regimes and applications among others in biology, chemistry and industry. Steering the direction back again to laser-driven particle accelerators, it has been demonstrated that nJ-level ultrashort light pulses can excite SP's in a Kretschmann-Raether configuration, and reach accelerating fields of multi-GV/m [116, 65] and keV-class electrons [71, 72, 37]. It is precisely the ability of SP's to "nano-scale" confine the incoming electromagnetic energy yielding much larger fields. The idea of an intensity multiplier seduces the scientific community including those already in the high field branch. Ponderomotive acceleration of relativistic laser pulses of $a_0 = 5$ is limited to few-MeV range, yet SP-triggered mechanisms (via a nano-grating) have led to multi-10 MeV [49].

4.1.2 Sub-cycle (non-ponderomotive) acceleration in plasmonic fields

Since practically almost all the work done in nanoplasmonics has been realized at moderate intensity $I_L \approx 10^{12-14} \text{ Wcm}^{-2}$, many of the following concepts apply only for low intensity regimes. Nevertheless, they represent a good introduction to understand the experimental results presented later. The plasmon-induced electron emission can be described by a two-step model, in analogy to the high-harmonic-generation mechanism studied in [30]. In the first step, free electrons are created by tunnel ionization for Keldysh parameter $\gamma_K \ll 1$. The resulting sub-cycle photo-induced or plasmon-induced current density has a certain probability of following the driving laser field E_L , being dragged rapidly into vacuum, in a "vacuum heating" fashion. The most common formula applied to metals in the tunneling regime is the Fowler-Nordheim equation [8, 69, 67]. The instantaneous current $j(t)$ follows:

$$j(t) \propto \frac{e^3 E_L(t)^2}{8\pi h W} e^{\left(-\frac{8\pi\sqrt{2m_e}W^{3/2}}{3h e |E_L(t)|}\right)}, \quad (4.22)$$

where W is the work function of the metal. This ultra fast current presents already some sub-fs features, as seen in Fig.(4.4). Does this contribute positively in our motivation to generate attosecond electron pulses? Yes. Nevertheless, as we will see in the experimental part, in the ultra relativistic regime the whole interaction can be very accurately described without taking into account any ionization mechanism.

The second step consists of acceleration of free electrons in the plasmonic evanescent field. Different birth times will correspond therefore to different final kinetic energies, similar to high-harmonic generation in gases [30, 84]. In a classical homogeneous field, electrons born at the start of a half-cycle are accelerated the most. Such times are considered the "ideal" times for direct and efficient acceleration and lead to the classical $2U_p$ energy cut-off [112]. Nevertheless, due to high localization and strong temporal decay of the fields in nanoparticles, the best time for acceleration is somewhat retarded [63]. Too early particles may leave the well-confined field before it reached its maximum, quenching the energy gain too soon. Furthermore, for short ($\ll \lambda_L$) plasmon decay length's in vacuum, $l_{dec} \equiv l_2 = 1/\kappa_2$ from Eq.(4.15), the electrons emitted in the beginning of the first half-cycle reach a weaker field position before they are dragged again into the target, avoiding the usual back-acceleration of the quivering regime and later re-scattering, as shown

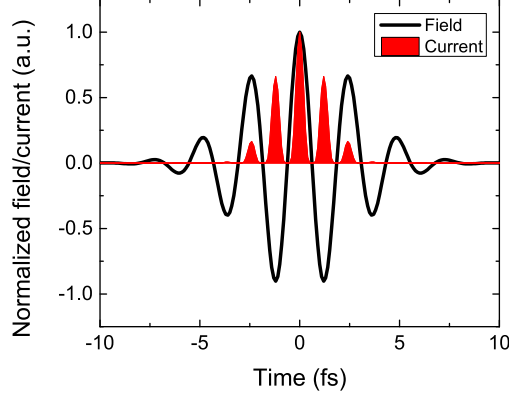


Figure 4.4: Electric field of a 4.5 fs laser pulse (black line) and the instantaneous emission current density (red), following Eq.(4.22) for 1 TV/m field strength and 50 eV work function, typical for Tungsten for the higher electron orbits.

in Fig.(4.5). To which extent the high confinement of the SP's plays a role is defined by the dimensionless δ -parameter [63] relating the quivering amplitude $l_q = a_0\lambda_L/2\pi$ and the plasmon decay length l_{dec} :

$$\delta = \frac{l_{dec}}{l_q} \begin{cases} = \frac{l_{dec}m_e\omega_L^2}{eE_L} \propto \lambda_L^{-1}, & a_0 \ll 1 \\ \approx \frac{\sqrt{n_e/n_c}}{a_0^{3/2}}, & a_0 \gg 1 \end{cases} \quad (4.23)$$

where $\omega_p^2/\omega_L^2 \rightarrow (n_e/n_c)a_0^{-1/2}$, including the relativistic corrections to the electron density from sub-sec.(2.3.1). The wavelength dependence from the original formula is hidden behind n_c and a_0 .

Most of the previous experiments with nanoplasmonics, such as [165], have been realized at moderate intensity $I_L \approx 10^{12-14} \text{ Wcm}^{-2}$ using visible-near-IR lasers, fulfilling $\delta > 1$. In the quivering picture, the acceleration and back-acceleration of the electron in an homogeneous field prevails. Only at $\lambda_L = 8 \mu\text{m}$, was $\delta < 1$ as reported by [63]. Here, the plasmonic field decreases significantly during the electron quivering. In this scenario, so-called sub-cycle regime, the classical ponderomotive energy gain is quenched, as described above, and the energy cut-off's for direct and back-scattered electron emission of $2U_p$ and $10U_p$, respectively, converge to an unique and lower value (see Fig.4 in [63]). The wavelength limitation can be compensated by applying extremely large intensities $I_L \approx 10^{20} \text{ Wcm}^{-2}$, In the following scenario: $a_0 \approx 5$ and $n_e/n_c = 100$, we obtain $l_{dec} \approx 530 \text{ nm}$ while $l_q = 590 \text{ nm}$. Thus, $\delta < 1$. We enter the sub-cycle regime.

4.1.3 CEP effects in nanoplasmonics

The quivering regime is also not valid anymore when the driver field is intense enough and limited to almost a single cycle. The quivering amplitude changes significantly from one cycle to the next, as the field envelope a_0 is not a smooth function anymore and the instantaneous intensity

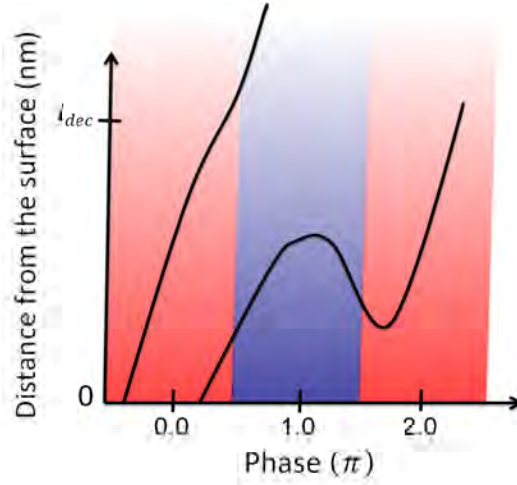


Figure 4.5: Illustration of electron trajectories in localized fields. Most of the electrons leave the surface rapidly, while electrons with later birth times $> \pi/4$ wiggle in the field and back-scatter. Figure inspired from [63]

contrast depends highly on the CEP. Thus, all electron parameters depend highly on the phase of the field. Control over the CEP has been the hallmark of the attosecond science since its birth [84]. On the other hand, relativistic laser-plasma interactions were used to depend mainly on the intensity envelope of the driver. First results came [10] at the limit of the relativistic threshold $a_0 = 0.4 - 0.7$. This barrier is about to be pushed by almost two orders of magnitude away when LWS-20 sub-5 fs pulses are employed. Yet, before coming to the experiments, let us review at least some CEP effects observed so far using moderate nonrelativistic drivers and nanotargets, where enormous contributions in this direction were made at MPQ.

Fig.(4.4) shows a hint of the most obvious phase-dependent effect we can think of: the electron current, or just electron yield. Tunnel ionization simulations yield a clear asymmetry regarding the amount of electrons ejected to each side, as demonstrated experimentally in [165] by studying the electron emission out of SiO_2 nanoparticles. Here, they discovered space charge repulsion to be responsible for very large enhancement factors in back-scattered electron spectra. Moreover, by taking advantage of the size-dependence of the localization of the near-fields in these nanoparticles, as seen in sub-sec.4.1.1, complete control over the directionality and electron yield was accomplished [142]. Furthermore, the biggest contribution of the Mie near-field resulted mainly radial, leaving the tangential component a non-crucial role.

Although ionization mechanisms are not the topic of this chapter, and rather left aside, in the relativistic regime the total number of electrons from a solid-target can be estimated following the vacuum heating picture. The normal component of the field E_s acts on the surface extracting an electron sheath of surface density Σ down to a depth of δ_p . Thus, the number of extracted electrons N is [2]:

$$N \approx \Sigma \delta_p \propto E_L \lambda_L \sin(\theta) \sqrt{(n_c/n_e)} \propto \begin{cases} \sqrt{I_L} \\ \frac{1}{\sqrt{n_e}} \end{cases} \quad (4.24)$$

from where we obtain the scalings $N \propto n_e^{-1/2}$ and $N \propto I_L^{1/2}$. A "cosine" laser pulse of 4.5 fs pulse duration has an intensity ratio 1:0.8 between main peak (pointing left L) and the two consecutive lower maxima (pointing right R) next to it. A naive calculation would estimate already a yield ratio of $\sqrt{L/2R} = \sqrt{1/(2 \times \sqrt{0.8})} = 0.56$ and an asymmetry parameter $A = (L - R)/(L + R) \approx 0.3$. So, any observable (yield, direction, spectrum, divergence, etcetera) which is field dependent, becomes a sensitive function of the CEP.

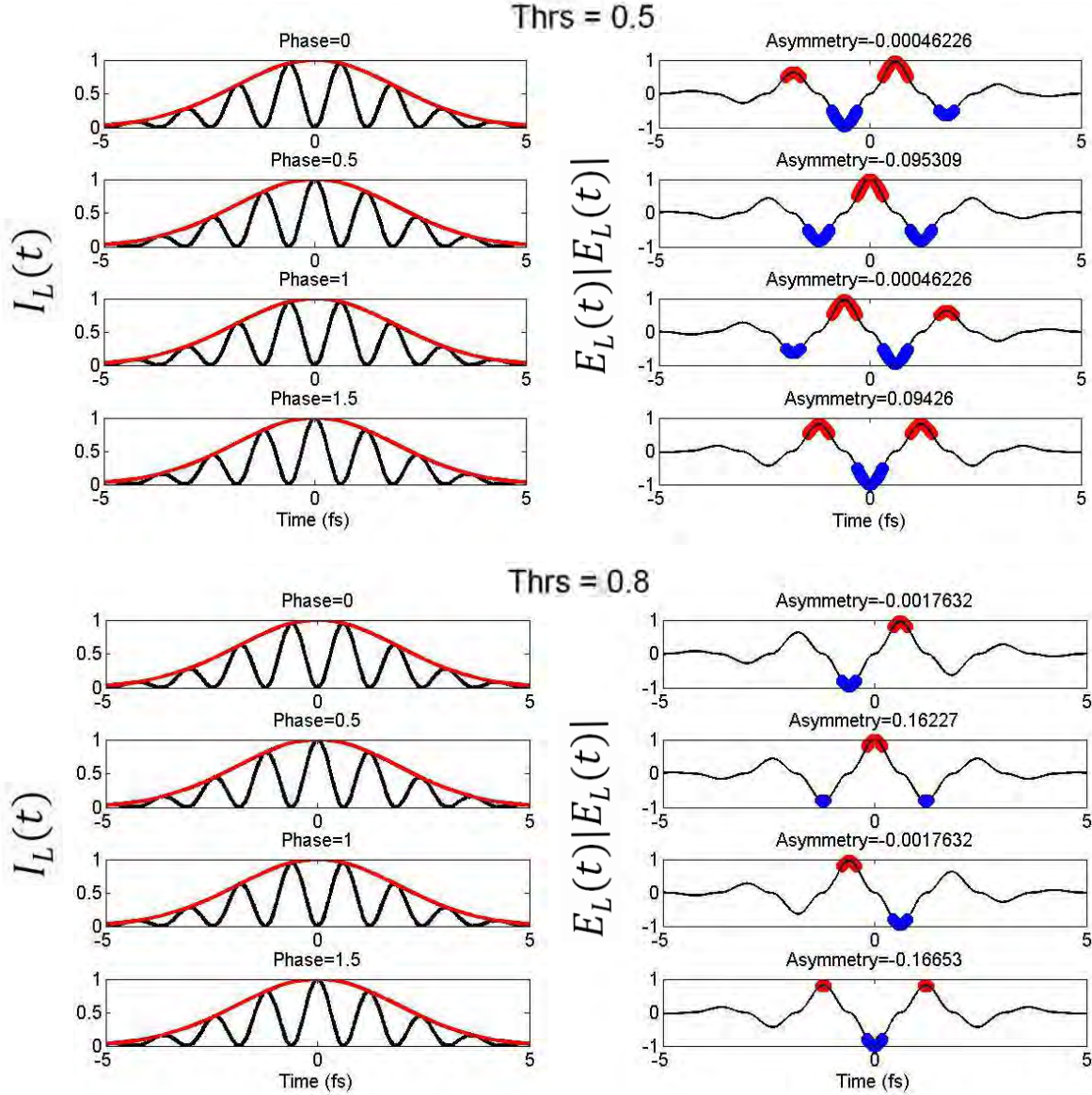


Figure 4.6: Left: Instantaneous intensity I_L (black) and envelope (red). Right: $E_L|E_L|$, where positive (negative) values correspond to left (right) direction. Highlighted in red (blue) the $E_L|E_L|$ above a certain threshold value ($|E_L| > \text{thrs}$).

Tunnel ionization or any nonlinear process which extracts the electrons from the solid's surface

occurs in a certain time-window around the electric field maximum for each half-cycle. Moreover, the Coulomb potential in the ionized target may narrow such time-window down, in particular in a largely-emitted charge scenario. Unlike Tunnel ionization which is an extreme nonlinear process, this narrow time-window is determined by the minimum escape energy of the electrons, given in Eq.(2.11). This corresponds to a certain threshold in the instantaneous intensity $I_L(t)$ as described in Fig.(4.7). By integrating the "directional" instantaneous intensity $E_L|E_L|$, at left and right, sinusoidal asymmetries A_N for this particular observable are obtained following the scaling from Eq.(4.24). A saturation and "rectangularization" [122] of A (no longer sinusoidal) would either result from an extreme nonlinear reaction or shortening the laser pulse to one single cycle. Furthermore, it is interesting to note that, depending on threshold level, the final asymmetry is actually invertible for the same laser waveform.

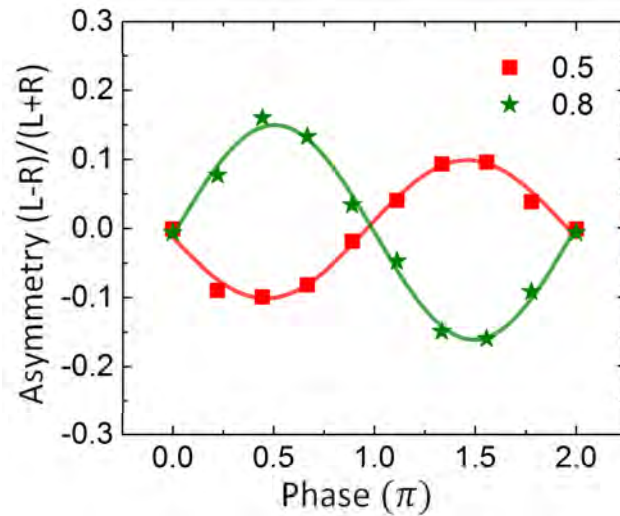


Figure 4.7: Asymmetry parameter A for the case of Fig.(4.6)

Finally, the experimental part. We shot at Tungsten nanotips with the purpose of generating relativistic attosecond electron bunches and exploiting the strong field dependence of the electron emission on the optical field. To this end, we describe in the following section the experimental setup and how we measure the electron bunch parameters in sec.4.2, followed by the findings in sec.4.3.2 and sec.4.3.3 and discussion, 4.3.4.

4.2 RANP experiment setup

The LWS-20 laser beam is transported in vacuum from the laser laboratory to the RANP experimental chamber (see Fig.(4.10), where it is focused to a focal spot size of $\sigma_{\text{FWHM}} = 1.22 \mu\text{m}$ using a $f = 50 \text{ mm}$ and F#1 off-axis parabolic mirror. Peak intensity calibration ($I_0 = 0.5 - 1.3 \times 10^{20} \text{ Wcm}^{-2}$), Rayleigh length ($Z_R = 4.8 \mu\text{m}$) as well as laser pointing $< 7 \mu\text{rad}$ ($\approx \lambda_L/2$) were measured by imaging the focal spot with a long-working distance microscope objective ($\times 20$) to a CDD camera outside the chamber, see Fig.(4.8). Even though $1.3 \times 10^{20} \text{ Wcm}^{-2}$ was the maximum intensity during the experimental campaign, on the most experimental days the peak intensity was about $I_0 = 6 \times 10^{19} \text{ Wcm}^{-2}$, $a_0 = 4.9$ due to larger imperfectly compensated wavefront aberrations.

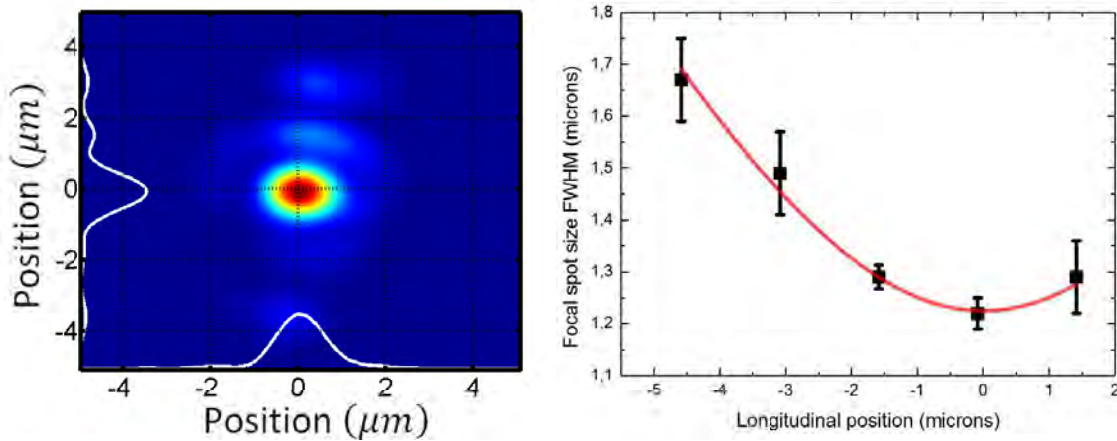


Figure 4.8: Left: Laser focal spot focused by an F#1 off-axis parabolic mirror to $\sigma_{\text{FWHM}} = 1.2 \mu\text{m}$. Right: Rayleigh length measurement. The continuous line corresponds to a $\sigma_{\text{FWHM}} \sqrt{1 + (x - x_0)^2 / Z_R^2}$ fit.

Each target was aligned independently as shown in Fig.(4.11). After imaging the focal spot size and marking its position at its minimum size, the target was imaged to the same focal plane by an extra 3D translation stage. The target was positioned independently with 1 nm stage accuracy. The maximum uncertainty in the longitudinal direction is actually less ($\times \approx 1/2$) than the depth of field, $\text{DOF} = 1.7 \mu\text{m}$, of the microscope due to extremely high spatial resolution of the positioning stage. The latter allowed us to interpolate between the two longitudinal positions where the target image became unsharp. Moreover, it is known that the phase of a focused Gaussian beam shifts over $\pm\pi/2$ along the Rayleigh length. The amplitude of this effect is again

fixed by the resolution of our positioning imaging in the longitudinal direction, i.e. $\text{DOF}/2$, as sketched in Fig.(4.9), yielding an uncertainty of $\Delta_{\text{Gouy}} = \pm \text{atan}(\frac{\text{DOF}/2}{Z_R}) \approx \pm 170 \text{ mrad}$.

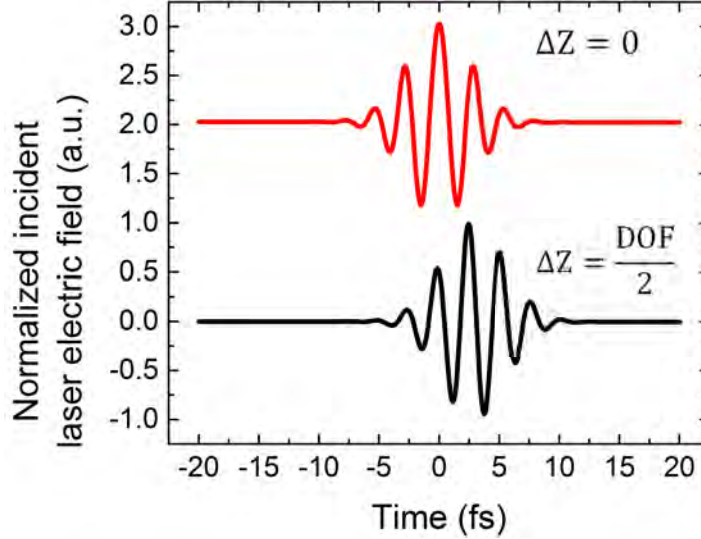


Figure 4.9: Gouy phase shift provided the resolution of the alignment in the longitudinal direction.

The electron angular distribution was measured by placing two imaging and absolutely calibrated scintillating screens, labeled S_L and S_R , covering an angle of -90° to $+5^\circ$ and 15° to 75° , respectively. For the sake of completeness, a third screen S_T was placed on top of the target covering a solid angle of $\approx 2.5 \text{ sr}$. The electron spectrum was measured by placing the same dipole magnet used in the LWFA experiment 3.2.1, about 2.5 cm away from the target (after removing S_L) with an entrance aperture of $5 \times 10 \text{ mm}^2$ and its exit with scintillating screens imaging to a CDD outside the chamber. Parameters such as electron directionality θ_{Left} or full electron yield N_e were only measured in S_L due to spatial limitations of S_R .

The experimental results are divided in many sub-sections. First, we mention the typical electron parameters (charge, divergence and spectrum) shooting at full intensity. In sub-sec.(4.3.2), we exploit the nano-nature of target in the electron emission process by scanning the input laser intensity and gain further knowledge of the acceleration process by analyzing the emission angles and finally in sub-sec.(4.3.3), we study the emission dependence on the phase of the optical field, i.e. CEP.

4.3 RANP experimental results

4.3.1 Electron emission from a nano-target

First of all, we need to mention that this is a single-shot experiment and each needle had to be replaced by a fresh one after each shot. The single-shot nature of the experiment relies absolutely on the shot-to-shot stability of the laser intensity due to wavefront aberrations, about 10%. Once

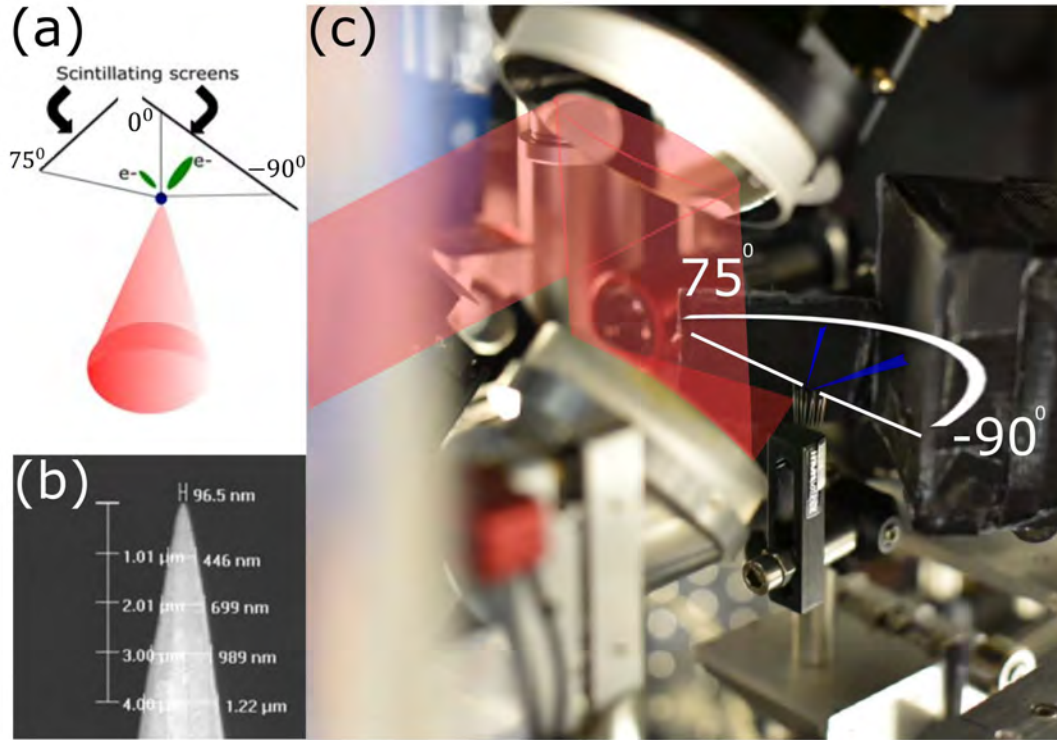


Figure 4.10: (a) Sketch of the top-view of the setup. (b) Electron microscope image of the Tungsten needle (Courtesy of AFM Bruker probes). (c) Experimental setup for RANP using the LWS-20 pulses. The laser beam is focused by a $F\#1$ 90° off-axis parabolic mirror to Tungsten nano-needle. 2.5 cm away the interaction, the angular distribution of the accelerated electron beams are analyzed on the scintillating screens, covered by $\approx 100 \mu\text{m}$ Al foil.

said this, we start with the experimental results before starting the discussion and comment the PIC simulations.

About 160 pC highly divergent (≈ 100 's mrad) beams are observed under irradiation of p-polarized pulses at $I_0 \approx 6 \times 10^{19} \text{ Wcm}^{-2}$ in the laser polarization plane in the forward direction at $\theta_{Left,Right} = \pm 25^\circ$. Fig.(4.12) shows the average of all shots measured with S_L and S_R . Furthermore, similar divergent few-pC electron bunches are observed on S_T as seen in Fig.(4.13). Since the experimental setup was very compact, the electron spectrum could not be measured in the needle-axis direction but only in the forward direction. As explained in the introduction in sub-sec.4.1.1, laser-solid interaction is highly polarization dependent. Furthermore, due to the sub-wavelength dimensionality of the target, we suspected the origin of the forward electrons to be related to surface plasmons excitation and laser absorption at the surface. We thus decided to study the process as a function of the laser polarization, since both of these mechanisms are polarization and target geometry dependent.

Although the absorption of the laser energy was not measured, we observed a gigantic quench in the electron emission when shooting with s-polarization, indicating a dramatic reduction in

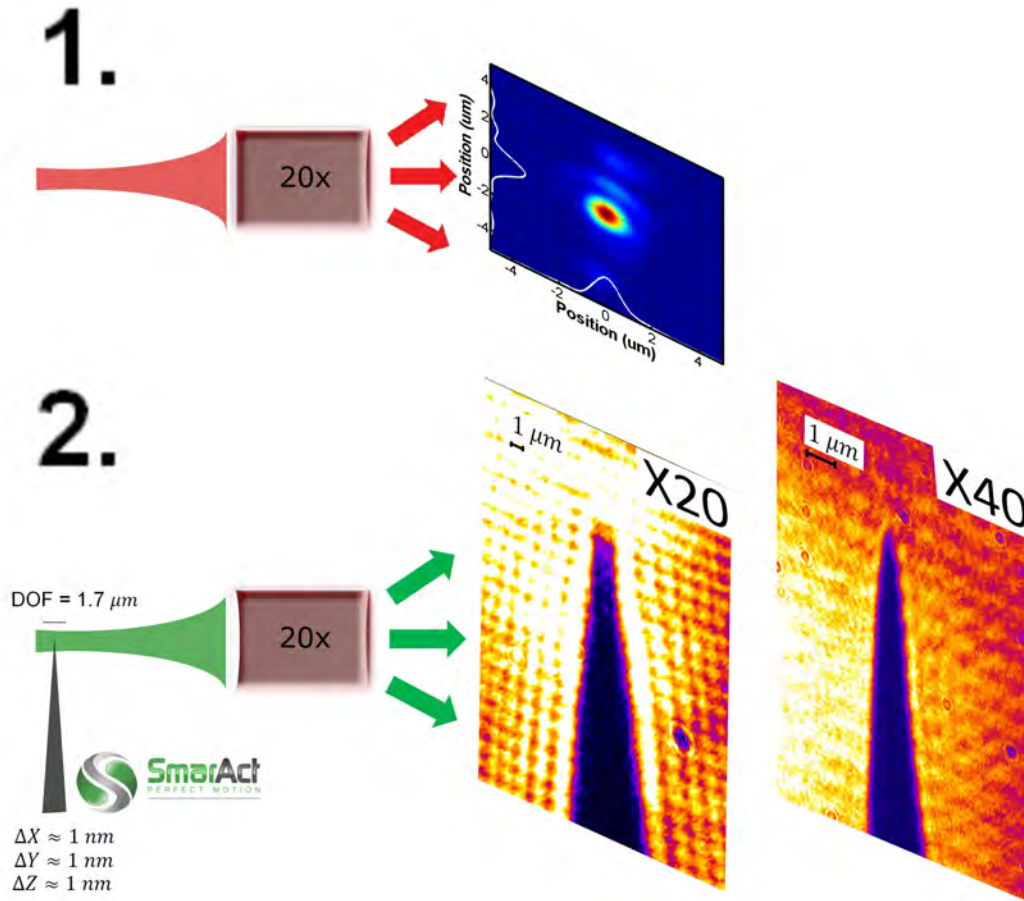


Figure 4.11: Alignment of each target. First step: scan the long-working distance objective position until the laser spot position is at its minimum size (image plane), then proceed to mark the laser spot (maximum) position. Second step: keeping the objective's position fixed and the laser blocked, the target is positioned with 1 nm accuracy to match the marked laser position vertically and horizontally. Finally, the longitudinal axis is scanned and the needle position is set equidistant to the positions z_1 and z_2 , where the image becomes blurry (out of focal plane).

the laser absorption. Approximately one order of magnitude less emitted charge (in forward and needle direction) is measured when the laser is polarized along the needle axis. Fig.(4.15) shows the raw data for p (top) and s (bottom) polarization.

Before proceeding with further scans to understand the origin of the electron emission, let us review the electron spectrum, shown in Fig.(4.14). While many groups require extreme enhanced near-fields to obtain keV level [71], laser intensities of $\approx 10^{20} \text{ Wcm}^{-2}$ already triggers the MeV range, i.e. $\approx 99\%c$. Thus, the relativistic term is immediately inherited from the laser parameters. In our case, a high-energy cut-off of about 7-9 MeV was measured, well beyond the laser

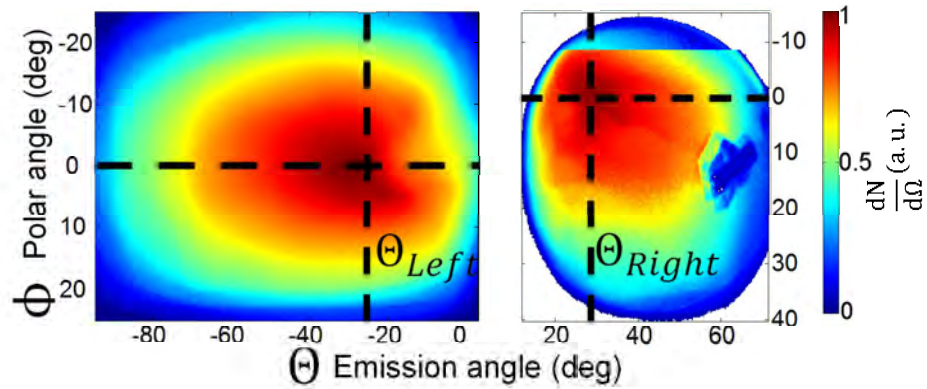


Figure 4.12: Average electron angular distribution of all shots from nanometer needles at maximum intensity.

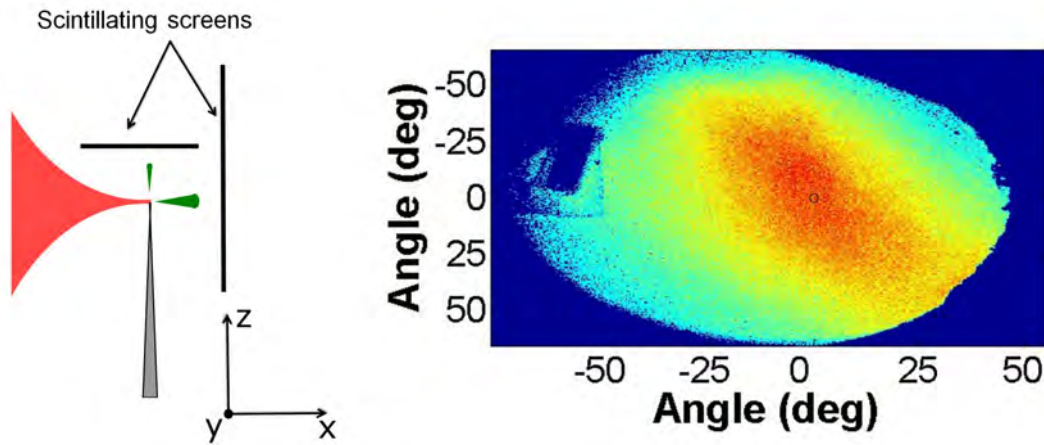


Figure 4.13: Left: Sketch of the experimental setup from a lateral perspective. Right: Typical shot with about 9 pC recorded at 90° polar angle on the top screen, in the needle axis direction.

ponderomotive potential W given by Eq.(2.11).

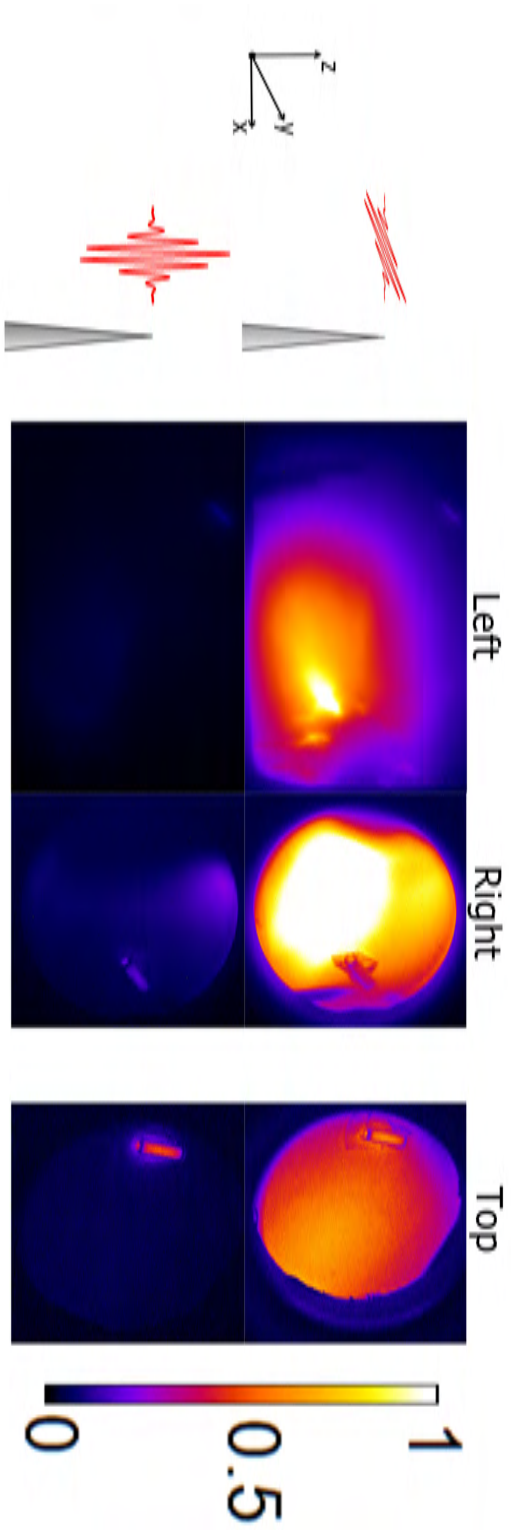


Figure 4.15: Top: Electron emission shooting with p-polarized light. Bottom: Electron emission shooting with s-polarized light. The images correspond from left to right to S_L , S_R and S_T , respectively. The color scale had to be adjusted in a way that on both cases emission becomes observable on the bottom, saturating thus the images on the top.

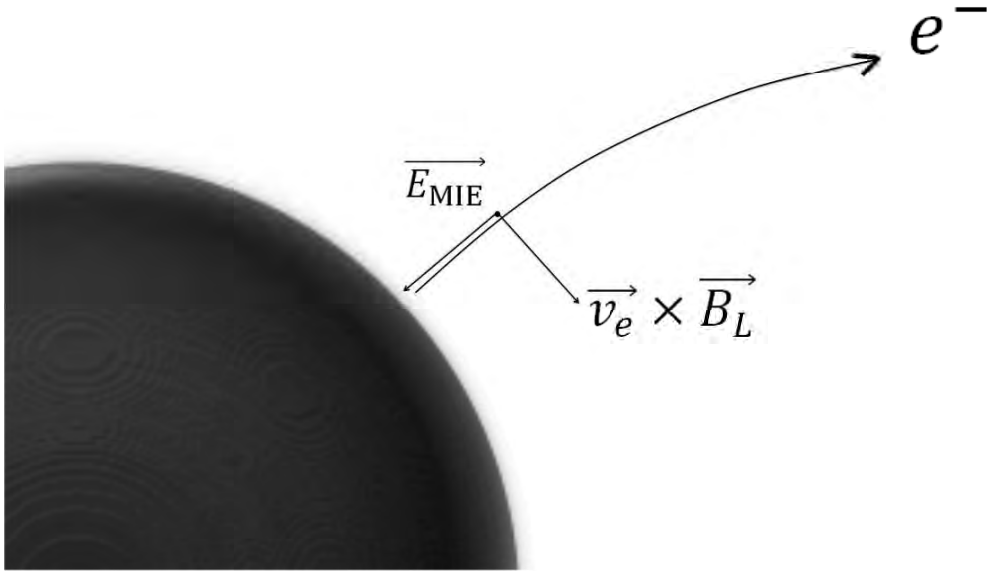


Figure 4.16: Forces acting on the electron during its ejection from the nanotarget into vacuum.

4.3.2 Intensity-dependent angular distribution

In this ultra-relativistic regime, the final emission angle is expected to be governed by the laser intensity [36], given by Eq.(2.20), rather than by the Mie angle which mainly depends on the size of the target. Therefore, at low intensities the scattering angle $\theta_{Left,Right}$ is expected to shift towards $\pm 90^\circ$, as classically predicted and demonstrated. Indeed, as shown in Fig.(4.19), by chirping the laser pulses and reducing the laser intensity by means of the DAZZLER, intensities almost 10^3 lower were reached and the full Mie regime is recovered.

Fig.(4.18) shows the measured emitted charge as a function of the laser intensity as well as previous results done at $> 10^6$ lower intensities [142]. Fig.(4.17) indicates experimentally the Mie-induced origin of the electron emission, since at low intensities, the emission occurs mainly at $\pm 70^\circ$, similar to previous reports[142]. Due to a combination of: slight inaccuracy ($\ll \sigma_{FWHM}$) of the vertical needle alignment, plasma expansion, target needle-like geometry and the spatial extension of the laser focal spot; the real target size during the interaction is not known. Yet, our results match the theoretical Mie angle of a $100 \text{ nm} < R_{\text{eff}} < 200 \text{ nm}$ radius target. The laser contrast proved to be extremely good, even though it is 10^7 at 5 ps using XPW. Most high-energy laser systems reach this intensity contrast about many 10's ps before the main pulse. Once again, we witness the uniqueness of OPCPA technology.

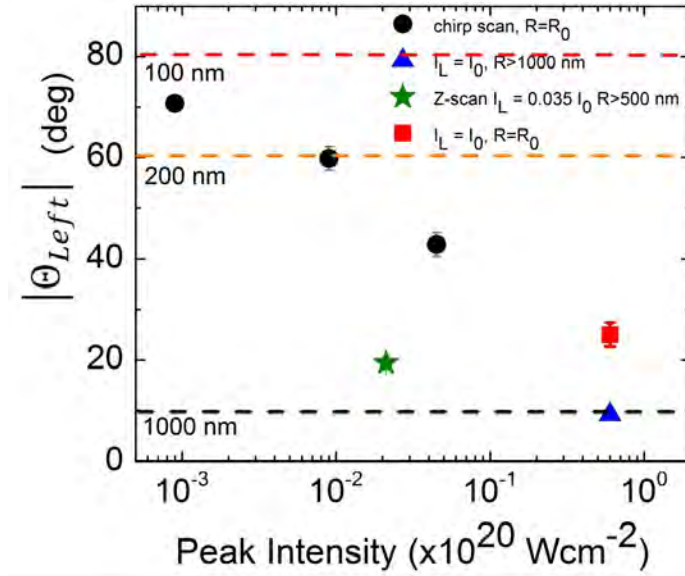


Figure 4.17: Emission angle measured on S_L as a function of the intensity $I_0 \approx 6 \times 10^{19} \text{ Wcm}^{-2}$. Particular cases, involving larger targets $R > 500 \text{ nm}$ or $R > 1000 \text{ nm}$, are plotted differently. Dashed lines correspond to the classical Mie angles for different radii.

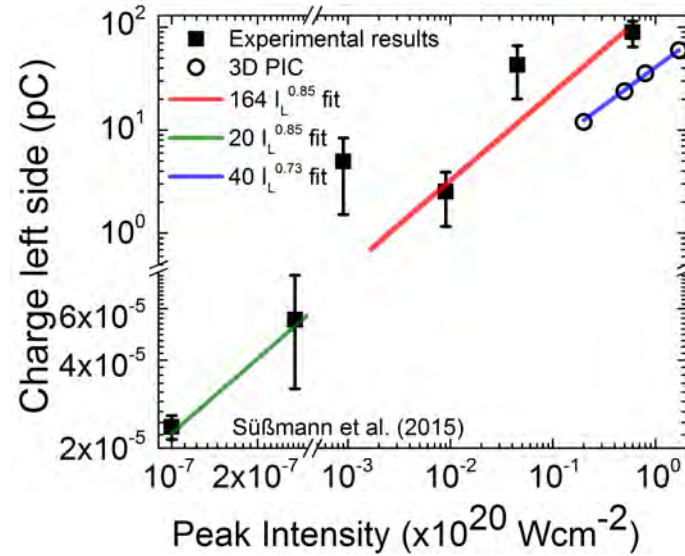


Figure 4.18: Measured charge on S_L as a function of the laser peak intensity.

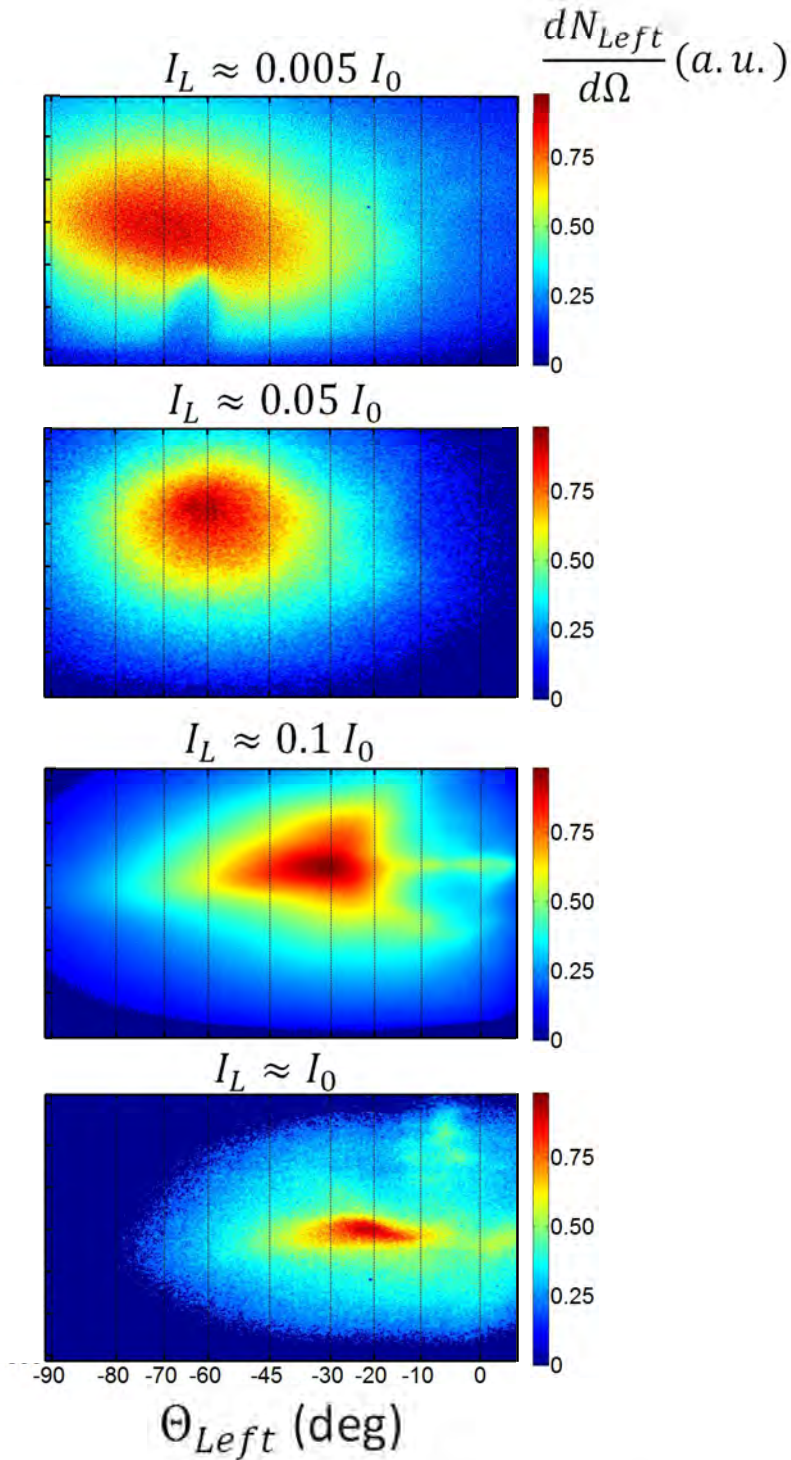


Figure 4.19: Typical shots for different peak intensities. At the lowest intensities, the electron emission occurs at the Mie angle $\theta_{Left} \approx -70^\circ$, whereas the electron bunch are bended forward, to about -20° at the highest intensity.

We focus on the total resulting ejected charge as a function of the laser peak intensity, as shown in Fig.(4.18). As introduced in sub-sec.4.1.3, the charge extracted from the target surface scales as $N \propto E_L \delta_p \propto I_L^{0.5}$ according to [2]. Yet, from sub-sec.2.3.2, at $a_0 \gg 1$, $\delta_p \rightarrow \delta_p \sqrt{a_0}$ due to relativistic corrections, which would lead to $N \propto I^{0.75}$, in agreement with the experimental observations, $\propto I^{0.85 \pm 0.18}$. Moreover, Fig.4.18 puts our results in perspective with respect to other reported experiments using few-cycle lasers and isolated nanoparticles, which matched the measured empirical intensity scaling, up to a pre-factor. In this way, the electron source presented in this work has much larger yield, $N \approx 10^9$ than reported so far.

Finally, the target size was scanned in two different ways: (i) Z-scan and (ii) focusing to a larger portion of the needle ($R \approx 10R_0$). By placing the needle out of the focal plane of the laser pulse, the spatially expanded waveform interacts with a larger portion of the target ($R \approx 6R_0$) at a lower intensity $I_L \approx 1 \times 10^{18} \text{ Wcm}^{-2}$, determined by the pulse divergence. In both cases, the interaction with a larger target resulted in a more forward-directed electron emission: $|\theta_{\text{Left}}(R_1)| > |\theta_{\text{Left}}(R_2)|$, for $R_1 < R_2$, regardless of the laser intensity, as observed in Fig.(4.17). In this way, some characteristic features of the Mie theory are still observable.

4.3.3 CEP effects observed

Near-single cycle laser pulses, in this case 1.8 cycles, exhibit a large field contrast among the different half-cycles within the temporal FWHM. The relative amplitude of each half-cycle is a sensitive function of the CEP (ϕ_{CEP}) as discussed in sub-sec.4.1.3. Moreover, the measured electron angular distribution showed a clear electron yield asymmetry for $\varphi_{\text{CEP}}(A_N = +0.15) \approx 0.85\pi$ and for $\varphi_{\text{CEP}}(A_N = -0.15) \approx 1.85\pi$, whereas a complex and more symmetric emission appeared for intermediate phases. Although the electron energy was not phase-tagged and was measured only on one side due to the compactness of the experimental setup, we can so far state that the whole electron angular distribution could be controllable by the phase of the laser pulse. The phase determination uncertainty corresponds to $\Delta_{\text{CEPmeter}} \approx 280$ mrad from the single-shot phasemeter. Gouy-phase shift from shot to shot, as mentioned above, was below this value ≈ 170 mrad. Thus, $\Delta_{\text{CEP}} = \sqrt{\Delta_{\text{CEPmeter}}^2 + \Delta_{\text{Gouy}}^2} = 330$ mrad. In any case, we expect significant changes in any phase-dependent observable at $\pi/2 = 1.57$ rad intervals, i.e. cosine and sine pulses. Indeed, we studied the electron yield $N_e = N_e(\phi_{\text{CEP}})$ and the electron scattering angle $\theta_{\text{Left}} = \theta_{\text{Left}}(\phi_{\text{CEP}})$, for almost 50 CEP-tagged shots. The asymmetry parameter A_N studied in this work is :

$$A_N(\phi_{\text{CEP}}) = \frac{N_{e,L}(\phi_{\text{CEP}}) - N_{e,R}(\phi_{\text{CEP}})}{N_{e,L}(\phi_{\text{CEP}}) + N_{e,R}(\phi_{\text{CEP}})} \quad (4.25)$$

where $N_{e,i}$ equals:

$$N_{e,i} = \int S_i d\Omega \quad i = L, R. \quad (4.26)$$

integrating S_L (S_R) over the angles -75° to -15° (15° to 75°) and over the same area on each screen. Fig.(4.20) shows the asymmetry parameter A_N , while Fig.(4.22) shows the electron emission angle θ_{Left} as a function of the laser's CEP. The asymmetry parameter oscillates sinusoidally with 2π periodicity, reaching a maximum amplitude of $|A_N| \approx 0.15$. This result is empirically well supported by the measured intensity scaling. Assuming an escape energy of about 50% $U_p \approx 1$

MeV [36], integration over the instantaneous intensity of a 4.5 fs laser pulse for left and right directions above a certain threshold as done in Fig.(4.6): $\int_{-\infty}^{\infty} (E_L(t)^2)^{0.85} (|E_L(t)| > \sqrt{0.5}E_0) dt$ yields a 15% asymmetry, in agreement with the measured data. Furthermore, the direction of the electron beam θ_{Left} was found to oscillate about $\pm 7^\circ$ around its mean value as a function of φ_{CEP} with a 2π -periodicity as well. In particular, a correlation between $A_N(\varphi_{CEP})$ and $|\theta_{Left}(\varphi_{CEP})|$ was recognized, within error bars, as shown in Fig.(4.20) and Fig.(4.22). The bunches with higher electron yield deviate even further from the laser axis and viceversa. In this way, Θ_{Left} deviated the furthest, to $\max(|\theta_{Left}|) \approx 32^\circ$, for the maximum positive asymmetry, $A_N = +0.15$ ($N_{e,L} \approx 1.35N_{e,R}$).

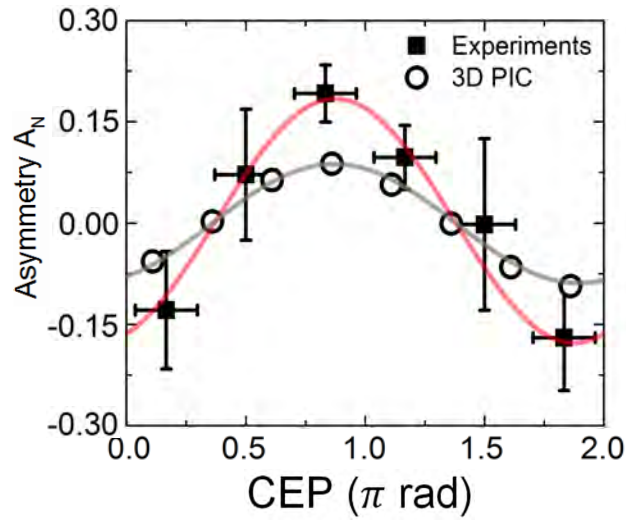


Figure 4.20: Measured and simulated asymmetry parameter A_N as a function of the CEP.

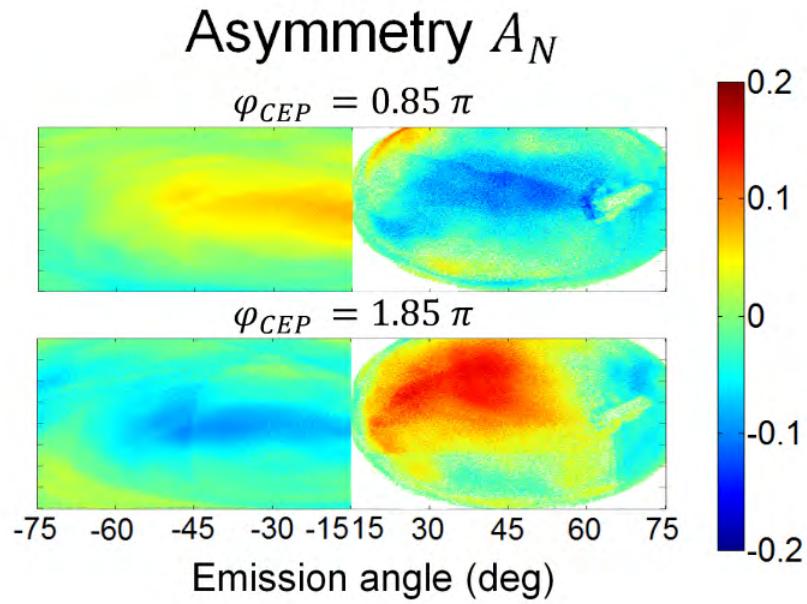


Figure 4.21: Electron angular distribution (average-subtracted) for $\varphi_{CEP} = 0.85\pi$ and $\varphi_{CEP} = 1.85\pi$.

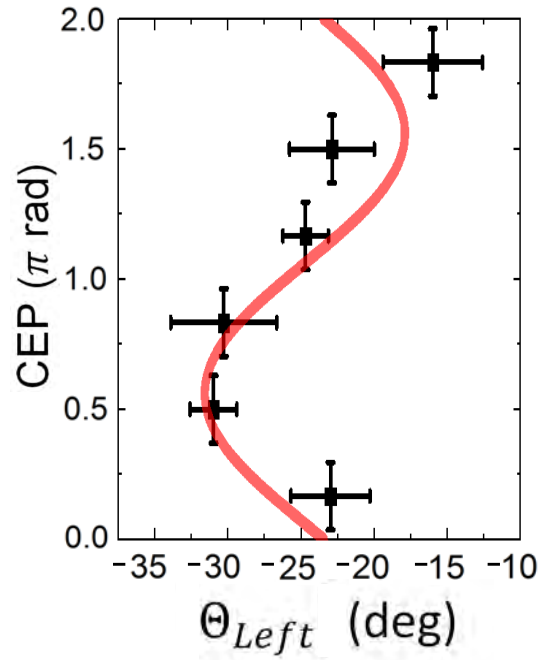


Figure 4.22: Measured emission angle θ_{Left} on S_L as a function of the CEP.

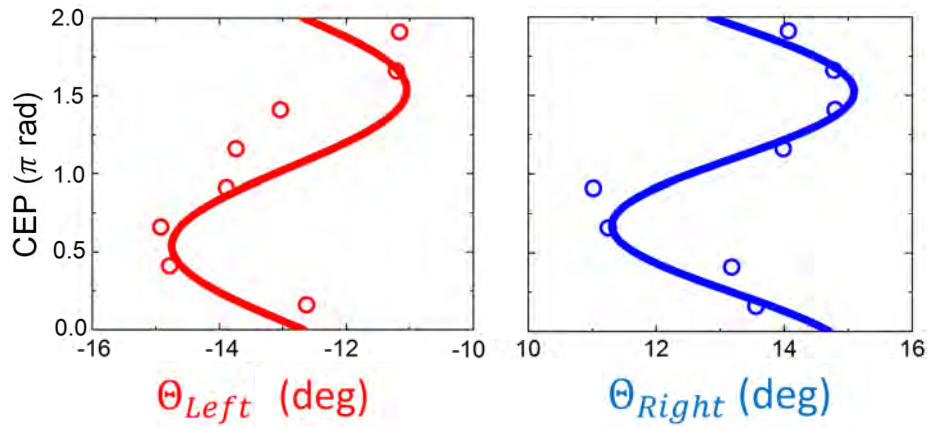


Figure 4.23: Simulated θ_{Left} and θ_{Right} emission angle as a function of the CEP.

4.3.4 Discussion

The intervention of localized surface plasmons in the acceleration process was first hinted in the polarization sensitivity results shown in Fig.(4.15). Any type of plasma wave generation at the surface via an oscillatory charge separation under the laser field, as sketched in Fig.(4.1), is hindered due to the geometry of the target for a s-polarized pulse, as no oscillatory charge migration can take place. Moreover, due to the shortness of the plasma-scale length, resonance absorption will also not take place significantly. The whole vacuum heating process is also hindered due to the high intensities, causing no back-acceleration into the target and thus significant less absorption. Yet, in terms of electron emission, a small sheath may escape and be further accelerated in a $\vec{v} \times \vec{B}$ fashion.

The underlying physics describing the transition between the Mie regime and the intensity-dependent scenario is not clear. For instance, the maximum obtainable energy is unclear and depends highly on the complete acceleration mechanism. One may think directly of VLA at the focus as studied in [40], though. Yet, some process is missing, in analogy to LWFA, which is responsible for injecting efficiently a fast electron (> 1 MeV) into vacuum and into the laser field, otherwise the net energy gain is very low, as explained in sub-sec.2.2. We can state that there "must" be an extra step within the acceleration since the electron energy is well beyond the capabilities of the laser. The suspicion of another mechanism, i.e. excitation of SPs on the target surface, playing the "injection" role is thus more evident.

As theoretically expected and explained in sub-sec.4.1.1, the enhanced electric field of the SP is, though higher than the incoming electric field, very localized at a certain angle in the laser polarization plane, see Fig.(4.2) and Fig.(4.3). Yet, the magnitude of the enhancement factor is hardly recognizable from the experimental results. Secondly, the smaller the target, the more this angle shifts towards $\pm 90^\circ$ from the laser direction. This physical picture corresponds to the Mie theory only and the overall electron emission is expected to occur at the corresponding Mie angles[142] at low intensities. Yet, in our case the electron bunches were emitted in the forward direction, $\theta_{Left,Right} \approx \pm 25^\circ$ off-axis (see Fig.(4.17)). Here, the Mie plasmons are not the only "accelerators", since at high intensities, where $v_e \approx c$, the cB_L field is as strong as E_L , as seen in Fig.4.16. In this way, the electron propagation angle is expected to deviate significantly from the Mie angles.

A two-step mechanism

So, the acceleration mechanism as well as the enhancement factor are difficult to estimate. The energy contribution from the Mie plasmon and the laser post-acceleration in vacuum up to $\approx Z_R$ [40], is unclear. As usual laser-plasma physicists turn to PIC simulations to understand better the process. Throughout the exhibition of the experimental results, we have speculated the possible appearance of Mie plasmons on the surface which eject hot electrons very efficiently into vacuum, referred to as 1st step illustrated in Fig.(4.24), and a second step where the laser field itself accelerates them further (2nd step shown in Fig.(4.28)). The participation of such plasmons seems irrefutable since the electron cut-off energy exceeds the laser capabilities.

PIC simulations were performed using a 100 times overcritical hemisphere of 200 nm radius. The applied laser intensity was 5×10^{19} Wcm⁻², 4.5 fs FWHM pulse duration and 1.2 μ m focal

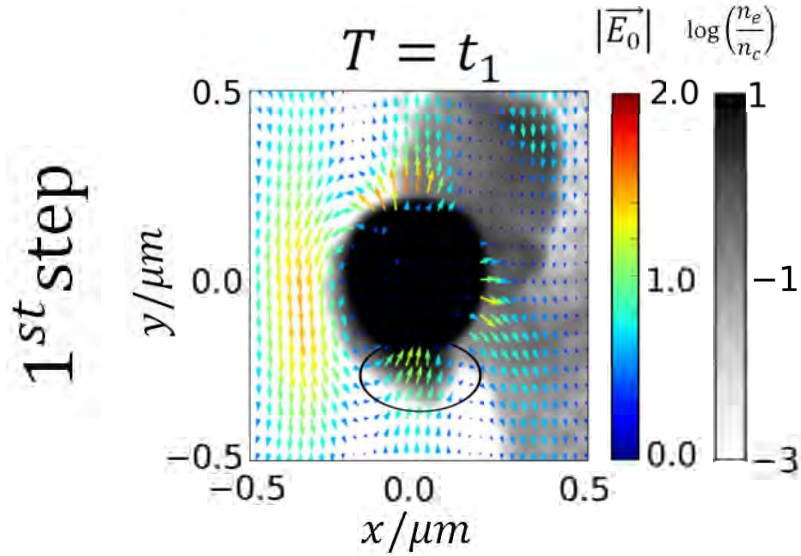


Figure 4.24: First step: the incident laser light is coupled to the plasmonic enhanced near field at the target surface. At $T = t_1$, the probed bunch (marked with a black ellipse) is rapidly extracted and pushed out of the target by the surface field at about 90° off the laser axis.

FWHM spot size. The 3D box consisted of $12 \times 12 \times 8 \mu\text{m}^{-3}$ divided in $768 \times 1024 \times 512$ grid points and 68×10^6 macroparticles. Moreover, as shown in Fig.(2.1), the ionization degree is about W^{+50} before the main peak arrives and only an extra $\approx 15\%$ during the pulse. Thus, all our results can be fully described assuming an initially ionized target. On the other side, inner-shells tunnel-born electrons at the surface will follow Eq.(4.22), as illustrated in Fig.(4.4). Yet, the fraction of TU-ionized electrons does not hinder the final result at all, as it will be shown later.

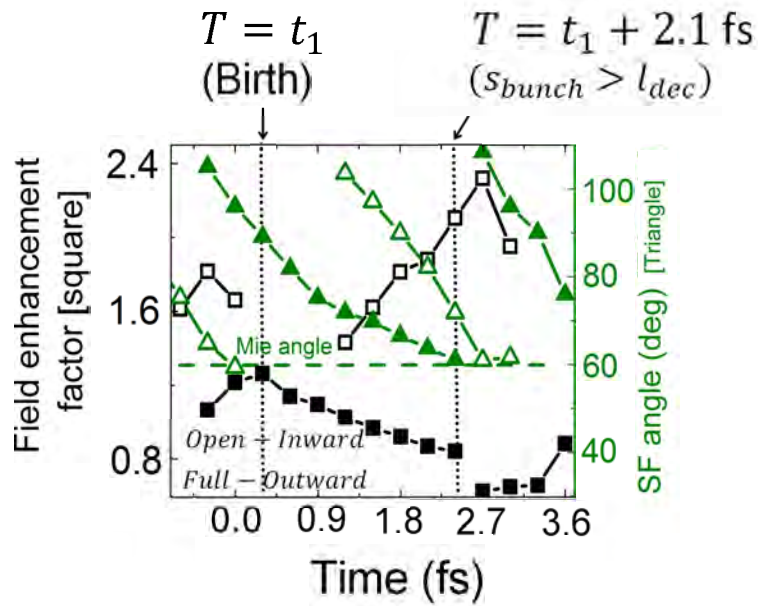


Figure 4.25: Surface field dynamics; strength and directionality, for the inward (open) and outward (full) accelerating field for electrons as a function of time.

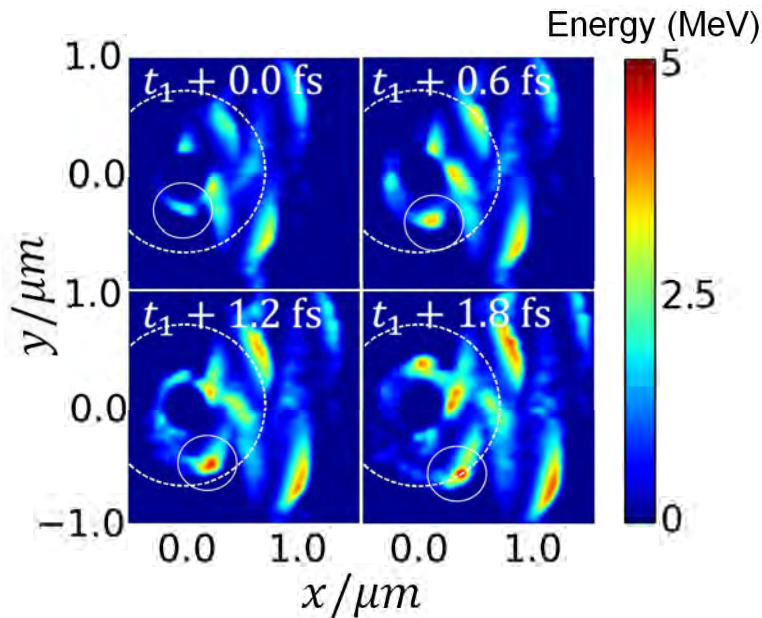


Figure 4.26: Energy evolution in real space: After a rapid (300 as) injection into vacuum, the bunch (marked with a white continuous circle) possesses a kinetic energy of 2.5 MeV and is further pushed by the plasmonic field until $T = t_1 + 1.8$ fs, when it reaches the plasmon decay length, $l_{dec} = 0.55 \mu\text{m}$ (dashed line)

By analyzing the simulated electron spectral evolution of a particular bunch, access and distinctions of each step is possible. Fig.(4.24) indicates the birth moment of an electron bunch (continuous line) at $T = t_1$, as well as the surface field (SF) dynamics at this instant. During the excitation of the plasmonic field by the incident laser light, the localized enhanced near field ($\approx 1.25E_0$) strongly pushes the plasma electrons of a $\delta_p\sqrt{a_0}$ thick slab outwards at about 90° , where the laser field is normal to the surface of the target. The emission time interval is limited to the SF's temporal-window, about 300 as. This scenario is mirrored on the semiplane $y > 0$ after each laser half-a-cycle, as described also in previous studies [91]. The complete dynamics of the SF during the first step is thoroughly analyzed in Fig.(4.25). This figure shows the SF's enhancement factor as well as its directionality as a function of time for the semiplane $y < 0$, whereas Fig.(4.26) shows the electron energy evolution in real space. The SF pushing the electrons inwards (empty) and pulling outwards (filled), vary their orientation from 100° beyond 60° as the laser pulse, and so a given half-cycle maximum, passes through the target. While the inwards-SF will reach its maximum of $\approx 2.3E_0$ at the Mie angle (60°) a cycle later, the amplitude of the outward-scattering SF is reduced due to the density gradient induced by the newly born bunch leaving the target. Although its directionality converges finally towards 60° as well, its maximum is reached at $T = t_1$, defining the emission time. Moreover, as indicated in these both figures, the tracked electron bunch reaches a distance from the target surface of $s_{bunch} \approx l_{dec}$, i.e. the SF decay length, right before the inward accelerating field, hindering the back-acceleration towards the target, resembling the sub-cycle emission represented in Fig.(4.5).

After surpassing the target's electro-static potential, (3 MeV at $s_{bunch} = 100$ nm from the target surface, corresponding to 300 nm from its center), the pre-accelerated electron bunch will not return to the surface[112], as depicted in Fig.(4.26). At this same instant, the inwards scattered electrons gain more energy than the directly-emitted ones due to the larger enhancement factor for $y > 0$. Yet, these electrons emerge with a quarter-cycle time-delay at almost 0° along the laser axis and suffer a strong deceleration after $1 \mu\text{m}$. The directly-emitted bunch surfs the plasmonic field (9 TV m^{-1}) until $l_{dec} \approx 550$ nm (dashed circumference), gaining a maximum energy of 5 MeV at $T = t_1 + 1.8$ fs. The propagation angle of these electrons, plotted in Fig.(4.27), resembles the SF's, as long as the bunch's position is within a l_{dec} radius, i.e. $s_{bunch} < l_{dec}$. In the vicinity $s_{bunch} \approx l_{dec}$, the first step comes to an end. Hence, the plasmonic field "passes the baton" to the laser field for subsequent acceleration in a second phase.

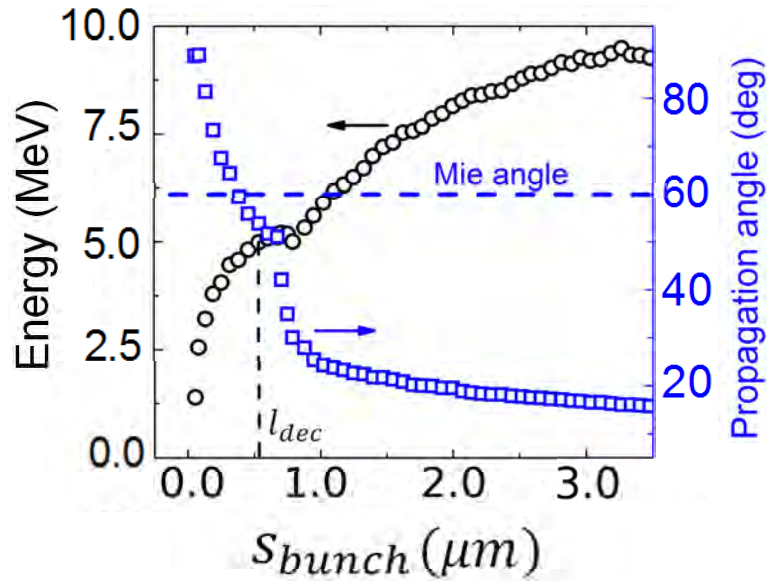


Figure 4.27: Energy and propagation angle evolution of the electrons as a function of the bunch distance from the target surface s_{bunch}

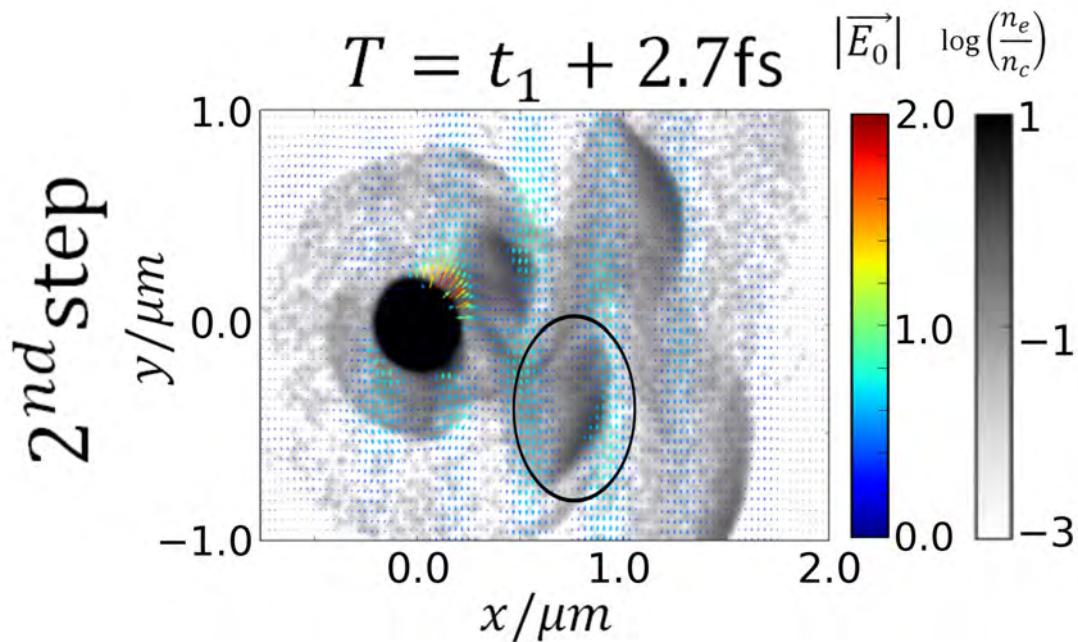


Figure 4.28: Second step: At $T = t_1 + 2.7$ fs, the monitored overdense electron bunch is being driven ponderomotively in forward direction by the laser. Sitting between two transverse field maxima, it fulfills the required conditions to get accelerated and gain even more energy from the traveling laser wave.

Fig.(4.27) indicates the rest of the mechanism for $s_{bunch} > l_{dec}$. At a later instant, $T = t_1 + 2.7$ fs and shown in Fig.(4.28), the overdense bunch sits between two transverse laser field maxima[150, 147]. Correctly injected, the bunch proceeds to Step 2: post-acceleration in the laser field. An electron bunch traveling with $0.99c$ is phase-synchronized and can actually gain monotonically more energy in the travelling wave[2] with a field strength of $\approx 3.6 \text{ TVm}^{-1}$, as deduced from the start of the second step in Fig.(4.27). Hence, the beam “surfs” then the laser wavefront along its propagation axis acquiring more energy and deviates strongly from the original Mie angle. At $s_{bunch} \approx Z_R$, the gained energy is about 5 MeV as shown in Fig.(4.29) at $T = t_1 + 14.4$ fs, in agreement with $\Delta E_{VLA} \approx 5$ MeV from Eq.(2.18). In the simulations the final energy is almost 10 MeV, in good agreement with experimental observations in Fig.(4.14). Reaching the VLA regime is a direct consequence of the sub-cycle relativistic injection and the tight focusing. The magnitude of the overall acceleration field is experimentally supported by the total energy gain and the focusing conditions: $\Delta E/Z_R \approx 9 \text{ MeV}/4.8 \mu\text{m} \approx 2 \text{ TVm}^{-1}$. Further PIC simulations at different peak laser intensities confirm these results; whereas the first step final energy scales as $a_0 l_{dec} \propto \sqrt{a_0}$, the post acceleration scales with a_0 , similar to previous studies[2], and shown in Fig.(4.30). Although Eq.(2.18) predicts a quadratic scaling with respect to the driving field, the final scaling results rather linear due to the obliquely transverse injection.

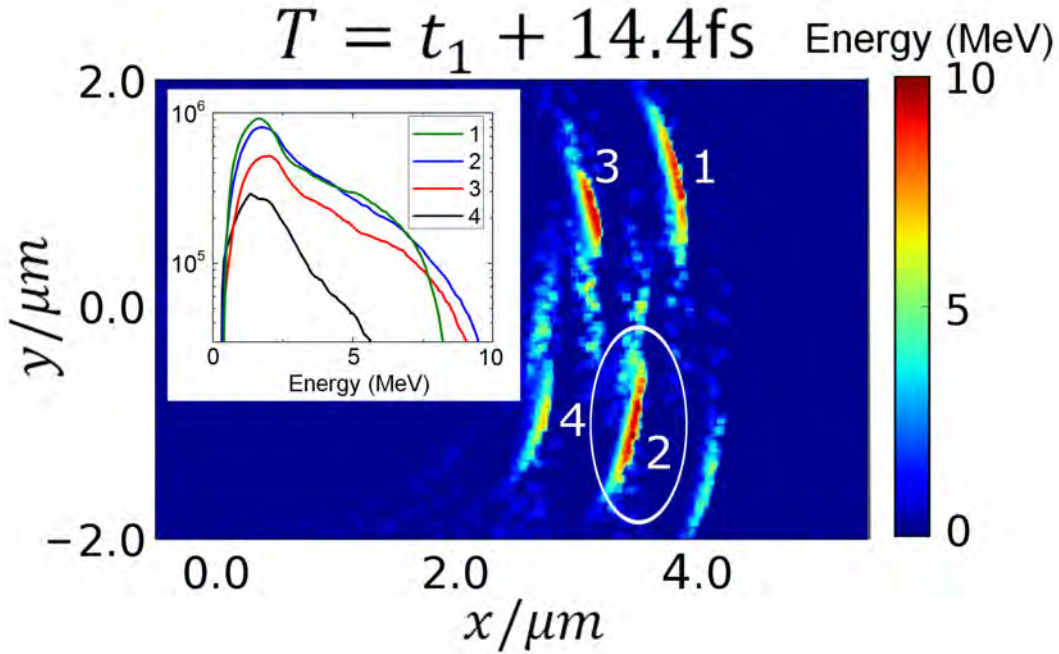


Figure 4.29: Almost at the end of the second step after approximately $\geq 3 - 4 \mu\text{m}$ of propagation, which corresponds to the simulated Rayleigh length ($4.4 \mu\text{m}$), at $T = t_1 + 14.4$ fs the electrons gained extra 5 MeV. $\varphi_{CEP} = 0.9\pi$.

The emission in the first step is intrinsically field dependent as shown in Fig.4.31. Since the

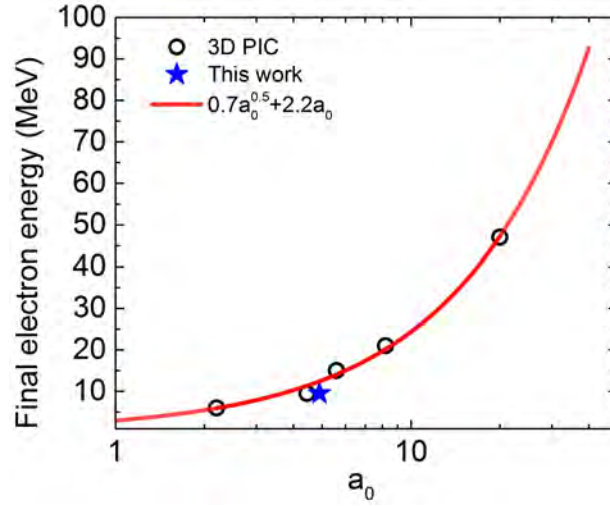


Figure 4.30: Simulated electron energy as a function of a_0 , assuming the same conditions in the RANP experiment.

driver has few cycles, the total emission results asymmetric for a cosine pulse and symmetric for a sine pulse. Indeed, as observed in Fig.(4.29), there is more charge emitted (bunches 1 and 3) on the semiplane $y > 0$. In the simulations, a charge asymmetry of 10% with a period of 2π is obtained, as shown in Fig.(4.20). Most importantly, this asymmetry allows the tracked bunch (labeled “2” now) to be isolated, via energy-filtering, as inherited from the attosecond science [84]. Moreover, the emitted bunches will not follow symmetric trajectories if the driver has only a few cycles because the field changes significantly from cycle to cycle. Another CEP-dependent degree to maneuver the synchronized direction of electron jets is also present along the VLA, as shown in Fig.(4.23). As expected in the ponderomotive scattering scheme[62, 97], the strongest half-cycle is expected to bend the electron bunch the closest to the laser axis, in agreement with the experimental observations, Fig.(4.22). Furthermore, these experimental observations, together with simulations, further prove our claims and support a steep plasma gradient ($\lambda_L/10$), since at a larger plasma scale-length, the electron propagation angle would mainly follow the laser propagation direction[127], decreasing the amplitude of this phase-induced steering effect.

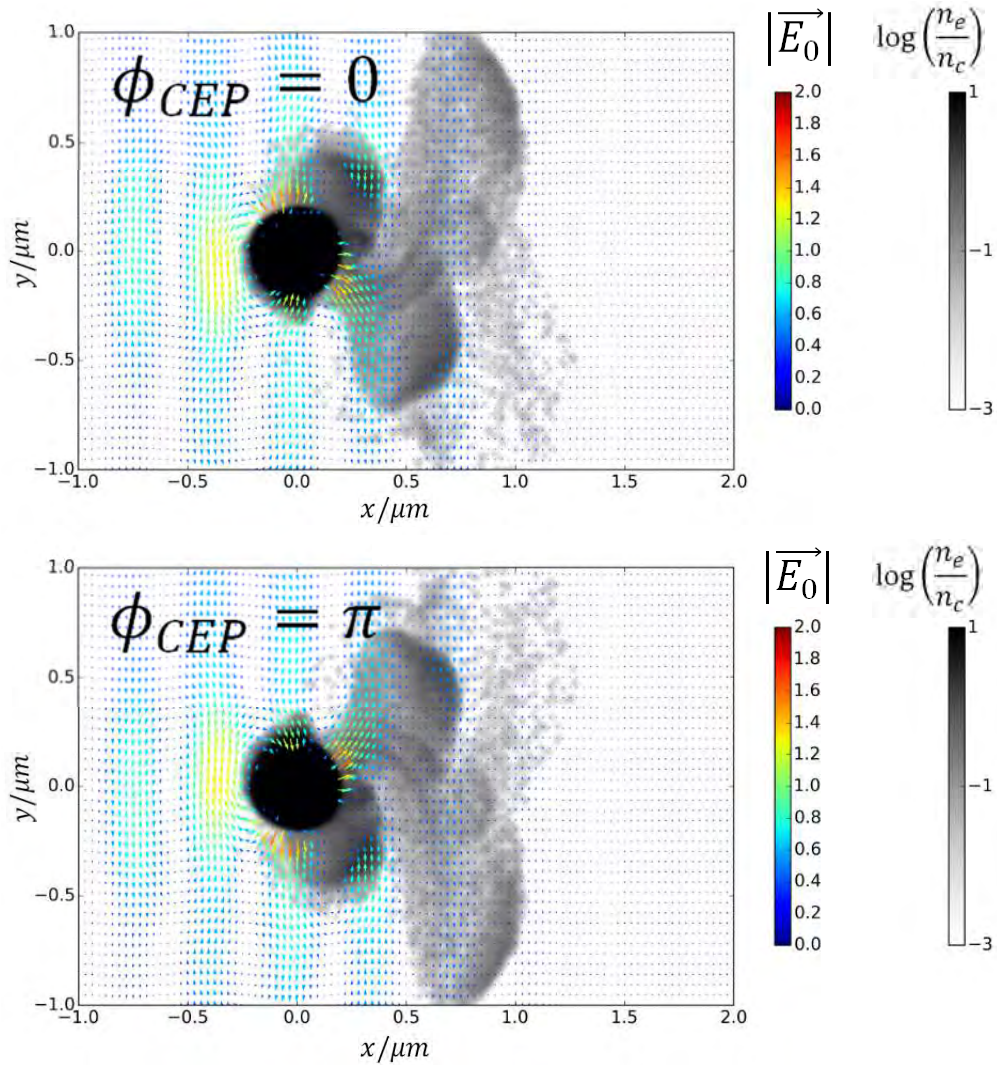


Figure 4.31: Top: Normalized electric vector field (colored) and the electron density distribution (gray and logarithmic scale). Bottom: Same case from top, but laser CEP is shifted by π . Both configurations were taken at the same simulation time-step.

In order to reproduce our results, we simulated the electron angular and spectral distribution for different CEP's: $0.4\pi, 0.9\pi, 1.4\pi, 1.9\pi$. See Fig.(4.33). A clear asymmetry (2D and 1D) is observed for phases $\varphi_{\text{CEP}} = 0.9\pi$ and $\varphi_{\text{CEP}} = 1.9\pi$. For intermediate phases, however, the integrated 1D profile (black line) remains symmetric yet the emission is rather complex and mixed. For each phase, the emission pattern reflects the sub-cycle regime dynamics. Overall charge asymmetry (see Fig.(4.20)) is easily explained by the shortness of the laser driver. Yet, the main advantage of simulations is its capability to isolate and resolve each bunch, as seen in Fig.(4.29), which allows us to explain all of our results exposed before in sub-sec.4.3.3. As also done for Fig.(4.21), Fig.(4.33) zooms into the details of the emission by subtracting the averaged angular distribution from each particular case, in order to enhance the asymmetry among the different phases. In this way, we are able to identify each bunch, as shown in Fig.(4.32).

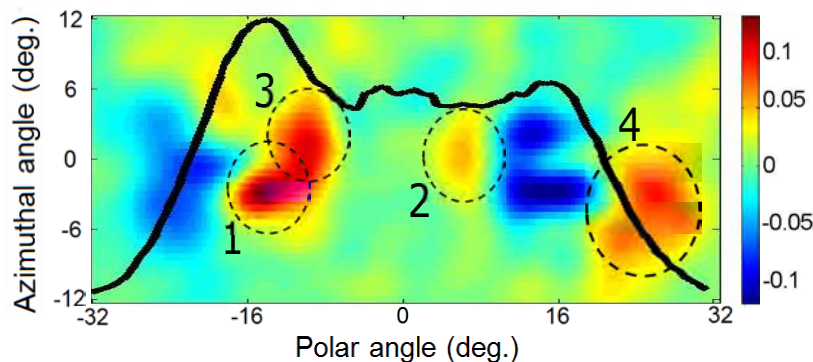


Figure 4.32: Simulated 2D asymmetry for $\varphi_{\text{CEP}} = 0.9\pi$, i.e. $I(\varphi_{\text{CEP}} = 0.9\pi) - \langle I \rangle$, where $\langle I \rangle$ is the averaged angular distribution. The electron bunch labeling corresponds to the same as in Fig.(4.29).

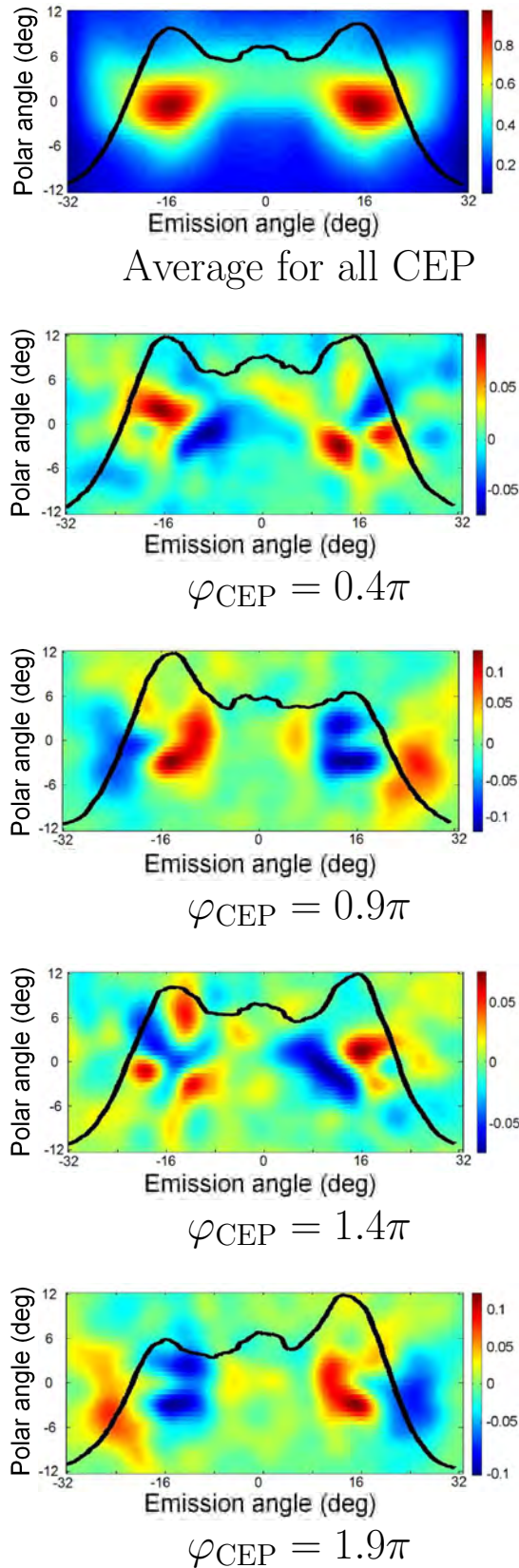


Figure 4.33: 2D asymmetry in angular distribution and 1D integrated distribution along the polar angle (black line) from 3D PIC simulations. Mind the different color bars.

Chapter 5

Conclusions and outlook

LPAs are slowly reaching maturity. The underlying physics is nowadays more and more understood, attributed in a large extent to the rich experimental feedback in these last years, including this work. For the purpose of producing the next generation of femtosecond and sub-femtosecond few-MeV electron sources, different types of laser-acceleration mechanisms have been studied and discussed in this thesis. Since relativistic laser-plasma interactions depend fundamentally in the electron density, they are mainly divided in underdense (gas) and overdense (solids). In particular, two important topics of LPAs were treated: (i) the phase-space evolution during the acceleration of the beam via controlled-injection in LWFA and (ii) emission of relativistic electrons from nanotargets. Throughout this thesis, some advantages and disadvantages of the different technologies have been already hinted, as well as the state-of-the-art.

5.1 The LWFA electron phase-space evolution

In chapter 3, a systematic and direct measurement of the dephasing effect in a laser wakefield accelerator has been performed utilizing shock-front injection and sub-10-fs laser pulses. For the final result, experimental data collected in the works of [130, 12] using the 8 fs LWS-20 version were included. Shock front provides stable and quasi-monoenergetic electron beams, even in very high dense plasmas where the dephasing lengths are 60-300 μm . The maximum obtainable electron energy is about 10 MeV for < 5 fs laser pulses as seen in Fig.(5.1), and 20 MeV for 8 fs. Shock-front injected beams occupy a smaller space in the phase-space and allowed the evolution of various electron parameters (peak energy, absolute energy spread, charge and divergence) during dephasing to be observed and monitored. Moreover, new effects such as the re-acceleration of the electron beam after dephasing or the improvement of the relative energy spread and divergence at the dephasing point have been identified due to the detailed measurement. Given the initial laser parameters in which the experiments were done, such as positive pre-chirping for the < 5 fs case, gave rise to a weakly LWFA scenario. Provided that nonlinearities were not significant, a simple model was able to describe the electron energy during dephasing. The study of the dephasing effect is of primary importance for bigger and longer accelerators, and our model provides a clearer understanding in order to guarantee the maximum performance of laser-plasma accelerators.

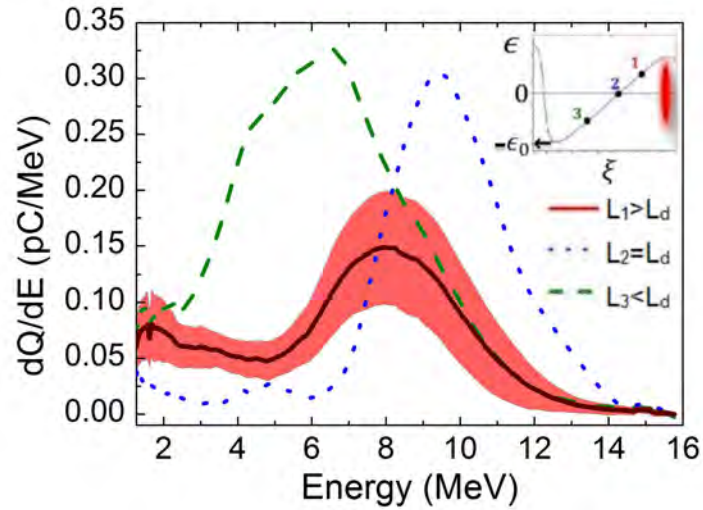


Figure 5.1: Studying the phase-space evolution with shock front. Plotted in the figure: the average electron spectrum with 8 MeV peak energy over 20 shots for (L_1) and the standard deviation band in shaded area, plus two typical single-shot electron spectra (for L_2 and L_3) with peak energies of 9 and 6 MeV, respectively, at $7.7 \times 10^{19} \text{ cm}^{-3}$ and < 5 -fs LWS-20 pulses. The measured dephasing length is $L_d \approx 130 \mu\text{m}$. Inset: Illustration of the longitudinal electric field of the plasma and position of the electrons in the co-moving frame inside the first plasma period at the time they leave the plasma. Electrons 1,2 and 3 have $L_1 = 180 \mu\text{m}$, $L_2 = 150 \mu\text{m}$ and $L_3 = 50 \mu\text{m}$ acceleration lengths, respectively.

5.2 CEP-dependent emission of relativistic electrons from nanotargets

In chapter 4, we studied thoroughly the electron emission of a nano-scale target in a very exotic regime using extremely intense ($6 \times 10^{19} \text{ Wcm}^{-2}$) sub-2 cycle driving laser pulses. Here, 0.1's nC electron bunches were measured at the forward direction, about $\pm 25^\circ$ off-laser axis, with a cut-off energy of 7-9 MeV. In this regime, as usual for relativistic scenarios, the laser intensity takes domain of the final electron parameters, in particular the electron angular distribution. Previous studies at 10^{13} Wcm^{-2} using isolated nanotargets reported only size-dependent angular distributions, insensitive to the applied laser intensity. By realizing an intensity scan down to 10^{17} Wcm^{-2} , we could explore the emission mechanism and recovered the classical Mie regime corresponding to a target with a radius $100 \text{ nm} < R_{\text{eff}} < 200 \text{ nm}$. Moreover, together with the support of simulations, two different acceleration mechanisms were identified. During the excitation of the plasmonic enhanced near-field, a electron slab of few nm thickness is strongly accelerated (9 TVm^{-1}) within a laser half-cycle up to 5 MeV over an acceleration length of 500 nm, i.e. the plasmon decay length. This injection into vacuum repeats itself every laser half-cycle,

alternating at each time the emission side. Since the plasmonic field follows instantaneously the incident laser field, the electron emission is expected to be a sensitive function of the CEP for sub-2 cycle pulses. Indeed, a maximum emitted charge asymmetry of 15% in the laser polarization plane was measured as seen in Fig.(5.2). In a correlated manner, the electron propagation angle oscillated with an amplitude of almost 10^0 . Only such a sub-cycle injection of a relativistic electron bunch permits its subsequent acceleration in the laser field in vacuum where they are further pushed at few TVm^{-1} until the Rayleigh length, reaching a maximum energy of 9 MeV. The CEP effects observed in this experiment could be extrapolated to secondary sources, such as X-rays generated via High-Harmonic Generation at relativistic intensities[151].

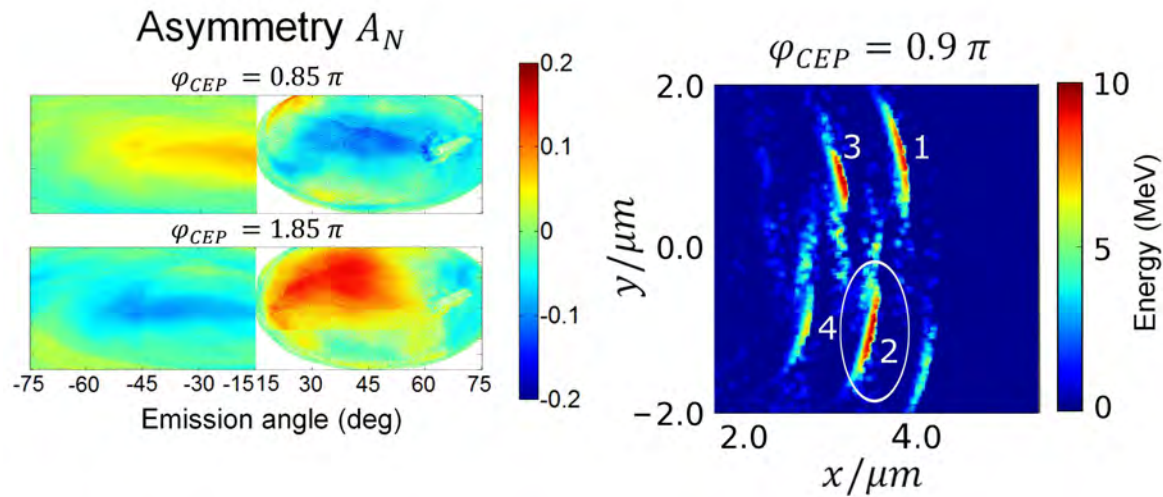


Figure 5.2: **Left:** Electron angular distribution as a function of the CEP, shown in in sub-sec.4.3.3 in Chapter 4. **Right:** Simulated vacuum acceleration of attosecond relativistic electrons emitted from a nanotarget at $5 \times 10^{19} \text{Wcm}^{-2}$. Due to the shortness of our the LWS-20 pulses, the emission is mainly compound of three electron bunches (1-3) in the laser polarization plane. In this case, the bunch “2” can be isolated via energy-filtering.

Furthermore, whereas nJ-class lasers rely entirely on the large enhancement factors nanotargets provide, in this case, the plasmonic field is only the co-protagonist and acts as an efficient electron photo-injector. VLA technology yields much larger accelerating fields and future PW laser systems should reach 100TVm^{-1} record values and GeV energies, following the scaling extracted from PIC simulations in Fig.(4.30). Large electron yield ($\approx \text{nC}$) will be automatically fulfilled by employing such powerful intense lasers on isolated nanotargets. The versatility and applicability of these sources will be given by the strong dependence of the electronic response on the driver’s optical field. By unifying concepts of the attosecond science (CEP dependence) and the relativistic-plasma physics ($a_0 \gg 1$), this experiment paves the way to the next generation of electron pulses, as simulations indicate the capability to isolate, via energy filtering, a relativistic attosecond electron bunch as highlighted in Fig.(5.2).

5.3 Looking towards the future

LPA technology was not born alone and will not continue evolving on its own. Laser technology and LPAs future are almost bound to each other. One motivates the other to grow together. In the near future, Petawatt and Exawatt lasers will catapult nonlinear relativistic optics and even nuclear photonics. Extremely high-intensity level 10^{26} Wcm^{-2} ($a_0 \approx 6000$) in the coming decade will be available, much beyond the current intensity regime 10^{21} Wcm^{-2} ($a_0 = 20$). Such extreme lasers could accelerate particles to frontiers of high energy of TeV and become a tool of fundamental physics involving particle physics, gravitational physics, nonlinear field theory, ultrahigh-pressure physics, astrophysics, and cosmology [145]. Not to forget, the secondary sources of these electron sources such as the production of novel sources as quasi-monoenergetic Xrays[79, 28] and gamma rays[119].

To conclude, of all possible particle accelerators applications, one of the markets where LPA technology has the potential to break through is, after decrease of the energy spread and beam divergence, 4D imaging with unprecedented picometer-femto or attosecond precision at sub-10 MeV electron energies. In this way, multiple groups worldwide keep on working in this quest for the “Holy Grail” of material science.

Bibliography

- [1] G. Aad, T. Abajyan, B. Abbott, J. Abdallah, S.A. Khalek, A. Abdelalim, O. Abdinov, R. Aben, B. Abi, M. Abolins et al. , *Physics Letters B* **716** (2012), 1.
- [2] A.A. Andreev und K.Y. Platonov, *Opt. Spectrosc.* **114** (2013), 788.
- [3] M. Aoyama, K. Yamakawa, Y. Akahane, J. Ma, N. Inoue, H. Ueda und H. Kiriya, *Optics Letters* **28** (2003), 1594.
- [4] V. Bagnoud, B. Aurand, A. Blazevic, S. Borneis, C. Bruske, B. Ecker, U. Eisenbarth, A. Frank, E. Gaul, S. Goette et al. , *Applied Physics B* **100** (2010), 137.
- [5] S. Banerjee, S.Y. Kalmykov, N.D. Powers, G. Golovin, V. Ramanathan, N.J. Cunningham, K.J. Brown, S. Chen, I. Ghebregziabher, B.A. Shadwick, D.P. Umstadter, B.M. Cowan, D.L. Bruhwiler, A. Beck und E. Lefebvre, *Phys. Rev. ST Accel. Beams* **16** (2013), 031302.
- [6] W.L. Barnes, A. Dereux und T.W. Ebbesen, *Nature* **424** (2003), 824.
- [7] B. Beaurepaire, A. Lifschitz und J. Faure, *New J. Phys.* **16** (2014), 023023.
- [8] V.T. Binh, N. Garcia und S. Purcell. In *Electron Field Emission from Atom-Sources: Fabrication, Properties, and Applications of Nanotips*, herausgegeben von P. W. Hawkes, Band 95 von *Advances in Imaging and Electron Physics*. Elsevier (1996), Seiten 63 – 153.
- [9] C.F. Bohren und D.R. Huffman: *Absorption and Scattering by a Sphere*. Wiley-VCH Verlag GmbH, 2007.
- [10] A. Borot, A. Malvache, X. Chen, A. Jullien, J.P. Geindre, P. Audebert, G. Mourou, F. Quéré und R. Lopez-Martens, *Nat. Phys.* **8** (2012), 416.
- [11] F. Brunel, *Physical Review Letters* **59** (1987), 52.
- [12] A. Buck: *Advanced characterization and control of laser wakefield acceleration*. Ludwig-Maximilian-Universität München, Dissertation, 2011.
- [13] A. Buck, M. Nicolai, K. Schmid, C.M.S. Sears, A. Sävert, J.M. Mikhailova, F. Krausz, M.C. Kaluza und L. Veisz, *Nat. Phys.* **7** (2011), 543.

- [14] A. Buck, J. Wenz, J. Xu, K. Khrennikov, K. Schmid, M. Heigoldt, J.M. Mikhailova, M. Geissler, B. Shen, F. Krausz, S. Karsch und L. Veisz, *Phys. Rev. Lett.* **110** (2013), 185006.
- [15] A. Buck, K. Zeil, A. Popp, K. Schmid, A. Jochmann, S.D. Kraft, B. Hidding, T. Kudyakov, C.M.S. Sears, L. Veisz, S. Karsch, J. Pawelke, R. Sauerbrey, T. Cowan, F. Krausz und U. Schramm, *Rev. Sci. Instrum.* **81** (2010), 033301.
- [16] R. Budriūnas, T. Stanislaukas, J. Adamonis, A. Aleknavičius, G. Veitas, D. Gadonas, S. Balickas, A. Michailovas und A. Varanavičius, *Opt. Express* **25** (2017), 5797.
- [17] S.V. Bulanov, F. Pegoraro, A.M. Pukhov und A.S. Sakharov, *Phys. Rev. Lett.* **78** (1997), 4205.
- [18] D.E. Cardenas: *Sub-5 fs laser wakefield acceleration of electrons*. Technische Universität München, Diplomarbeit, 2014.
- [19] R. Carminati, J.J. Greffet, C. Henkel und J.M. Vigoureux, *Optics Communications* **261** (2006), 368.
- [20] A.L. Cavaliere, E. Goulielmakis, B. Horvath, W. Helml, M. Schultze, M. Fieß, V. Pervak, L. Veisz, V. Yakovlev, M. Uiberacker et al. , *New Journal of Physics* **9** (2007), 242.
- [21] M. Cerchez, R. Jung, J. Osterholz, T. Toncian, O. Willi, P. Mulser und H. Ruhl, *Phys. Rev. Lett.* **100** (2008), 245001.
- [22] G. Cerullo und S. De Silvestri, *Rev. Sci. Instrum.* **74** (2003), 1.
- [23] X. Chen, A. Jullien, A. Malvache, L. Canova, A. Borot, A. Trisorio, C.G. Durfee und R. Lopez-Martens, *Opt. Lett.* **34** (2009), 1588.
- [24] S.W. Chou: *Investigation of electron acceleration and deceleration in plasmas*. Ludwig-Maximilian-Universität München, Dissertation, 2016.
- [25] C. Clayton, J. Ralph, F. Albert, R. Fonseca, S. Glenzer, C. Joshi, W. Lu, K. Marsh, S. Martins, W. Mori et al. , *Physical Review Letters* **105** (2010), 105003.
- [26] C.E. Clayton, J.E. Ralph, F. Albert, R.a. Fonseca, S.H. Glenzer, C. Joshi, W. Lu, K.a. Marsh, S.F. Martins, W.B. Mori, a. Pak, F.S. Tsung, B.B. Pollock, J.S. Ross, L.O. Silva und D.H. Froula, *Phys. Rev. Lett.* **105** (2010), 105003.
- [27] G. Colas des Francs, S. Derom, R. Vincent, a. Bouhelier und a. Dereux, *Int. J. Opt.* **2012** (2012), 1.
- [28] S. Corde, K.T. Phuoc, G. Lambert, R. Fitour, V. Malka, A. Rousse, A. Beck und E. Lefebvre, *Reviews of Modern Physics* **85** (2013), 1.
- [29] S. Corde, C. Thaury, a. Lifschitz, G. Lambert, K. Ta Phuoc, X. Davoine, R. Lehe, D. Douillet, a. Rousse und V. Malka, *Nat. Commun.* **4** (2013), 1501.

- [30] P.B. Corkum, *Phys. Rev. Lett.* **71** (1993), 1994.
- [31] H.e.a. Daido, *Rep. Prog. Phys.* **75** (2012).
- [32] C. Danson, D. Hillier, N. Hopps und D. Neely, *High Power Laser Science and Engineering* **3** (2015), e3.
- [33] C.D. Decker und W.B. Mori, *Phys. Rev. E* **51** (1995), 1364.
- [34] C.D. Decker, W.B. Mori, K.C. Tzeng und T. Katsouleas, *Phys. Plasmas* **3** (1996), 2047.
- [35] F. Desforges, B. Paradkar, M. Hansson, J. Ju, L. Senje, T. Audet, A. Persson, S. Dobosz-Dufrénoy, O. Lundh, G. Maynard et al. , *Physics of Plasmas* **21** (2014), 120703.
- [36] L. Di Lucchio und P. Gibbon, *Phys. Rev. ST Accel. Beams* **18** (2015), 023402.
- [37] P. Dombi, P. Rácz und B. Bódi, *Laser Part. Beams* **27** (2009), 291.
- [38] G. Doumy, F. Quéré, O. Gobert, M. Perdrix, P. Martin, P. Audebert, J. Gauthier, J.P. Geindre und T. Wittmann, *Physical Review E* **69** (2004), 026402.
- [39] A. Dubietis, G. Jonušauskas und A. Piskarskas, *Opt. Commun.* **88** (1992), 437.
- [40] E. Esarey und M. Pilloff, *Phys. Plasmas* **2** (1995), 1432.
- [41] E. Esarey, C. Schroeder und W. Leemans, *Rev. Mod. Phys.* **81** (2009), 1229.
- [42] L. Evans, *New Journal of Physics* **9** (2007), 335.
- [43] X. Fan, W. Zheng und D.J. Singh, *Light Sci. Appl.* **3** (2014), e179.
- [44] J. Faure, Y. Glinec, A. Pukhov und S. Kiselev, *Nature* (2004), 541.
- [45] J. Faure, Y. Glinec, J. Santos, F. Ewald, J.P. Rousseau, S. Kiselev, a. Pukhov, T. Hosokai und V. Malka, *Phys. Rev. Lett.* **95** (2005), 205003.
- [46] J. Faure, Y. Glinec, J.J. Santos, F. Ewald, J.P. Rousseau, S. Kiselev, a. Pukhov, T. Hosokai und V. Malka, *Phys. Rev. Lett.* **95** (2005), 205003.
- [47] J. Faure, C. Rechatin, A. Norlin, A. Lifschitz, Y. Glinec und V. Malka, *Nature* **444** (2006), 737.
- [48] J. Faure, C. Rechatin, A. Norlin, A. Lifschitz, Y. Glinec und V. Malka, *Nature* **444** (2006), 737.
- [49] L. Fedeli, A. Sgattoni, G. Cantono, D. Garzella, F. Réau, I. Prencipe, M. Passoni, M. Raynaud, M. Květoň, J. Proska, A. Macchi und T. Ceccotti, *Phys. Rev. Lett.* **116** (2016), 015001.
- [50] H.P. Freund: *Principles of free-electron lasers*. Springer Science & Business Media, 2012.

- [51] D.H. Froula, C.E. Clayton, T. Döppner, K.A. Marsh, C.P.J. Barty, L. Divol, R.a. Fonseca, S.H. Glenzer, C. Joshi, W. Lu, S.F. Martins, P. Michel, W.B. Mori, J.P. Palastro, B.B. Pollock, A. Pak, J.E. Ralph, J.S. Ross, C.W. Siders, L.O. Silva und T. Wang, *Phys. Rev. Lett.* **103** (2009), 215006.
- [52] E.W. Gaul, M. Martinez, J. Blakeney, A. Jochmann, M. Ringuette, D. Hammond, T. Borger, R. Escamilla, S. Douglas, W. Henderson et al. , *Applied optics* **49** (2010), 1676.
- [53] C.G.R. Geddes, J.V. Tilborg, E. Esarey, C.B. Schroeder, D. Bruhwiler, C. Nieter, J. Cary und W.P. Leemans, *Nature* **431** (2004), 535.
- [54] P. Gibbon: *Short Pulse Laser Interactions with Matter An Introduction*. Imperial College Press, 2005.
- [55] P. Gibbon und A.R. Bell, *Phys. Rev. Lett.* **68** (1992), 1535.
- [56] A.J. Gonsalves, K. Nakamura, C. Lin, D. Panasenkov, S. Shiraishi, T. Sokollik, C. Benedetti, C.B. Schroeder, C.G.R. Geddes, J. van Tilborg, J. Osterhoff, E. Esarey, C. Toth und W.P. Leemans, *Nat. Phys.* **7** (2011), 862.
- [57] L.M. Gorbunov, S.Y. Kalmykov und P. Mora, *Phys. Plasmas* **12** (2005), 033101.
- [58] S. Gordienko und A. Pukhov, *Phys. Plasmas* **12** (2005), 043109.
- [59] E. Goulielmakis, V.S. Yakovlev, A.L. Cavalieri, M. Uiberacker, V. Pervak, A. Apolonski, R. Kienberger, U. Kleineberg und F. Krausz, *Science* **317** (2007), 769.
- [60] D. Guénot, D. Gustas, A. Vernier, B. Beaurepaire, F. Böhle, M. Bocoum, M. Lozano, A. Jullien, A. Lifschitz und J. Faure, *Nat. Photonics* (2017), 1.
- [61] B. Hafizi, A. Ting, P. Sprangle und R.F. Hubbard, *Phys. Rev. E.* (2000), 4120.
- [62] F.V. Hartemann, S.N. Fochs, G.P. Le Sage, N.C. Luhmann, J.G. Woodworth, M.D. Perry, Y.J. Chen und A.K. Kerman, *Phys. Rev. E* **51** (1995), 4833.
- [63] G. Herink, D.R. Solli, M. Gulde und C. Ropers, *Nature* **483** (2012), 190.
- [64] D. Herrmann, C. Homann, R. Tautz, M. Scharrer, P.S.J. Russell, F. Krausz, L. Veisz und E. Riedle, *Opt. Exp.* **34** (2010), 2459.
- [65] J. Hoffrogge, J. Paul Stein, M. Krüger, M. Förster, J. Hammer, D. Ehberger, P. Baum und P. Hommelhoff, *J. Appl. Phys.* **115** (2014), 094506.
- [66] L. Hofmann: *Density characterization of supersonic gas jets for laser wakefield acceleration*. Ludwig-Maximilian-Universität München, Diplomarbeit, 2015.
- [67] P. Hommelhoff, C. Kealhofer und M.A. Kasevich, *Phys. Rev. Lett.* **97** (2006), 247402.

- [68] P. Hommelhoff und M. Kling: *Attosecond nanophysics: From basic science to applications*. John Wiley & Sons, 2015.
- [69] P. Hommelhoff, Y. Sortais, A. Aghajani-Talesh und M.A. Kasevich, *Phys. Rev. Lett.* **96** (2006), 077401.
- [70] C.J. Hooker, J.L. COLLIER, O. CHEKHLOV, R.J. CLARKE, E.J. DIVALL, K. ERTEL, P. FOSTER, S. HANCOCK, S.J. HAWKES, P. HOLLIGAN, L. A.J., L. W.J., D. NEELY, P. B.T. und B. WYBORN, *Rev. Laser Engng* **37** (2009), 443.
- [71] S.E. Irvine, A. Dechant und A.Y. Elezzabi, *Phys. Rev. Lett.* **93** (2004), 184801.
- [72] S.E. Irvine, P. Dombi, G. Farkas und a.Y. Elezzabi, *Phys. Rev. Lett.* **97** (2006), 146801.
- [73] J. Jackson: *Classical Electrodynamics, 3rd Edition*. Wiley, 1998.
- [74] O. Jansen, T. Tückmantel und A. Pukhov, *Eur. Phys. J. Spec. Top.* **223** (2014), 1017.
- [75] H.I. Jena. *JETI200 Laser*. <https://www.hi-jena.de/>.
- [76] A. Jullien, O. Albert, F. Burgy, G. Hamoniaux, J.P. Rousseau, J.P. Chambaret, F. Augé-Rochereau, G. Chériaux, J. Etchepare, N. Minkovski et al. , *Optics letters* **30** (2005), 920.
- [77] S.Y. Kalmykov, a. Beck, X. Davoine, E. Lefebvre und B.a. Shadwick, *New J. Phys.* **14** (2012), 033025.
- [78] A. Kessel, V.E. Leshchenko, M. Krüger, O. Lysov, A. Münzer, A. Weigel, V. Pervak, M. Trubetskov, S.A. Trushin, Z. Major, F. Krausz und S. Karsch, *Submitted to CLEO 2017* (2017).
- [79] K. Khrennikov, J. Wenz, A. Buck, J. Xu, M. Heigoldt, L. Veisz und S. Karsch, *Physical review letters* **114** (2015), 195003.
- [80] H.T. Kim, K.H. Pae, H.J. Cha, I.J. Kim, T.J. Yu, J.H. Sung, S.K. Lee, T.M. Jeong und J. Lee, *Phys. Rev. Lett.* **111** (2013), 165002.
- [81] K. Kondo, H. Maeda, Y. Hama, S. Morita, A. Zoubir, R. Kodama, K.A. Tanaka, Y. Kitagawa und Y. Izawa, *J. Opt. Soc. Am. B* **23** (2006), 231.
- [82] D. Koningsberger und R. Prins: *X-ray absorption: principles, applications, techniques of EXAFS, SEXAFS, and XANES*. John Wiley and Sons, New York, NY, 1988.
- [83] G. Kraft, *Progress in Particle and Nuclear Physics* **45** (2000), S473.
- [84] F. Krausz und M. Ivanov, *Rev. Mod. Phys.* **81** (2009), 163.
- [85] W. Kruer: *The physics of laser plasma interactions*. Reading, MA (US); Addison-Wesley Publishing Co., Jan 1988.
- [86] W.L. Kruer und K. Estabrook, *Phys. Fluids* **28** (1985), 430.

- [87] J. Lawson, *IEEE Transactions on Nuclear Science* **26** (1979), 4217.
- [88] W. Leemans, J. Daniels, A. Deshmukh, A. Gonsalves, A. Magana, H. Mao, D. Mittelberger, K. Nakamura, J. Riley, D. Syversrud et al. : *BELLA laser and operations. BELLA laser and operations*, In *Proc. PAC.* (2013).
- [89] W. Leemans, A.J. Gonsalves, H.S. Mao, K. Nakamura, C. Benedetti, C. Schroeder, C. Tóth, J. Daniels, D. Mittelberger, S. Bulanov, J.L. Vay, C. Geddes und E. Esarey, *Phys. Rev. Lett.* **113** (2014), 245002.
- [90] W.P. Leemans, B. Nagler, A.J. Gonsalves, C. Tóth, K. Nakamura, C.G.R. Geddes, E. Esarey, C.B. Schroeder und S.M. Hooker, *Nat. Phys.* **2** (2006), 696.
- [91] T.V. Liseykina, S. Pirner und D. Bauer, *Phys. Rev. Lett.* **104** (2010), 095002.
- [92] W. Lu, M. Tzoufras, C. Joshi, F. Tsung, W. Mori, J. Vieira, R. Fonseca und L. Silva, *Phys. Rev. Spec. Top. - Accel. Beams* **10** (2007), 061301.
- [93] O. Lundh, J. Lim, C. Rechatin, L. Ammoura, a. Ben-Ismaïl, X. Davoine, G. Gallot, J.P. Goddet, E. Lefebvre, V. Malka und J. Faure, *Nat. Phys.* **7** (2011), 219.
- [94] G. Ma, W. Dallari, A. Borot, F. Krausz, W. Yu, G.D. Tsakiris und L. Veisz, *Physics of Plasmas* **22** (2015), 033105.
- [95] S. Macchi, F. Cornolti, F. Pegoraro, T.V. Liseykina, H. Ruhl und V.A. Vshivkov, *Phys. Rev. Lett.* **87** (2001), 205004.
- [96] G. Malka, E. Lefebvre und J. Miquel, *Physical review letters* **78** (1997), 3314.
- [97] G. Malka und J. Miquel, *Physical Review Letters* **77** (1996), 75.
- [98] V. Malka, J. Er, Y.A. Gauduel, E. Lefebvre, A. Rousse und K.I.M.T.A. Phuoc, *Nature Physics* **4** (2008), 447.
- [99] S.P.D. Mangles, C.D. Murphy, Z. Najmudin, A.G.R. Thomas, J.L. Collier, A.E. Dangor, E.J. Divall, P.S. Foster, J.G. Gallacher, C.J. Hooker, D.A. Jaroszynski, A.J. Langley, W.B. Mori, P.A. Norreys, F.S. Tsung, R. Viskup, B.R. Walton und K. Krushelnick, *Nature* (2004), 535.
- [100] B.W. McNeil und N.R. Thompson, *Nature photonics* **4** (2010), 814.
- [101] J.M. Mikhailova, A. Buck, A. Borot, K. Schmid, C. Sears, G.D. Tsakiris, F. Krausz und L. Veisz, *Optics letters* **36** (2011), 3145.
- [102] W. Mori, *IEEE Journal of Quantum Electronics* **33** (1997), 1942.
- [103] G. Mourou, T. Tajima und S. Bulanov, *Rev. Mod. Phys.* **78** (2006), 309.
- [104] P. Mulser und D. Bauer: *High Power Laser-Matter Interaction*. Springer Tracts in Modern Physics. Springer Berlin Heidelberg, 2010.

- [105] P. Mulser, D. Bauer und H. Ruhl, *Phys. Rev. Lett.* **101** (2008), 225002.
- [106] N.M. Naumova, J.a. Nees, I.V. Sokolov, B. Hou und G.a. Mourou, *Phys. Rev. Lett.* **92** (2004), 063902.
- [107] C. Nieter und J.R. Cary, *J. Comput. Phys.* **196** (2004), 448.
- [108] L. Nomerovannaya, M. Kirillova und M. Noskov. *OPTICAL PROPERTIES OF TUNGSTEN SINGLE CRYSTALS*. Technischer Bericht, Inst. of Physics of Metals, Sverdlovsk, USSR, 1971.
- [109] M.A. Ordal, L.L. Long, R.J. Bell, S.E. Bell, R.R. Bell, R.W. Alexander und C.A. Ward, *Appl. Opt.* **22** (1983), 1099.
- [110] T. Paasch-Colberg, A. Schiffrin, N. Karpowicz, S. Kruchinin, O. Salam, S. Keiber, O. Razskazovskaya, S. Mühlbrandt, A. Alnaser, M. Kübel, V. Apalkov, D. Gerster, J. Reichert, T. Wittmann, J.V. Barth, M.I. Stockman, R. Ernstorfer, V.S. Yakovlev, R. Kienberger und F. Krausz, *Nat. Photonics* **8** (2014), 214.
- [111] J. Pang, Y. Ho, X. Yuan, N. Cao, Q. Kong, P. Wang, L. Shao, E. Esarey und A. Sessler, *Physical Review E* **66** (2002), 066501.
- [112] G.G. Paulus, W. Becker, W. Nicklich und H. Walther, *Journal of Physics B: Atomic, Molecular and Optical Physics* **27** (1994), L703.
- [113] E. Pedroni, R. Bacher, H. Blattmann, T. Böhlinger, A. Coray, A. Lomax, S. Lin, G. Munkel, S. Scheib, U. Schneider et al. , *Medical physics* **22** (1995), 37.
- [114] J.M. Pitarke, V.M. Silkin, E.V. Chulkov und P.M. Echenique, *Reports Prog. Phys.* **70** (2007), 1.
- [115] T. Plettner, R. Byer, E. Colby, B. Cowan, C. Sears, J. Spencer und R. Siemann, *Phys. Rev. Lett.* **95** (2005), 134801.
- [116] T. Plettner, P.P. Lu und R.L. Byer, *Phys. Rev. ST Accel. Beams* **9** (2006), 111301.
- [117] E.B. Podgoršak. In *Compendium to Radiation Physics for Medical Physicists*. Springer (2014), Seiten 1041–1099.
- [118] A. Popp: *Dynamics of electron acceleration in laser-driven wakefields: Acceleration limits and asymmetric plasma waves*. Ludwig-Maximilian-Universität München, Dissertation, 2011.
- [119] N.D. Powers, I. Ghebregziabher, G. Golovin, C. Liu, S. Chen, S. Banerjee, J. Zhang und D.P. Umstadter, *Nature Photonics* **8** (2014), 28.
- [120] A. Pukhov und J. Meyer-ter Vehn, *Physical review letters* **76** (1996), 3975.
- [121] A. Pukhov und J. Meyer-ter Vehn, *App. Phys. B* **74** (2002), 355.

- [122] P. Rácz und P. Dombi, *Phys. Rev. A* **84** (2011), 063844.
- [123] C. Rechatin, X. Davoine, A. Lifschitz, A.B. Ismail, J. Lim, E. Lefebvre, J. Faure und V. Malka, *Phys. Rev. Lett.* **103** (2009), 194804.
- [124] C. Rechatin, J. Faure, A. Ben-Ismail, J. Lim, R. Fitour, A. Specka, H. Videau, A. Tafzi, F. Burgy und V. Malka, *Phys. Rev. Lett.* **102** (2009), 164801.
- [125] D. Rivas, A. Borot, D. Cardenas, G. Marcus, X. Gu, D. Herrmann, J. Xu, J. Tan, D. Kormin, G. Ma, W. Dallari, G. Tsakiris, I. Földes, S. Chou, M. Weidmann, B. Bergues, T. Wittmann, H. Schröder, P. Tzallas, D. Charalambidis, O. Raszkazovskaya, V. Pervak, F. Krausz und L. Veisz, *Accepted in Sci. Rep.* (2017).
- [126] L. Roso: *Salamanca Pulsed Laser Center: the Spanish petawatt. Salamanca Pulsed Laser Center: the Spanish petawatt*, In *International Conference on Applications of Optics and Photonics*. International Society for Optics and Photonics (2011) Seiten 800 113–800 113.
- [127] M. Santala, M. Zepf, I. Watts, F. Beg, E. Clark, M. Tatarakis, K. Krushelnick, A. Dangor, T. McCanny, I. Spencer et al. , *Physical Review Letters* **84** (2000), 1459.
- [128] J.P. Schäfer: *Implementierung und Anwendung analytischer und numerischer Verfahren zur Lösung der Maxwellgleichungen für die Untersuchung der Lichtausbreitung in biologischem Gewebe*. Universität Ulm, Dissertation, 2011.
- [129] A. Schiffrin, T. Paasch-Colberg, N. Karpowicz, V. Apalkov, D. Gerster, S. Mühlbrandt, M. Korbman, J. Reichert, M. Schultze, S. Holzner, J.V. Barth, R. Kienberger, R. Ernstorfer, V.S. Yakovlev, M.I. Stockman und F. Krausz, *Nature* **493** (2013), 70.
- [130] K. Schmid: *Supersonic micro-Jets and their application to few-cycle laser-driven electron acceleration*. Ludwig-Maximilian-Universität München, Dissertation, 2009.
- [131] K. Schmid, A. Buck, C.M.S. Sears, J.M. Mikhailova, R. Tautz, D. Herrmann, M. Geissler, F. Krausz und L. Veisz, *Phys. Rev. ST Accel. Beams* **13** (2010), 091301.
- [132] K. Schmid, L. Veisz, F. Tavella, S. Benavides, R. Tautz, D. Herrmann, A. Buck, B. Hidding, A. Marcinkevicius, U. Schramm, M. Geissler, J. Meyer-ter Vehn, D. Habs und F. Krausz, *Phys. Rev. Lett.* **102** (2009), 124801.
- [133] C.B. Schroeder, C. Benedetti, E. Esarey und W.P. Leemans, *Phys. Rev. Lett.* **106** (2011), 135002.
- [134] C.B. Schroeder, E. Esarey und B.a. Shadwick, *Phys. Rev. E. Stat. Nonlin. Soft Matter Phys.* **72** (2005), 055401.
- [135] C.M.S. Sears, S.B. Cuevas, U. Schramm, K. Schmid, A. Buck, D. Habs, F. Krausz und L. Veisz, *Rev. Sci. Instrum.* **81** (2010), 073304.
- [136] P. Sprangle, E. Esarey und A. Ting, *Phys. Rev. A* **41** (1990), 4463.

- [137] M.I. Stockman, *Opt. Express* **19** (2011), 22029.
- [138] M.I. Stockman, *Opt. Express* **19** (2011), 22029.
- [139] D. Strickland und G. Morou, *Optics Communications* (1985), 447.
- [140] G.Z. Sun, E. Ott, Y.C. Lee und P. Guzdar, *Phys. Fluids* **30** (1987), 526.
- [141] P. Suortti und W. Thomlinson, *Physics in medicine and biology* **48** (2003), R1.
- [142] F. Süßmann, L. Seiffert, S. Zherebtsov, V. Mondes, J. Stierle, M. Arbeiter, J. Plenge, P. Rupp, C. Peltz, a. Kessel, S.a. Trushin, B. Ahn, D. Kim, C. Graf, E. Rühl, M.F. Kling und T. Fennel, *Nat. Commun.* **6** (2015), 7944.
- [143] M. Tabak, J. Hammer, M.E. Glinsky, W.L. Kruer, S.C. Wilks, J. Woodworth, M. Campbell, M.D.P.J. Mason, M. Tabak, J. Hammer, M.E. Glinsky, W.L. Kruer, S.C. Wilks, J. Woodworth, E.M. Campbell, M.D. Perry und R.J. Mason, *Phys. of Plasmas* **1** (1994).
- [144] T. Tajima und J. Dawson, *Phys. Rev. Lett.* **43** (1979), 267.
- [145] T. Tajima und G. Mourou, *Phys. Rev. ST Accel. Beams* **5** (2002), 031301.
- [146] J. Tan: *Contrast and Dispersion Management in an OPCPA System*. Ludwig-Maximilians-Universität München, Diplomarbeit, 2016.
- [147] M. Thévenet, A. Leblanc, S. Kahaly, H. Vincenti, A. Vernier, F. Quéré und J. Faure, *Nature Physics* (2015).
- [148] A.G.R. Thomas, Z. Najmudin, S.P.D. Mangles, C.D. Murphy, a.E. Dangor, C. Kamperidis, K.L. Lancaster, W.B. Mori, P.a. Norreys, W. Rozmus und K. Krushelnick, *Phys. Rev. Lett.* **98** (2007), 095004.
- [149] Y. Tian, J. Liu, W. Wang, C. Wang, A. Deng, C. Xia, W. Li, L. Cao, H. Lu, H. Zhang, Y. Xu, Y. Leng, R. Li und Z. Xu, *Phys. Rev. Lett.* **109** (2012), 115002.
- [150] Y. Tian, J. Liu, W. Wang, C. Wang, A. Deng, C. Xia, W. Li, L. Cao, H. Lu, H. Zhang et al. , *Physical review letters* **109** (2012), 115002.
- [151] G.D. Tsakiris, K. Eidmann, J.M. ter Vehn und F. Krausz, *New Journal of Physics* **8** (2006), 19.
- [152] F. Tsung, R. Narang, W. Mori, C. Joshi, R. Fonseca und L. Silva, *Phys. Rev. Lett.* **93** (2004), 185002.
- [153] F.S. Tsung, C. Ren, L.O. Silva, W.B. Mori und T. Katsouleas, *Proc. Natl. Acad. Sci. U. S. A.* **99** (2002), 29.
- [154] M. Tzoufras, W. Lu, F.S. Tsung, C. Huang, W.B. Mori, T. Katsouleas, J. Vieira, R.a. Fonseca und L.O. Silva, *Phys. Plasmas* **16** (2009), 056705.

- [155] A. Vaupel, N. Bodnar, B. Webb, L. Shah und M. Richardson, *Optical Engineering* **53** (2013), 051507.
- [156] L. Veisz, D. Rivas, G. Marcus, X. Gu, D. Cardenas, J. Mikhailova, A. Buck, T. Wittmann, C. Sears, S.W. Chou et al. : *Generation and applications of sub-5-fs multi-10-TW light pulses. Generation and applications of sub-5-fs multi-10-TW light pulses*, In *Conference on Lasers and Electro-Optics/Pacific Rim*. Optical Society of America (2013) Seite TuD2_3.
- [157] J. Vieira, F. Fiúza, L.O. Silva, M. Tzoufras und W.B. Mori, *New J. Phys.* **12** (2010), 045025.
- [158] J. Wang, Y. Ho, Q. Kong, L. Zhu, L. Feng, S. Scheid und H. Hora, *Physical Review E* **58** (1998), 6575.
- [159] P. Wang, Y. Ho, X. Yuan, Q. Kong, N. Cao, A. Sessler, E. Esarey und Y. Nishida, *Applied Physics Letters* **78** (2001), 2253.
- [160] S. Wilks, T. Katsouleas, J. Dawson, P. Chen und J. Su, *IEEE transactions on plasma science* **15** (1987), 210.
- [161] T. Wittmann, B. Horvath, W. Helml, M.G. Schätzkel, X. Gu, A.L. Cavalieri, G. Paulus und R. Kienberger, *Nature Physics* **5** (2009), 357.
- [162] B.P.M. Woodward und B. A., *J. IEE* **93** (1947), 1554.
- [163] M. Zepf, G. Tsakiris, G. Pretzler, I. Watts, D. Chambers, P. Norreys, U. Andiel, A. Dangor, K. Eidmann, C. Gahn et al. , *Physical Review E* **58** (1998), R5253.
- [164] S. Zherebtsov, T. Fennel, J. Plenge, E. Antonsson, I. Znakovskaya, A. Wirth, O. Herrwerth, F. Süß mann, C. Peltz, I. Ahmad, S.a. Trushin, V. Pervak, S. Karsch, M.J.J. Vrakking, B. Langer, C. Graf, M.I. Stockman, F. Krausz, E. Rühl und M.F. Kling, *Nat. Phys.* **7** (2011), 656.
- [165] S. Zherebtsov, F. Süß mann, C. Peltz, J. Plenge, K.J. Betsch, I. Znakovskaya, a.S. Al-naser, N.G. Johnson, M. Kübel, a. Horn, V. Mondes, C. Graf, S.a. Trushin, a. Azzeer, M.J.J. Vrakking, G.G. Paulus, F. Krausz, E. Rühl, T. Fennel und M.F. Kling, *New J. Phys.* **14** (2012), 075010.

Chapter 6

Data archiving

The experimental raw data, the evaluation files, and the figures can be found on the Data Archive Sever of the Laboratory for Attosecond Physics at the Max Planck Institute of Quantum Optics. Each figure has its own folder with the corresponding .eps, .png or .jpg file. Moreover, some of these directories contain either Matlab files to evaluate the raw data, plot files created with OriginPro 9.0 or the date where the raw data used in the thesis can be found (in the server). A explanatory text document commenting the experimental observations and special conditions during each day of the experimental campaigns can also be found in the server. All these files are sufficient to re-evaluate the data in the future.

Chapter 1

- **Fig.1.1**
Laser_scenario.eps
Laser_scenario.opj
- **Fig.1.2**
laser_setup.eps
- **Fig.1.3**
laser_amplification.eps
- **Fig.1.4**
Laser_temp_strc.eps
- **Fig.1.5**
contrast.eps

Chapter 2

- **Fig.2.1**
Z_vs_intensity.eps

IonizationintensityZ.opj

- **Fig.2.2**
electron_energy_in_laser.eps
Pond_scatan_electronenergy_under_laser.
opj
few_cycle_laser.mat
- **Fig.2.3**
pondermotive_sketch.eps
- **Fig.2.4a**
Scattering_angle_vs_energy.eps
Scattering_angle_a0.eps
Pondscatanda0.opj
Pondermotivescat.opj
Pondermotive_angles.mat

- **Fig.2.5a**

- **Fig.2.6**
GDD_plasmas.eps
dispersion.opj
- **Fig.2.7a**
plasma_scale.eps
Laserplasmaskinddepth.opj
- **Fig.2.8a**
normal_skin.eps
Laserplasmaskinddepth.opj
- **Fig.2.9a**
Relativistic_trans.eps
Laserplasmaskinddepth.opj
- **Fig.2.10a**
PIC_nanotargets.eps
- **Fig.2.11a**
PIC_bubble.eps
- **Fig.2.12a**
PIC_bubble_spectrum.eps

Chapter 3

- **Fig.3.1**
wakeboat.eps
- **Fig.3.2**
wakefield_calculations.eps
wakefieldstructure.opj
eval\solution2_1D_wakefield_phase_
space.mat
- **Fig.3.3**
phase_space_intro.eps
eval\solution2_1D_wakefield_phase_

space.mat

- **Fig.3.4**
Shockfront_theory.eps
- **Fig.3.5**
setup_LWFA.eps
- **Fig.3.6**
focal_diagnosis.eps
- **Fig.3.7**
dispersion_magnet.eps
- **Fig.3.8**
Shockwave_in_sideview.eps
- **Fig.3.9**
shockfront_profile.eps
- **Fig.3.10**
LWFA_illustration.eps
- **Fig.3.11**
div_all_together.eps
Pointing_fluctuations.eps
- **Fig.3.12**
field_lab_frame.eps
- **Fig.3.13**
curve_fit.eps
Curve_fits.opj
- **Fig.3.14**
Exp_theory_deph_lengths.eps

-
- Dephlength(expandtheo).opj
 - **Fig.3.15**
transmitted_spectrum.eps
Shockfront_scan.opj
 - **Fig.3.16**
Rayleigh_scan_5um.eps
Focusscan.opj
 - **Fig.3.17**
long_acc_field.eps
Longaccfield.opj
 - **Fig.3.18**
1_2_3.eps
4_5.eps
6_7.eps
8_9.eps
L10_11_12.eps
2_curve_rms_error.eps
charge.eps
Relative_spread.eps
absolute_spread.eps
double_period_divergence.eps
Doubledephasing.opj
 - **Fig.3.19**
phase_space_2.eps
eval\solution2_1D_wakefield_phase_space.mat
 - **Fig.3.20**
shockfront_detail.eps
Q_shockfront.eps
 - **Fig.3.21**
absolute_relat_spread_8fs_simu.eps
 - energy_acclength_8simu.eps
8_fs_typical_spec_simu.eps
absolute_relat_spread_8fs_simu.eps
8_fs_typical_spec_experiment.eps
charge_8fs_experiment.eps
Evaluation_Run_204_ShockFrontScanDC.opj
FINALFIG6.opj
PICsimulations.opj
\electron1_correctyaxis.mat
 - **Fig.3.22**
8_simu_4e19_spectra.eps
 - **Fig.3.23**
Normalized_acc_field.eps Longaccfield.opj
 - **Fig.3.24**
electric_field_5simu_0fs2.eps
 - **Fig.3.25**
electric_field_5simu_20fs2_0umfocus.eps
 - **Fig.3.26**
wakeacceleration_chirp.eps
 - Matlab codes:
matlab\Focus_Analyzer_ELAC_v2.mat
matlab\Analyze_all.mat
matlab\Spectrum.mat
matlab\divergence.mat
matlab\Spectrum.mat
Information: matlab\readme.txt
 - **Fig.4.1**
excitation_plasmon.eps

Chapter 4

- **Fig.4.2**
Mie_fields.eps
\Mie\MieMatscat\calccyl.mat
- **Fig.4.3**
MieFields_time.jpg
- **Fig.4.4**
tunnel_current.eps
tunnelcurrent.opj
tunne_current.mat
- **Fig.4.5**
sub_cycle_plasmon_quivering.eps
- **Fig.4.6**
asy_cep_thrs.eps
- **Fig.4.7**
asy_cep.eps
- **Fig.4.8**
focuslum.eps
Focusscan.opj
\matlab\focus.mat
- **Fig.4.9**
Gouy_phase_laser.eps
Gouyphase.opj
few_cycle_laser.mat
- **Fig.4.10**
Nano_setup.eps
- **Fig.4.11**
DOF_needle.eps
- **Fig.4.12**
Average_shots.eps
Average_finalforpaper.mat
- **Fig.4.13**
top_shot.eps
- **Fig.4.14**
nano_spectrum.eps
Electronspectrum.opj
readspectrum.mat
- **Fig.4.15**
polarization_dependence.eps
- **Fig.4.16**
emission_forces.eps
- **Fig.4.17**
Intensity_scan.eps
Intensity_scan.opj
Pondermotive_angles.mat
- **Fig.4.18**
Charge_scan.eps
- **Fig.4.19**
Intensity_scan_typicalshots.eps
- **Fig.4.20**
CEP_asy_exp.eps
CEPmeasurements.opj
\Simulations\analysis.mat
- **Fig.4.21**
CEP_asy_exp_colorbar.eps
- **Fig.4.22**
CEPmeasurements.opj
Pointing_cep_v2.eps
- **Fig.4.23**
Pointing_cep_PIC_V2.eps
\Simulations\CEPdependences.opj
\Simulations\analysis.mat
- **Fig.4.24**
Fig5_1.eps

-
- **Fig.4.25**
 Fig5_2.eps
 Analysisofisolatedbunch.opj
 read_field.mat
 - **Fig.4.26**
 Fig5_3.eps
 - **Fig.4.27**
 Fig5_4.eps
 - **Fig.4.28**
 nano\Fig5_5.eps
 - **Fig.4.29**
 Fig5_6.eps
 Spectrum_simulationgating1.5pi.opj
 \thot-5e19\read_thot_plots.mat
 - **Fig.4.30**
 Nano_scaling.eps
 Nano_scaling_a0.opj
 - **Fig.4.31**
 CEP_cycle_to_cycle.eps
 - **Fig.4.32**
 Bunch_resolving.eps
 - **Fig.4.33**
 CEP_aver_PIC.eps
 CEP_1_PIC.eps
 CEP_2_PIC.eps
 - CEP_3_PIC.eps
 - CEP_4_PIC.eps
 - 2dplotanalysis.mat
 - Matlab codes:
 \matlab\Focus_Analyzer_ELAC_v2.mat
 \matlab\Analzye_all.mat
 \matlab\Spectrum.mat
 \matlab\divergence_05022016.mat
 \matlab\divergence_24022016.mat
 \matlab\divergence_07032016.mat
 \matlab\divergence_08032016.mat
 \matlab\readfile05022016.mat
 \matlab\readfile24022016.mat
 \matlab\readfile07032016.mat
 \matlab\combining_days.mat
 \matlab\PICanalysis.mat
 \matlab\plotting_2days.mat
 \matlab\plotting_2days_2Dplots.mat
 Information: matlab\readme.txt

Chapter 5

- **Fig.5.1**
 Conclusion1.eps
 FINALFIG2.opj
- **Fig.5.2**
 Conclusion2.eps

Acknowledgments

1. First of all, I want to thank my PhD adviser **Prof. Dr. Ferenc Krausz** for giving me the opportunity to work and study in such a world-leading institute.
2. My most personal and special thanks also go to **Prof. Dr. László Veisz**, for supervising my day-to-day work as well as correcting this thesis. He has taught me the majority of my knowledge in Optics and we have become good friends after almost six years working together.
3. I want to express my thanks to **Prof. Dr. Malte Kaluza** for accepting being the second supervisor in my committee and his interest into my work.
4. I would like to thank **Dr. Shao-wei Chou**, with whom I spent most of the time in the laboratory during the LWFA experiments presented in this thesis. My PhD would have taken much longer had he not been at the LWS-20 group when I started at MPQ. Furthermore, I would like to thank **Luisa Hofmann**, with whom I spent long beamtimes during the LWFA campaign as well for her contribution in building the RANP setup.
5. **Tobias M. Ostermayr** with whom I spent marathonic nights during the RANP campaign. Without his clever ideas, this beamtime would not have been successful at all. Furthermore, I would like to thank **Prof. Dr. Jörg Schreiber** for his scientific interest in the LWS-20 group and his personal support. Also many thanks go to **T. Rösch** and **M. Würfl** for calibrating correctly our electron spectrometer. Similarly, to **Prof. Dr. Matthias. F. Kling** for his personal support and scientific advice in the interpretation of the RANP results.
6. I am very thankful to **Dr. Laura di Lucchio** and **Prof. Paul Gibbon** for all their support from the theoretical and computational side. They performed many simulations for us with which we could understand the highly-complex RANP experiments. Similarly, I would like to thank **Dr. Jiancai Xu** for doing the simulations in LWFA with shock front.
7. Many thanks and memories I owe to the LWS-20 group for all their work on the laser system: **Dr. Antonin Borot**, **Dmitri Kormin**, **Dr. Guangjin Ma**, **Dr. William Dallari**, **Dr. Matthew Weidman**, **Dr. Boris Bergues**, **Dr. Tibor Wittmann**, **Jeryl Tan** and **Pascal Weinert**. Moreover, I wish the best of luck to **Alexander Muschet** and **Peter Fischer** in Sweden.
8. I wish to thank **Manfred Fischer**, **Alois Böswald**, **Anton Horn** and **Harald Haas** for their great help along these last years.
9. I would like to thank **Michael Rogg** and his team at the MPQ-Werkstatt for their fast and effective work in different experiments during my PhD.
10. My colleague and friend **Daniel Rivas**, for countless funny moments (inside and outside the MPQ), his dedicated work on the LWS-20 laser system and his help during my PhD. Similarly, to all my friends at MPQ: **Mathias Krüger**, **Olga Razskazovskaya**, **Olga Lysov** and **Alexander Kessel** for making these last years more enjoyable. Special thanks go to **Dr. Hanieh Fattahi** for supporting me in these last months of my PhD.
11. Finalmente quiero agradecer a mi familia y en particular a mi madre, por ser *el negativo de la foto de mi alma*. Sin ustedes no lo hubiese logrado; und meinen Freund **Dominik Obesser** und seine Familie für seine Unterstützung und Liebe in diesen letzten Jahren. Ohne euch hätte ich es auch nicht geschafft.